

Universität Stuttgart



Deutsches Zentrum
für Luft- und Raumfahrt
German Aerospace Center

Master's Thesis

**Enhancement of a Flow Calorimeter by Coupling
a Measurement Heat Exchanger-Bypass, for
Heat Capacity and Heat Transfer Measurements
Using a Silicone-based Heat Transfer Fluid up to
430°C for Concentrated Solar Power
Applications**

submitted by

Oliver Pfrommer

from Karlsruhe

| | |
|-----------------|---|
| Degree programm | M. Sc. Energy Engineering |
| Examined by | Prof. Dr.-Ing. Konstantinos Stergiaropoulos |
| IGTE Supervisor | Dr.-Ing. Henner Kerskes |
| DLR Supervisor | Dipl.Ing. Christoph Hilgert |
| Submitted on | 14 June 2023 |

Declaration of Originality

Master's Thesis of Oliver Pfrommer (M. Sc. Energy Engineering)

| | |
|----------------|---|
| Address | Hinter der Kirche 76, 76307 Karlsbad |
| Student number | 3489149 |
| English title | <i>Enhancement of a Flow Calorimeter by Coupling a Measurement Heat Exchanger-Bypass, for Heat Capacity and Heat Transfer Measurements Using a Silicone-based Heat Transfer Fluid up to 430°C for Concentrated Solar Power Applications</i> |
| German title | <i>Verbesserung eines Durchflusskalorimeters durch Ergänzung eines Messwärmetauscher-Bypasses für Wärmekapazitäts- und Wärmeübertragungsmessungen eines silikonbasierten Wärmeträgerfluids bis zu 430°C für Anwendungen in solarthermischen Kraftwerken</i> |

I now declare,

- that I wrote this work independently,
- that no sources other than those stated are used and that all statements taken from other works—directly or figuratively—are marked as such,
- that the work submitted was not the subject of any other examination procedure, either in its entirety or in substantial parts,
- that I have not published the work in whole or in part, and
- that my work does not violate any rights of third parties and that I exempt the University against any claims of third parties.

Stuttgart, 14 June 2023

Abstract

In concentrating solar power (CSP), the efficiency and profitability is significantly determined by the heat transfer fluid (HTF) that transports the heat from the receiver to the power block. The achievable efficiency and capacity of parabolic power plants is also limited, by the maximum operating temperature of the HTF. The novel silicone-based HTF HELISOL[®]XLP (HXLP) enables operating temperatures up to 430 °C, comprises reduced environmental and occupational risks and requires no exchange over a power plant lifetime of 25 years. Thus, several advantages result compared to the current benchmark eutectic mixture of biphenyl and diphenyl oxide (BP/DPO) with a maximum operating temperature of 400 °C.

This thesis presents the design of a measurement bypass at the PROMETEO parabolic trough collector (PTC) loop at Plataforma Solar de Almería (PSA) to demonstrate the fluid properties such as the specific heat capacity and heat transfer coefficient of HXLP under typical PTC loop conditions up to 430 °C. An existing flow calorimeter is enhanced for the increased temperatures by coupling an HTF cooler, as previous measurements stated systematic deviations of the Coriolis mass flow sensor at temperatures above 270 °C. In order to lower the measurement uncertainty at high temperatures, an HTF cooler enables lower operating temperatures at the sensor. Furthermore, the option of in-line volume flow calibration using laser Doppler anemometry, developed and applied by the national metrology institute (PTB) is implemented.

For the development of the measurement heat exchanger (MHE) to measure the heat transfer coefficient of HXLP at 430 °C the sensitivity of the measurands i.e. temperature, geometry and heat losses on the heat transfer is investigated and the derivations are respected during the design of the MHE. The selected design applying a water-HTF counter flow double pipe measurement heat exchanger enables straightforward applications of the equations given in the literature for comparison of the actual to the calculated heat transfer coefficient. An evaluation routine is developed to perform post-measurement evaluation, incorporating statistical uncertainties based on example process data of PROMETEO and known systematic uncertainties. The automated uncertainty analysis promises an overall uncertainty of 1.2 % for the specific heat capacity and 1.46 % for the heat transfer coefficient each at 430 °C.

Contents

| | |
|--|-------------|
| Abstract | iii |
| List of Acronyms | vii |
| List of Symbols | ix |
| List of Figures | xi |
| List of Tables | xiii |
| 1. Introduction | 1 |
| 1.1. Motivation | 2 |
| 1.2. Research Problem | 2 |
| 2. Fundamentals | 3 |
| 2.1. Concentrating Solar Power | 3 |
| 2.1.1. Parabolic Trough Collectors | 4 |
| 2.2. Plataforma Solar de Almería | 6 |
| 2.3. SING Project Objectives | 7 |
| 2.4. Heat Transfer Fluids | 8 |
| 2.4.1. HELISOL [®] XLP | 9 |
| 2.5. Specific Heat Capacity | 10 |
| 2.5.1. KONTAS-cp Flow Calorimeter | 11 |
| 2.6. Heat Transfer | 12 |
| 2.7. Double Pipe Heat Exchanger | 15 |
| 2.8. Calculation Method for Convective Heat Transfer | 16 |
| 2.8.1. Heat Transfer in Pipe Flow | 17 |
| 2.8.2. Heat Transfer in Concentric Annular Gap | 17 |
| 2.9. Uncertainty Estimation | 18 |
| 3. Design of the Measurement Bypass | 19 |
| 3.1. Enhancement of the Existing Flow Calorimeter | 19 |
| 3.1.1. Stress Analysis for Adapted Pipes | 20 |
| 3.2. Design of the Measurement Heat Exchanger | 22 |
| 3.2.1. Temperature Measurement in the Heat Exchanger | 25 |
| 3.2.2. Massflow Measurement | 28 |
| 3.2.3. Geometry of the Heat Exchanger | 29 |
| 3.2.4. Stuffing Box for Length Expansion Compensation | 30 |
| 3.2.5. Heat Losses | 30 |
| 4. Measurements and Evaluation | 33 |
| 4.1. Validation of the Flow Calorimeter with Water | 33 |
| 4.2. Generation of Dummy Data for the Measurement Heat Exchanger | 36 |
| 4.3. Data Evaluation for the Measurement Heat Exchanger | 39 |
| 4.3.1. Energy Balance in the Heat Exchanger | 39 |

Contents

| | |
|--|-----------|
| 4.3.2. Heat Losses in the Heat Exchanger | 40 |
| 4.3.3. Specific Heat Capacity and Heat Transfer Coefficient in Heat Exchanger | 41 |
| 5. Measurement Uncertainties | 43 |
| 5.1. Measurement Uncertainty of Specific Heat Capacity | 43 |
| 5.1.1. Comparison of the Uncertainties for the Different Modes of Measuring the Specific Heat Capacity | 46 |
| 5.2. Measurement Uncertainty of Specific Heat Transfer Coefficient | 47 |
| 6. Conclusion and Outlook | 51 |
| Bibliography | 53 |
| A. Data Sheet of HELISOL[®] XLP | 57 |
| B. Enhancement of the Flow Calorimeter | 61 |
| B.1. ROHR2 Stress Simulation | 61 |
| C. Design of the Measurement Heat Exchanger | 63 |
| D. Uncertainty Estimation of the Heat Transfer Coefficient | 69 |
| D.1. Partial Derivatives of the Specific Heat Transfer Coefficient of HXLP | 71 |

List of Acronyms

| | |
|---------|--|
| BP/DPO | Biphenyl and diphenyl oxide |
| CAD | Computer aided design |
| CFD | Computational fluid dynamics |
| CIEMAT | Centro de Investigaciones Energéticas, Medioambientales y Tecnológicas |
| CNC | Computerized Numerical Control |
| CSP | Concentrated solar power |
| DAQ | Data acquisition |
| DIN | German Institute for Standardization |
| DLR | German Aerospace Center |
| DN | Nominal diameter for pipes |
| DNI | direct normal irradiance |
| EEA | European Environment Agency |
| EU | European Union |
| GUM | Guide to the expression of uncertainty in measurement |
| HTF | Heat transfer Fluid |
| HXLP | HELISOL [®] XLP |
| ITML | Inlet Temperature Measurement Location |
| LABVIEW | Laboratory Virtual Instrumentation Engineering Workbench |
| LDA | Laser Doppler anemometry |
| NPT-F | National pipe taper fuel |
| OTML | Outlet Temperature Measurement Location |
| PID | Piping and instrumentation diagram |
| PN | Pressure Nominal |
| PSA | Plataforma Solar de Almería |
| PTB | National metrology institute of the Federal Republic of Germany |
| PTC | Parabolic trough collectors |
| RISE | Research Institute of Sweden AB |
| RSS | Root-sum-of-squares |
| SIMON | Silicone Fluid Maintenance and Operation |
| SING | Silicone next generation |
| SITEF | Silicone fluid Test Facility |
| UN | United Nations |
| UPS | Uninterrupted power supply |
| VDI | The Association of German Engineers |

List of Symbols

| Symbol | Description | Unit |
|----------------------|-------------------------------|----------------------|
| A | Surface | m ² |
| a | Diameter ratio | - |
| c _i | Sensitivity coefficient | - |
| c _p | Specific heat capacity | J/(kg K) |
| d | Diameter | m |
| e | Emissivity of the surface | - |
| H | Enthalpie | J |
| k | Heat transmission coefficient | W/(m ² K) |
| L | Length | m |
| \dot{m} | Mass flow | kg/s |
| Nu | Nusselt number | - |
| P | Power | W |
| Pr | Prandtl number | - |
| Q | Heat | J |
| R | Thermal resistance | (m ² K)/W |
| r | Radius | m |
| Ra | Surface roughness | μm |
| Re | Reynolds-number | - |
| T | Temperature | K |
| t | Time | s |
| U | Internal energy | J |
| u | Velocity | m/s |
| u(Y) | Uncertainty of Measurand | - |
| V | Volume | m ³ |
| W | Work | J |
| Y | Measurand | - |
| α | Heat transfer coefficient | W/(m ² K) |
| α _{thermal} | Thermal expansion coefficient | K ⁻¹ |
| ζ | Discharge coefficient | - |
| η | Dynamic viscosity | Pa s |
| θ | Temperature | °C |
| λ | Thermal conductivity | W/(mK) |
| ν | Kinematic viscosity | m ² /s |
| ρ | Density | kg/m ³ |

List of Figures

| | | |
|-------|---|----|
| 2.1. | General principle and design of a parabolic trough collector | 4 |
| 2.2. | Schematic set-up of a receiver/ absorber tube for parabolic trough collectors | 4 |
| 2.3. | Layout of a parabolic trough power plant with thermal storage and oil as heat transfer fluid | 5 |
| 2.4. | Aerial view of PROMETEO parabolic trough facility at Plataforma Solar de Almería | 6 |
| 2.5. | Schematic of the measurement bypass at PROMETEO for measuring the specific heat capacity and heat transfer coefficient of HXLP | 7 |
| 2.6. | Operating temperature for various heat transfer fluids and respective classes in solar parabolic trough applications | 8 |
| 2.7. | Molecular structure of polydimethylsiloxane heat transfer fluids | 9 |
| 2.8. | Principle of flow calorimetry with temperature and mass flow measurement and heater | 10 |
| 2.9. | Sectional view of the measurement setup, indicating the energy balance volume, flow directions and HTF temperatures | 11 |
| 2.10. | Development of the boundary layer over a wall with the different flow regimes | 12 |
| 2.11. | Schematic drawing of counter flow double pipe heat exchanger | 15 |
| 2.12. | Temperature profile of a counterflow heat exchanger with concave profile | 15 |
| 2.13. | Temperature profile through a pipe wall with convective and conductive heat transfer | 16 |
| 3.1. | Simplified PID of the enhanced flow calorimeter at the PROMETEO measurement bypass | 19 |
| 3.2. | Thermal sections of flow calorimeter for stress analysis | 20 |
| 3.3. | Schematic design of the measuring heat exchanger with temperature measuring chambers, precision tubes, static mixers and stuffing box. | 22 |
| 3.4. | Simplified PID of measurement heat exchanger bypass with pressurized water for cooling the heat transfer fluid | 23 |
| 3.5. | Temperature measuring chamber with compression fitting for Pt100 Sensors | 25 |
| 3.6. | Flow velocity in measurement chamber for different length of temperature sensor | 26 |
| 3.7. | Temperature profile in measurement chamber for HELISOL XLP with immersion depth of 100mm from center of T-piece | 26 |
| 3.8. | Sliced geometry of temperature measuring chamber | 27 |
| 3.9. | HELISOL [®] XLP samples and the influence of fluid quality on the left side clear fluid and on the right side scattered turbid fluid with residues of a previous HTF | 28 |
| 3.10. | Stuffing box for sealing the inner pipe to the outer pipe and allowing relative motion in axial direction | 30 |
| 3.11. | Heat loss of 2000 mm pipe section of the heat exchanger through insulation for different wind speeds at 20°C ambient temperature | 31 |
| 4.1. | Flow calorimeter setup with water for validation measurements | 33 |
| 4.2. | Measurement of flow calorimeter with water for system validation | 34 |
| 4.3. | Deviations of the Pt100 temperature readings over the absolute temperature to the reference in the AMETEK calibrator with the tolerance limits | 34 |
| 4.4. | Relative calibration in AMTETEK calibrator indicating larger deviations at higher temperatures in a range from 25 °C to 475 °C | 35 |

List of Figures

| | | |
|-------|---|----|
| 4.5. | Raw data set (left side) and data set after relative and absolute calibration (right side) of Pt100 temperature reading | 35 |
| 4.6. | Exemplary measurement data of PROMETEO facility from September 2022 . . . | 36 |
| 4.7. | Overview chart of selected operating data of the demo data of the PROMETEO system, top: inlet temperatures and pressure of HXLP, below: mass flows HXLP and water | 37 |
| 4.8. | Simplified scheme for the arrangement of the circumferential temperature sensors on the outer pipe surface | 38 |
| 4.9. | Absorbed heat of water in the measurement heat exchanger and mean temperature difference between inlet and outlet in a measurement point over 5 minutes | 39 |
| 4.10. | Program flow for iterative calculation of specific heat transfer coefficient | 41 |
| 4.11. | Temperature profile of HXLP and water in heatexchanger over the proportion of the total length of 2000 mm | 42 |
| 5.1. | Uncertainty of specific heat capacity for different modes of operation | 46 |
| 5.2. | Pie chart of uncertainty contributions from different sources for the heat transmission coefficient k | 48 |
| 5.3. | Proportion of the influence parameters in the overall uncertainty for the heat transfer coefficient for HXLP at different fluid temperatures | 49 |
| B.1. | Results of ROHR2 stress simulation for case 1 with 41.1% utilisation of the strength | 61 |
| B.2. | Results of ROHR2 stress simulation for case 2 with 46% utilisation of the strength | 61 |
| B.3. | Results of ROHR2 stress simulation for case 3 with 42.5% utilisation of the strength | 62 |
| B.4. | Results of ROHR2 stress simulation for case 4 with 52.6% utilisation of the strength | 62 |
| B.5. | Flow calorimeter with measurement bypass at PROMETEO facility | 62 |
| C.1. | Initial Drawing of the heat exchanger | 63 |
| C.2. | Guiding tubes for stabilisation Pt100 sensors through the measuring chamber . . | 64 |
| C.3. | Technical drawing of the temperature measurement chamber for the heat exchanger | 65 |
| C.4. | Measurement section for in-situ LDA calibration for temperatures up to 300°C for silicone oil | 66 |
| C.5. | Technical drawing of the stuffing box | 67 |
| C.6. | Technical drawing of the nut of the stuffing box | 68 |

List of Tables

| | |
|---|----|
| 2.1. Overview and comparison of CSP technologies | 3 |
| 2.2. Physical properties of HELISOL [®] XLP in use based on laboratory data by Wacker | 9 |
| 2.3. Typical heat transfer coefficient values for different heat transfer situations | 13 |
| 3.1. Temperatures in the thermal sections for different operation points | 21 |
| 3.2. Dimensions and tolerances for precision pipes according to DIN 10305-1 | 29 |
| 4.1. Integrated sensors for heat exchanger with sensor names of PID | 36 |
| 4.2. Initial values for the generation of demo data | 37 |
| 4.3. Input values for the calculations of radial temperatures along the heat exchanger . | 38 |
| 5.1. Type B uncertainties for calculating the overall measurement uncertainty for the specific heat capacity of HXLP | 43 |
| 5.2. Type B uncertainties of the individual measurands for calculating the overall mea- surement uncertainty for the specific heat transfer coefficient of HXLP in the heat exchanger | 47 |
| A.1. Physical properties of HELISOL [®] XLP in use based on laboratory data by Wacker | 59 |

1. Introduction

The effects of anthropogenic climate change are getting increasingly noticeable, prompting the need to successively replace fossil fuels with sustainable technologies. At the UN Climate Change Conference in 2015, 197 countries agreed to limit global warming to 1.5 °C compared to pre-industrial times. The increase in renewable energies in the electricity sector plays an essential role in the success of the energy transition. The energy sector accounts for the largest share of annual greenhouse gas emissions in Europe. Even though major savings have already been achieved since 1990, the energy sector needs to be decarbonised. There are various approaches to decarbonising the energy sector, whereby the interaction between profitability, sustainability and reliability of supply is of key importance.

While there are different classifications of sustainable energy, the EU taxonomy has recently classified nuclear power and gas as transitional technologies. In 1987, the United Nations gave a broader definition in the Brundtland Report: "Sustainable development is development that meets the needs of the present without compromising the ability of future generations to meet their own needs" (United-Nations, 1987, p. 37). In order to cope with this sustainable transformation of the electricity sector, massive investments in sustainable energies such as wind energy, solar energy and hydro power are necessary. Since renewable energies are subject to the fluctuations of the weather, the forecasting, regulation and storage of energy is gaining in importance. Concentrating solar power (CSP) is a technology that offers several advantages, such as reliable and stable energy supply and the comparatively simple storage of energy and thus the provision of renewable energy on demand.

The achievable efficiency and capacity of parabolic trough power plants, is significantly limited by the maximum operating temperature of the heat transfer fluid (HTF) used to transport the heat from the collector field to the power block. The state of the art HTF is the eutectic mixture of biphenyl and diphenyl oxide (BP/DPO), with an maximum operating temperature of 400 °C. In order to increase the operating temperature of parabolic trough power plants and thus the efficiency and profitability, the German Aerospace Center (DLR) is conducting research on new silicone-based HTF at the Plataforma Solar de Almería (PSA). Silicone-based heat transfer fluids are promising as they allow higher operating temperatures up to 430 °C and are much more environmentally friendly and chemically stable over its lifetime, than BP/DPO. The improved properties of the silicone-based HTF, named HELISOL[®] XLP (HXLP), is currently under demonstration in the national German project SING (silicone fluid next generation) in order to enable a large-scale market introduction for CSP applications.

1.1. Motivation

The essential purpose of the HTF in CSP applications is to absorb the heat from the absorber pipe effectively and transport it out of the collector field. This can be represented in technical terms by two thermo-physical fluid properties, the heat capacity and the heat transfer coefficient. The knowledge of the fluid properties are relevant from a technical point of view as they prove the concept and confirm the heat transfer behaviour for the increased temperatures up to 430 °C. From an economic point of view, these data ensure planning confidence and bankability of projects. To establish HXLP in parabolic trough systems, its temperature-dependent thermo-physical properties must be known over the entire application range, focusing on the application limit at 430 °C. To demonstrate the feasibility and improved thermo-physical properties, qualification measurements under real CSP operating conditions must be carried out in addition to laboratory measurements, to confirm at larger scale under typical conditions.

For this purpose, the PROMETEO parabolic trough loop at PSA is used in cooperation with the Spanish research institute 'Centro de Investigaciones Energéticas, Medioambientales y Tecnológicas' (CIEMAT) to test HXLP under loop scale conditions. In a measurement bypass, the specific heat capacity and the heat transfer coefficient is measured under typical operating conditions up to 430 °C. This enables reliable measurement data of a real parabolic trough collector (PTC) loop to be obtained, which lowers the implementation hurdles for new CSP projects, for the above mentioned reasons.

1.2. Research Problem

To measure the heat capacity and heat transfer at loop scale up to 430 °C, a measurement bypass consisting of a flow calorimeter and a measurement heat exchanger is set up. A flow calorimeter for measuring the heat capacity of HTF up to 350 °C had previously been used at a different facility (Hilgert, Howar, et al., 2019). However, to measure the heat capacity of HXLP at the PROMETEO facility up to 430 °C the existing flow calorimeter is adapted for the increased temperatures. The Coriolis massflow sensor showed increased uncertainties at temperatures above 270 °C. Therefore, a heat exchanger should cool the HTF upstream the mass flow sensor, enabling a comparably low operation temperature of the Coriolis sensors even at 430 °C in the PTC loop.

For the aim of measuring the heat transfer of HXLP in the heat exchanger with a uncertainty below 2 %, a measurement heat exchanger is designed. The heat transfer from HXLP to water is measured in a double-pipe heat exchanger. The approach to reduce the measurement uncertainties is to examine the sensitivity of the measurands for the heat transfer and consider them in the design. An evaluation routine is established to automatically perform the measurement analysis, incorporating statistically and known systematic uncertainties. This is based on process data of PROMETEO, which are generated to simulate the operation of the measurement heat exchanger. The comprehensive uncertainty analysis enables the comparison of the measurement data with laboratory results and manufacturer specifications.

After completion of this work and the successful design of the measurement bypass, measurements of the heat capacity and the heat transfer of HXLP with low measurement uncertainty can be carried out at PROMETEO. This answers the question of the actual heat transfer and the heat capacity under PTC loop conditions.

2. Fundamentals

2.1. Concentrating Solar Power

Concentrating solar power (CSP) uses mirrors or lenses to concentrate solar irradiation onto a thermal receiver. The incoming solar irradiation is absorbed and converted into heat. This heat can be stored and is usually used to drive a heat engine that is coupled to a generator to produce electrical energy. The heat source can also be used for chemical reactions or other downstream technologies. CSP systems capture only direct normal irradiance (DNI). Whereby the diffuse radiation cannot be used, which is why CSP systems are located in areas with high percentage of clear sky days (Lovegrove and Stein, 2012, p. 6).

CSP technologies are classified into line-focusing and point-focusing concentrators. Point-focusing are central receiver towers with heliostats or parabolic dishes. Line-focusing are parabolic trough systems or fresnel systems. An overview and comparison of the CSP technologies can be seen in Table 2.1, and these are described in the following section (Lovegrove and Stein, 2012, pp. 6–10).

| | Capacity per unit [MW] | Concentration ratio | Operating temperature [°C] |
|-------------------------|---------------------------|------------------------|-------------------------------|
| Central receiver towers | 10 - 150 | 300 - 1000 | 300 - 1000 |
| Parabolic dishes | 0.01 - 0.4 | 1000 - 3000 | 120 - 1500 |
| Linear fresnel | 10 - 200 | 200 | 50 - 300 |
| Parabolic trough | 10 - 200 | 50 - 90 | 200 - 400 |

Table 2.1.: Overview and comparison of CSP technologies (Müller-Steinhagen and Trieb, 2004, p. 2) (Chen et al., 2020, p. 3)

Central receiver towers consists of a series of two axes-tracking heliostats (mirrors) that follow the movement of the sun and reflect the sunlight onto a receiver at the top of a tower. The receiver at the top of the tower absorbs the incoming concentrated sunlight and is heated up. This thermal energy is collected and transferred through a heat transfer fluid to the ground where it can be stored or used to drive a steam power plant.

Parabolic dishes uses three-dimensional parabolic concentrators. The concentrators reflect direct normal radiation onto a point receiver. The dish is bi-axially tracked to the sun. At the focus, a Stirling engine converts the thermal energy.

Linear fresnel consists of flat or slightly curved mirrors that track the sun on one axis and focus the direct solar radiation onto a line. A downward-facing, stationary receiver tube absorbs the radiation.

Since the topic of this thesis is based on the technology of parabolic trough systems, it will be described in more detail in the following.

2.1.1. Parabolic Trough Collectors

Parabolic trough collectors (PTC) use linear parabolic mirrors to reflect direct beam radiation onto an axis-tracking linear focal point on a receiver tube as can be seen in Figure 2.1. Solar radiation is absorbed by the receiver tube and converted into thermal energy. Parabolic trough collectors have a support structure to ensure the geometric parabolic shape. Standardised designs like the EuroTrough (Lüpfert et al., 2003, p. 3) provide stiffness and prevent torsion, which results in improved optical performance and wind resistance. Typical widths of such parabolic trough collectors are 0.5 m - 10 m (Alexopoulos and Kalogirou, 2022, p. 44).

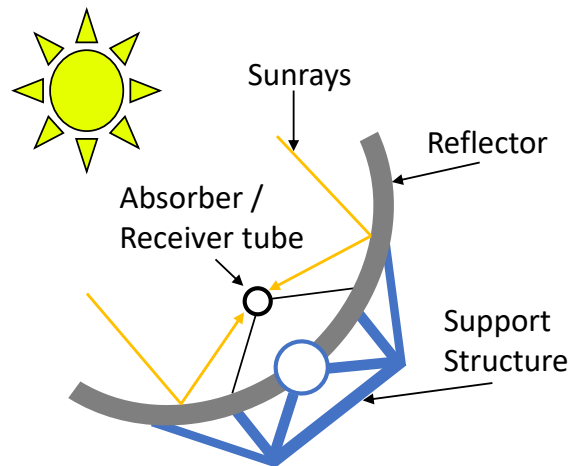


Figure 2.1.: General principle and design of a parabolic trough collector

A receiver tube is shown in Figure 2.2 and consists of two concentric tubes, an inner steel tube containing the heat transfer fluid and a vacuumed glass envelope. The outer surface of the steel tube has an optically selective surface with high solar absorptance and low emittance for thermally generated infrared radiation (Lovegrove and Stein, 2012, p. 208). The glass envelope provides transmittance and the vacuum annular gap reduces conductive heat loss. A chemical getter absorbs gas molecules to maintain the vacuum.

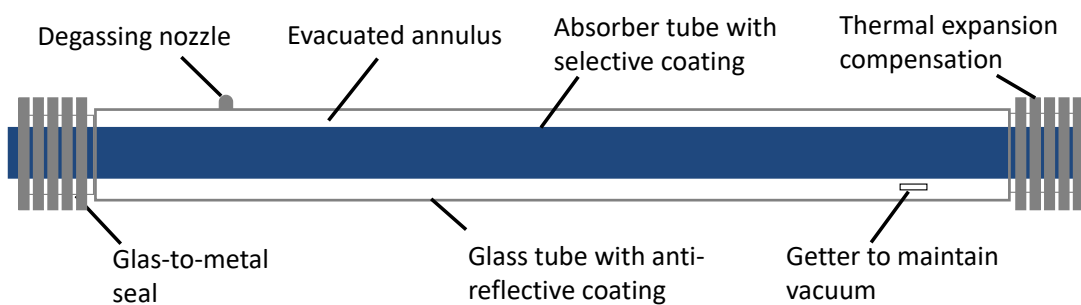


Figure 2.2.: Schematic set-up of a receiver/ absorber tube for parabolic trough collectors (Wehner, 2022, p. 15) and (Lovegrove and Stein, 2012, p. 210)

Parabolic trough power plants are commonly divided into three subsystems, the solar field, thermal storage and power block as can be seen in Figure 2.3. A solar field is composed of a multitude of parallel and in line arranged parabolic trough collectors. These collect the direct solar radiation, convert it into thermal energy in the receiver tube and transport it using a heat transfer fluid (HTF) from the solar field to a heat sink. In the power plant unit, thermal energy is converted into mechanical work by a Clausius-Rankine process in a steam turbine and into electrical energy by means of a generator. The steam power cycle is similar to conventional power plants. However,

wet cooling for condensation is a challenge for CSP power plants, as they are usually used in regions with water scarcity.

A major advantage of solar thermal power plants is the comparatively simple storage of thermal energy. Thermal storage enables to regulate the energy output of the fluctuating incident solar energy during cloud transients. It also enables operation during the night and increases the operating hours of the power plant unit. Depending on the configuration of the plant, the solar field feeds directly or indirectly into the storage unit and the power block is coupled to the storage. Thermal storage mostly works with molten salt in a temperature range of 390 °C for parabolic trough power plants. In addition to the storage tank, the HTF circulating in the solar field also provides inertia, which contributes to stable grid operation. For example a 50 MW parabolic trough power plant in Moron, Spain has about 330 tonnes of HTF in the system (Wehner, 2022, p. 129).

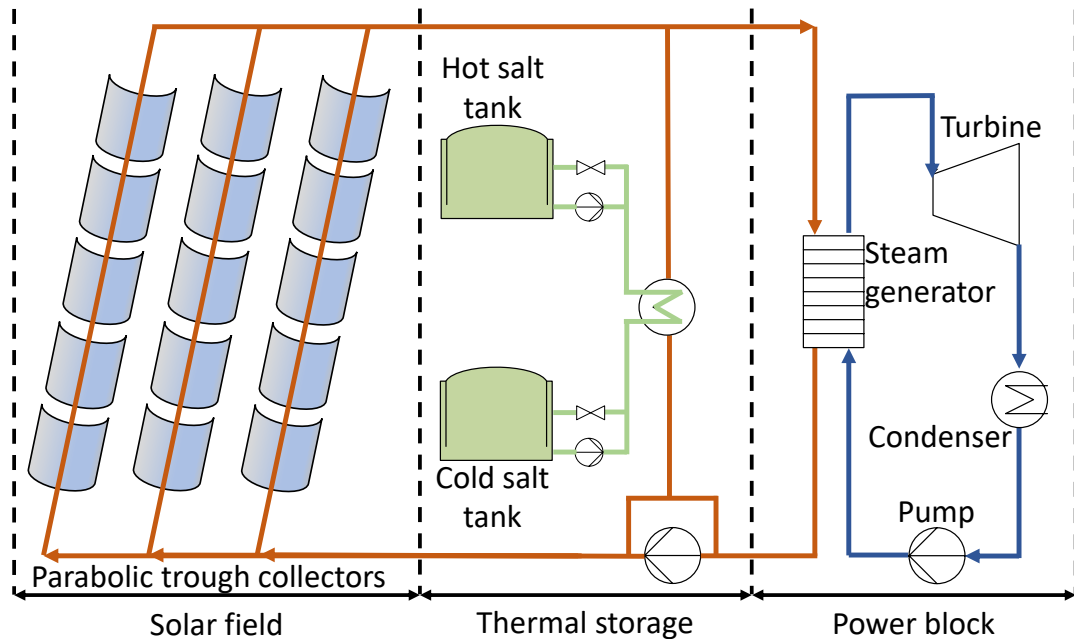


Figure 2.3.: Layout of a parabolic trough power plant with thermal storage and oil as heat transfer fluid (Hirsch, 2021, p. 2)

Typically, parabolic trough power plants use oil as heat transfer fluid and can be operated up to 400 °C. Here, the state of the art heat transfer fluid is BP/DPO, which is described in Chapter 2.4. PTCs are the main technology for large-scale concentrating solar power applications (Alexopoulos and Kalogirou, 2022, p. 44), in 2018, parabolic troughs accounted for 90 % of commercially operated solar thermal power plants (Chen et al., 2020, p. 2).

Solar thermal power plants have a capacity of 6 GW worldwide, with installed capacity in Spain of 2.3 GW (stagnating), 1.6 GW in the United States, 0.5 GW in Morocco, 0.5 GW in China and 0.5 GW in South Africa. Costs have fallen since large-scale market introduction in 2007 in the US and Spain and now reach values of around 6 ct/kWh under favourable boundary conditions. (Pitz-Paal et al., 2018, p. 88). However, other renewables such as PV offer lower LCOE¹ of below 3 ct/kWh, resulting in no new CSP projects in Spain at present. Morocco and the United Arab Emirates are at the leading of current CSP construction projects (Njore et al., 2021, p. 8).

To further reduce costs, research aims to increase the operating temperature and thus the efficiency. Digital technologies are also intended to optimise the operation and maintenance of the large solar fields (Pitz-Paal et al., 2018, p. 89). Since the 1980s, research and qualification has been carried out on concentrating solar thermal energy technologies at the Plataforma Solar de Almería (PSA).

¹Levelized Cost of Electricity

2.2. Plataforma Solar de Almería

The Plataforma Solar de Almería (PSA) was founded in 1980 as a cooperative project of nine international countries. The PSA is owned and operated by the Spanish research centre CIEMAT. The PSA is located in the Tabernas desert, in the province of Almería in Andalusia, Spain. The direct annual solar radiation is more than 1900 kWh/(m² year) with over 3000 hours of sunshine per year and the average annual temperature is around 17 °C. This provides optimal conditions for research on concentrating solar thermal energy.

In terms of its arid landscape, size, diversity and expertise, the Plataforma Solar de Almería is a unique research site for concentrating high-temperature solar technology worldwide. On the 100-hectare test site, differently shaped mirrors with an area of 20 000 square metres are installed. The PSA is equipped, among others, with the following testing facilities (DLR, 2023):

- Central receiver tower CESA-1 with 300 heliostats of 40 m² each and a tower height of 83 m
- Central receiver tower SSPS with 92 heliostats of 40 m² each and a tower height of 43 m
- Parabolic trough test system PROMETEO with two rows of 100 m length each
- Solar furnace with up to 3 MW/m² and temperature gradients up to 104 K/s
- 6 Dish-Stirling systems
- Desalination plant
- Optic laboratory for investigating the ageing behaviour of materials
- Measuring station for solar meteorology
- Rotatable test facility for parabolic mirrors KONTAS

A current research project at the parabolic trough system called PROMETEO (see Figure 2.4) at the PSA is the silicone fluid next generation (SING) project, which is explained in the next section.



Figure 2.4.: Aerial view of PROMETEO parabolic trough facility at Plataforma Solar de Almería

2.3. SING Project Objectives

The SING project "Silicon Fluid Next Generation" serves to demonstrate the thermo-physical properties and investigate the long-term behaviour of the silicone-based heat transfer fluid HXLP for CSP applications. The project is funded by the research programme of the Federal Ministry for Economic Affairs and Energy and is a joint project of several partners ². The SING project is developing an important basis for the widespread use of silicone-based heat transfer fluids in parabolic trough power plants. HELSIOL[®]XLP is a further developed silicone oil based on the previous product HELISOL[®]5A and follows on from previous projects such as SITEF (Silicone fluid Test Facility) and SIMON (Silicone Fluid Maintenance and Operation). The SING project has four central aspects (Hilgert, 2020, p. 3):

1. Demonstration of the advanced heat transfer fluid HXLP in a loop scale at 430 °C.
2. The international standardisation of silicone-based heat transfer fluids for CSP-applications.
3. The investigation of heat transfer properties under relevant operating conditions in loop scale and in the laboratory.
4. A mobile test stand for temperatures up to 480 °C to investigate key issues such as HTF degradation, pump durability, gas evolution and corrosion.

The PROMETEO facility at PSA is used for the demonstration in a loop scale up to 430 °C. The PROMETEO facility consists of two rows of parabolic trough collectors, each 100 metres long and divided into eight 12-metre PTC modules. The plant has an east-west orientation, which allows high temperatures to be achieved at the zenith throughout the year. The test loop is equipped with an air cooler as a heat sink and a temperature control bypass allows the cooling capacity to be adjusted to reach the desired temperature at the collector inlet.

To measure the heat capacity and the heat transfer coefficient, a measurement bypass is installed at PROMETEO, see Figure 2.5. The measuring bypass consists of a flow calorimeter for measuring the specific heat capacity. An optional section for calibrating the mass flow sensor at temperatures up to 300°C with laser Doppler anemometry (LDA). And a measurement heat exchanger for measurements of the specific heat transfer coefficient and for cooling the HXLP.

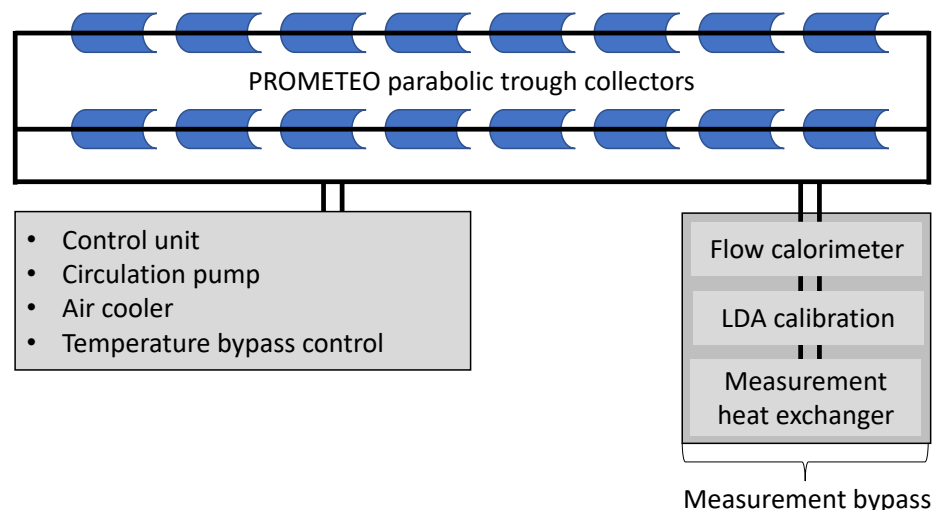


Figure 2.5.: Schematic of the measurement bypass at PROMETEO for measuring the specific heat capacity and heat transfer coefficient of HXLP

²DLR, Wacker Chemie AG, Dickow Pumpen GmbH & Co. KG, flucon fluid control GmbH, TÜV NORD EnSys GmbH & Co. KG, Senior Flexonics GmbH and CIEMAT

2.4. Heat Transfer Fluids

In concentrating solar power applications, the absorbed thermal energy needs to be transferred from the collector field, to use it or convert it into electricity at a different location. Therefore a heat transfer fluid (HTF) is used. In general, HTFs are primarily used as intermediate fluids to transfer heat from a heat source to the consumers (Mukund and Santanu, 2012, p. 675).

Heat transfer fluids have a decisive influence on the thermal efficiency and thus the economic profitability of solar power plants, which is why research and development is striving to improve their properties in order to reduce the cost of electricity. Desired characteristics for heat transfer fluids are a high heat capacity, as a lower mass flow is required to transport a certain thermal energy (Hilgert, Jung, et al., 2021, p. 49). This, as well as a low viscosity reduces the pressure drop resulting in a lower pumping capacity. Low vapour pressure enables operation at low design pressure, which saves costs for piping and equipment. Furthermore a high thermal conductivity improves the heat transfer behaviour. For a wide operating range, the HTF should have a melting point below the surrounding minimal temperature and a high boiling point. In addition to the physical properties, the thermal stability and low tendency to ageing and non-corrosive behaviour are also essential. A common degradation issue in CSP applications is the formation of hydrogen, which can diffuse at operating temperature through the absorber tube into the vacuum insulation. Due to the increased heat conduction, the heat losses increase. Additional desirable characteristics are low occupational and environmental risks for safe operation and handling for the environment and staff.

HTFs can be classified into six groups: Air and gas, water/steam, thermal oils, organics, molten salts and liquid metals (Vignarooban et al., 2015, p. 385). Typical HTFs for solar parabolic trough applications are shown in Figure 2.6.

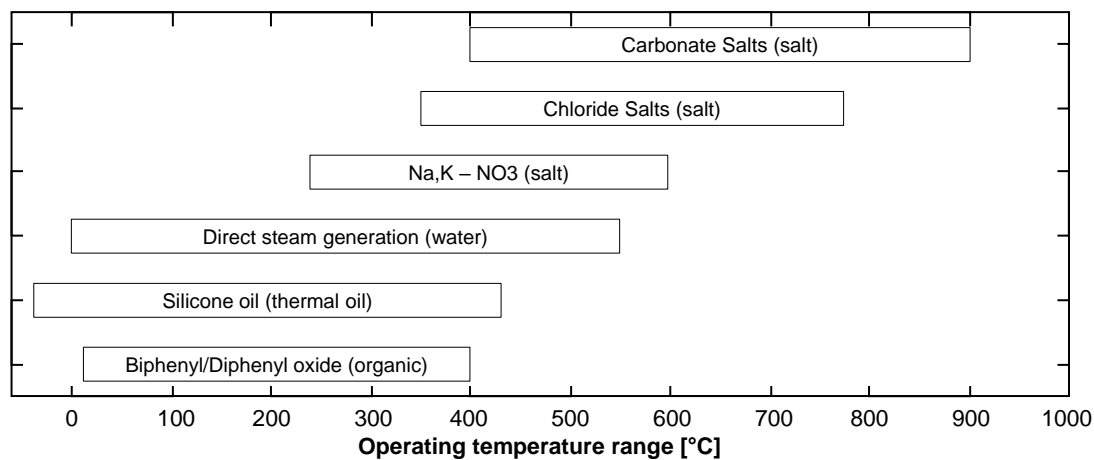


Figure 2.6.: Operating temperature for various heat transfer fluids and respective classes in solar parabolic trough applications (Hirsch, 2021, p. 5)

For commercial parabolic trough CSP plants, the eutectic mixture of biphenyl and diphenyl oxide (BP/DPO) as HTF is state of the art. Common products are Therminol[®] VP-1, Dowtherm[™] A or DIPHYL[®]. Due to improved fluid characteristics such as the maximum operating temperature and ecotoxicity as will be described in the following, silicone oil-based HTFs are the focus of research and the next section presents the most recent silicone oil from Wacker, HELISOL[®] XLP.

2.4.1. HELISOL[®] XLP

HELISOL[®] XLP is chemically a linear polydimethylsiloxane as can be seen on the left side of Figure 2.7 and thus it belongs to the group of silicone-based heat transfer fluids. HXLP is known to be a odourless, colourless and clear liquid with temperature stability (Wacker, 2022, p. 1). It can be operated at 430°C and has a steam pressure of 10.3 bar at 400°C. Further physical properties of laboratory data are given in Table 2.2 and Appendix A.

| Temperature [°C] | Viscosity [mPas] | Thermal conductivity [W/m ² K] | Density at 20 bar [kg/m ³] | Heat capacity at 20 bar [J/kg K] |
|------------------|------------------|---|--|----------------------------------|
| 25 | 12.25 | 0.1352 | 946.9 | 1470 |
| 430 | 0.46 | 0.0735 | 357.98 | 2452 |

Table 2.2.: Physical properties of HELISOL[®] XLP in use based on laboratory data by Wacker

At temperatures above 200 °C, rearrangement reactions of the silicone-oxygen bonds occur, forming linear and cyclic siloxanes. This process of equilibration proceeds until an equilibrium fluid composition is reached that remains stable during its lifetime (see Figure 2.7). As fluid properties such as viscosity, flash point and equilibrium vapour pressure change, silicone based HTF are referred to as "in use" after equilibration (Hilgert, Jung, et al., 2021, p. 9).

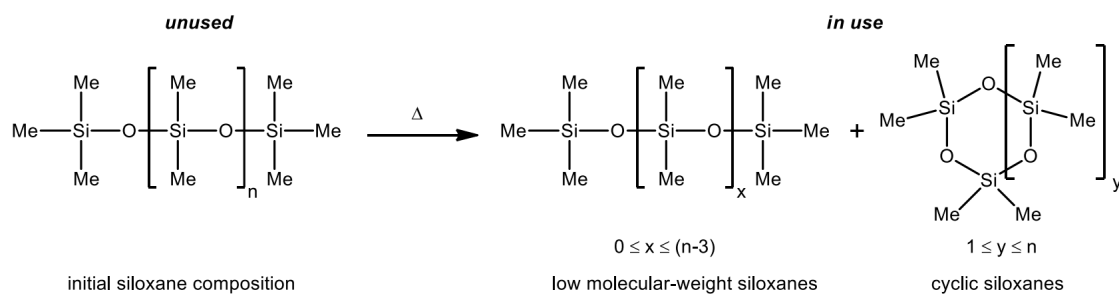


Figure 2.7.: Molecular structure of polydimethylsiloxane heat transfer fluids (Hilgert, Jung, et al., 2021, p. 9)

Silicone-based heat transfer fluids and HXLP in particular, have improved properties compared to the current benchmark BP/DPO as has previously been presented (Hilgert, 2020, p. 5):

- HXLP has a higher maximum operating temperature than BP/DPO (400 °C). This allows for higher steam temperatures, and therefore efficiencies, in the power blocks. Furthermore, the hot tank temperature in the thermal energy storage system can be raised, which lowers its volume and cost.
- BP/DPO forms substances such as benzene through thermal degradation during operation.
- The solidification point of BP/DPO at 12 °C requires a freeze protection system to prevent possible solidification of the HTF's in the piping system depending on the plant location. This requires investment and also reduces the overall revenue. HXLP solidifies at -40 °C.
- HXLP has a lower hydrogen formation rate at operating temperature. This is a cost reduction potential, as hydrogen from the HTF circuit can permeate into the vacuum ring of the absorber tubes and cause increased thermal losses (see previous chapter).
- Compared to BP/DPO, silicone oil-based HTFs are more thermally stable, which enables higher operation temperature or longer life time at the same temperature and keeps fluid properties such as viscosity constant over time.

2.5. Specific Heat Capacity

As can be deduced from the previous chapter, heat capacity is an essential physical property for HTFs. The isobaric specific heat capacity is defined as the amount of heat that must be added to a unit of mass at constant pressure, without a change of state in order to increase the temperature of the medium by one unit (Hannoschöck, 2018, p. 102).

The term heat is defined by the first law of thermodynamics.

$$\Delta U = \Delta Q + \Delta W \quad (2.1)$$

The change in the internal energy (ΔU) of a closed system is equal to the sum of the change in heat (ΔQ) and the change in work (ΔW) (VDI, 2013, p. 19). If heat is added to the system, the medium will expand according to the temperature increase as long as the pressure p is kept constant. With the formula of the specific enthalpy h related to the mass the energy balance results as (Hannoschöck, 2018, p. 102):

$$du = dq - p dv = dh - p dv - v dp \quad (2.2)$$

with the total differential of enthalpy:

$$dh = \left. \frac{\partial h}{\partial T} \right|_p dT + \left. \frac{\partial h}{\partial p} \right|_T dp = dq + v dp \quad (2.3)$$

The derivative of the specific enthalpy according to temperature at constant pressure is the heat capacity:

$$c_p = \left. \frac{\partial h}{\partial T} \right|_p dT = \left. \frac{dq}{dT} \right|_p = \left. \frac{1}{m} \frac{dQ}{dT} \right|_p \quad (2.4)$$

The heat capacity depends on two state functions $c_p(T; p)$. The dependence on temperature T is usually stronger than that on pressure p .

One way of measuring heat capacity is differential scanning calorimetry (DSC), which is mainly used in laboratories. Here, the heat flux between a material sample and a reference is measured and the heat capacity is determined. Another method is flow calorimetry, whereby the heat capacity can be measured continuously in a process. This method serves as the basis of this work for measuring the heat capacity. The measuring arrangement, as can be seen in Figure 2.8, consists of a temperature measurement at the input, a heat source, a temperature measurement at the output and a mass flow sensor. A heating rod is used as the heat source because the electrical energy can be measured with low uncertainty and dissipates completely into heat. Heat losses must be minimised by insulation, but the remaining losses can be quantified and taken into account in the calculation of the isobaric specific heat capacity in Equation (2.5).

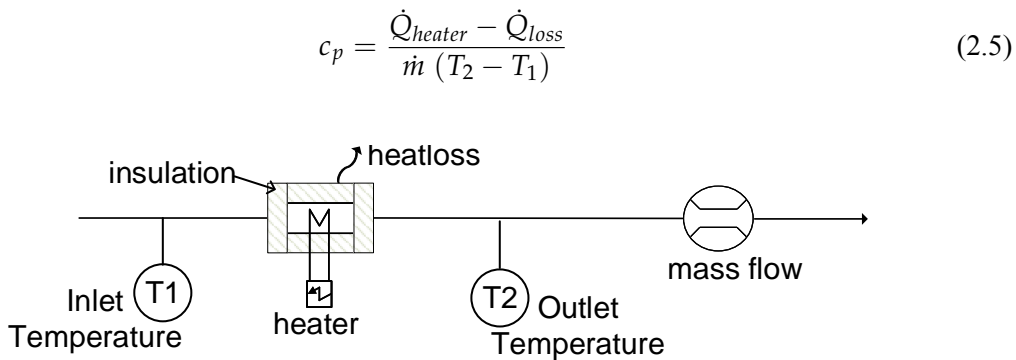


Figure 2.8.: Principle of flow calorimetry with temperature and mass flow measurement and heater

2.5.1. KONTAS-cp Flow Calorimeter

Based on the principle of flow calorimetry presented in the previous chapter, the flow calorimeter KONTAS-cp was developed by DLR to measure the specific heat capacity of HTF under operating conditions. The flow calorimeter was designed as a mobile measuring system for temperatures up to 350 °C. Figure 2.9 shows the sectional view of the measurement setup (Hilgert, Howar, et al., 2019, p. 807). The incoming fluid flow (blue arrows) is divided into two flows, the measurement flow and the protection flow (see below). The measurement flow passes through a static mixer to eliminate temperature inhomogeneities. Then the inlet temperature T_1 is measured. The heater consists of electric heating rods that heat up the fluid with a heat rate of up to 10 kW. Baffles in the heater ensure a defined and homogeneous flow and the cross-flow improves the heat transfer. The electrical power is measured by a power meter and the electrical cable losses are considered. In the output (red arrows) there is a further static mixer and the output temperature T_2 is measured. Next, the mass flow is measured in a Coriolis sensor.

The protection flow is used to eliminate heat losses from the measurement flow through the flange, through which the heating rods are introduced. Large heat losses would occur if the flow were in direct contact with the surface of the flange. However, since the fluid on both sides of the partition plate has practically the identical temperature, almost no heat loss occurs from the measurement flow. The flow calorimeter is further thermally insulated and unavoidable heat losses can be measured. The control and data acquisition is realised via a LABVIEW program that acquires and logs the measurement data every second.

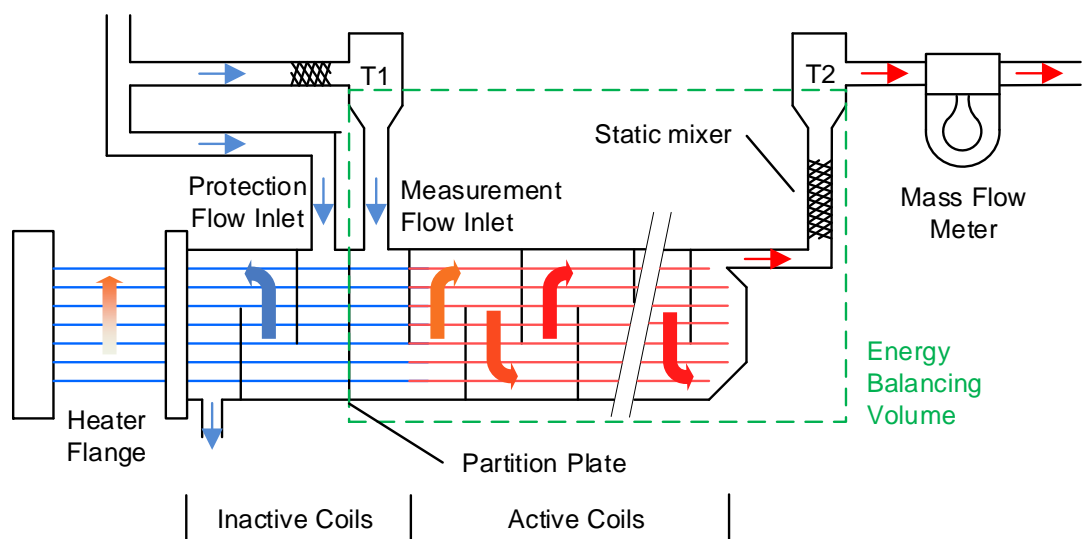


Figure 2.9.: Sectional view of the measurement setup, indicating the energy balance volume, flow directions and HTF temperatures (Hilgert, Howar, et al., 2019, p. 807)

Measurements with an uncertainty of 1.86 % at 329 °C were achieved . At elevated temperatures above 270°C, systematic deviations compared to the laboratory measurements were found, which can be assigned to the mass flow sensor (Hilgert, Howar, et al., 2019, p. 812). The range for the calibration of the mass flow sensor is between 20 °C - 90 °C, therefore measurements at temperatures far from calibration range show an increased uncertainty. The maximum operating temperature of the Coriolis sensor is limited to 350°C.

2.6. Heat Transfer

As introduced in the previous chapter, according to the first law of thermodynamics, the internal energy of a system can only be changed by the transport of energy across the system boundary, by work or heat. Heat is the energy that is transferred due to a temperature difference that exists between a system and its environment. The transport process related to the transfer of heat is called heat transfer (VDI, 2013, p. 19)

The second law of thermodynamics states that heat is always transferred from a body with a higher temperature to a body with a lower temperature. The heat transferred per unit of time is referred to as the heat flow rate \dot{Q} [W]:

$$\dot{Q} = \frac{dQ}{dt} \quad (2.6)$$

per unit of area:

$$\dot{q} = \frac{d\dot{Q}}{dA} \quad (2.7)$$

In principle, three types of heat transport are distinguished:

Conduction is based on the transport of energy among molecules between an existing temperature gradient (VDI, 2013, p. 19). If there is a local temperature gradient $\delta T / \delta x$ in the direction of the spatial coordinate x , the heat flux for pure heat conduction depends only on the thermal conductivity of the material λ [W/(K m)]. Fourier's law can be stated in general as follows:

$$\dot{q} = -grad(\vartheta)\lambda \quad (2.8)$$

for one dimension:

$$\dot{q} = -\lambda \frac{\partial \vartheta}{\partial x} \quad (2.9)$$

Convection refers to the transport of energy in flowing fluids. A distinction is made between forced convection, if the flow is forced by external means, e.g. pumps or fans and free convection, if the fluids motion is caused by density changes referring to the buoyancy effect, when warm fluid rises and cold fluid falls (Bahrami, 2009, p. 1). Convective heat transport therefore depends not only on the physical characteristics of the fluid, but also on process parameters such as the flow velocity or the degree of turbulence (VDI, 2013, p. 20). The heat transfer is always based on the heat conduction in the flow boundary layer or thermal boundary layer (Böckh and Wetzel, 2015, p. 3) which can be seen in Figure 2.10.

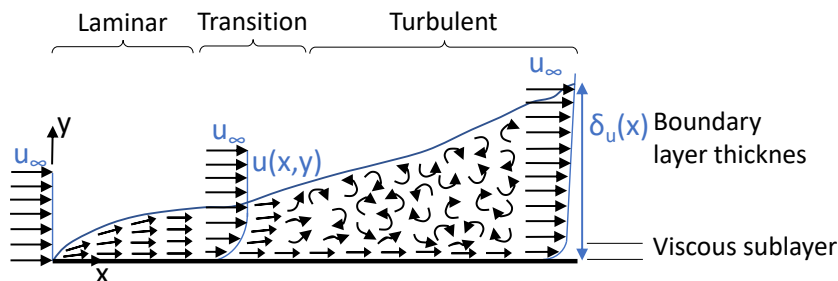


Figure 2.10.: Development of the boundary layer over a wall with the different flow regimes (Bahrami, 2009, p. 2)

Figure 2.10 shows a forced convection and the flow profile for a parallel flow close to the wall with the length L . For the heat transfer, the surface temperature ϑ_w of the wall, which is assumed to be homogeneous, as well as the temperature distribution $\vartheta(x, y)$ and the velocity

distribution $u(x, y)$ in the fluid near the wall $y = 0$ are decisive. Directly at the wall no slip condition applies, the fluid has a disappearingly low velocity of $u(x, 0) = 0$ and the same temperature as the plate surface $\vartheta(x, 0) = \vartheta_w$ (Kugi et al., 2016, p. 73). Far away from the wall, the fluid temperature ϑ_f and the flow velocity w_f rule. Above the wall, velocity and temperature gradients form boundary layers with a characteristic temperature and velocity profile are present. The thickness of the thermal boundary layer δ can be approximately equated to the thickness of a fictive, immobile fluid boundary layer (Kerskes, 2021, p. 16) in which by means of pure heat conduction at the same temperature difference $\vartheta_w - \vartheta_f$ the same heat flux \dot{q} would be induced as in convective heat transfer.

$$\left. \begin{aligned} \dot{q}_{conv} = \dot{q}_{cond} &= -\lambda \frac{\partial \vartheta}{\partial y} \Big|_{y=0} \\ \dot{q}_{conv} &= \alpha (\vartheta_w - \vartheta_f) \end{aligned} \right\} \alpha = \frac{-\lambda \frac{\partial \vartheta}{\partial y} \Big|_{y=0}}{\vartheta_w - \vartheta_f} \quad (2.10)$$

Therefore the following equation is relevant for convective heat transfer with the heat transfer coefficient $\alpha [W/m^2K]$.

$$\dot{q} = \alpha (\vartheta_w - \vartheta_f) \quad (2.11)$$

Since the heat transfer coefficient varies along the flow direction, the mean heat transfer coefficient is of particular interest (Kugi et al., 2016, p. 74). Table 2.3 shows typical alpha values for various flow conditions.

| | | |
|--------------|--------------------|----------------------------------|
| 2-25 | W/m ² K | free convection in gases |
| 10-1000 | W/m ² K | free convection in liquids |
| 25-250 | W/m ² K | forced convection in gases |
| 50-20 000 | W/m ² K | forced convection in liquids |
| 2500-100 000 | W/m ² K | for condensing or boiling fluids |

Table 2.3.: Typical heat transfer coefficient values for different heat transfer situations (VDI, 2013)

Various dimensionless numbers are necessary for calculating convective heat transfer: The **Reynolds-number (Re)** is the ratio of the inertial forces to the frictional forces. It indicates whether a flow is laminar or turbulent.

$$Re = \frac{u L}{\nu} \quad (2.12)$$

with:

- u – Average flow velocity [m/s]
- L – Characteristic length [m]
- ν – Kinematic viscosity [m²/s]

2. Fundamentals

To better estimate the gradient in the velocity boundary layer and the thermal boundary layer, the **Prandtl (Pr)** number is used. This is the ratio between the viscosity and the thermal conductivity.

$$Pr = \frac{\eta c_p}{\lambda} \quad (2.13)$$

with:

- η – Dynamic viscosity [Pa s]
- c_p – Specific heat capacity [J/kg K]
- λ – Thermal conductivity [W/m K]

The ratio of convection to heat conduction in the same fluid layer is given by the **Nusselt number Nu** thus describes the increase of heat transfer by convection.

$$Nu = \frac{\alpha L}{\lambda} \quad (2.14)$$

Radiation is based on electromagnetic waves and is independent of a transport medium and thus also travels in a vacuum. The radiation intensity depends on the temperature of the body and the emissivity of its surface. The heat flux emitted by a body can be calculated using the Stefan-Boltzmann law:

$$\dot{q} = \epsilon \sigma T^4 \quad (2.15)$$

with:

- ϵ – Emissivity of the surface ($0 \leq \epsilon \leq 1$)
- σ – Stefan-Boltzmann constant 5.6710^{-8} [W/m² K⁴],
- T – Temperature of the emitting body [K]

2.7. Double Pipe Heat Exchanger

A heat exchanger is a device that transfers thermal energy from one fluid to another. The fluids are physically separated from each other and the heat is transferred through a wall. There are different types of heat exchangers, such as shell - tube or plate heat exchangers, double-pipe heat exchangers and others. A very simplest type is the double pipe heat exchanger. This consists of two concentric pipes. For example, the warm fluid flows through the inner pipe and is cooled by a medium in the shell area or concentric annular gap. By placing the cooler medium in the shell area, heat losses can be reduced. In addition to the design, heat exchangers can be differentiated by their flow direction. A distinction is made between parallel flow, counterflow and crossflow (Heidemann, 2022, p. 17). Figure 2.11 shows the schematic of a double pipe in counterflow arrangement.

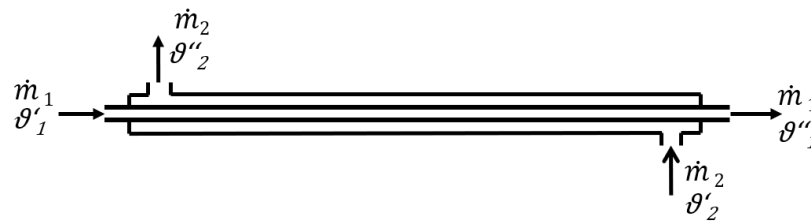


Figure 2.11.: Schematic drawing of counter flow double pipe heat exchanger

The transferred heat in a heat exchanger depends on the heat transmission coefficient k , the exchange surface A and the mean logarithmic temperature difference $\Delta\vartheta_{ln}$ (LMTD) as can be seen in the formula given:

$$\dot{Q} = k A \Delta\vartheta_{ln}; \quad (2.16)$$

with the mean logarithmic temperature difference:

$$\Delta\vartheta_{ln} = LMTD = \frac{\vartheta_{max} - \vartheta_{min}}{\ln \frac{\vartheta_{max}}{\vartheta_{min}}}; \quad (2.17)$$

The temperature curve in the counterflow is shown in 2.12.

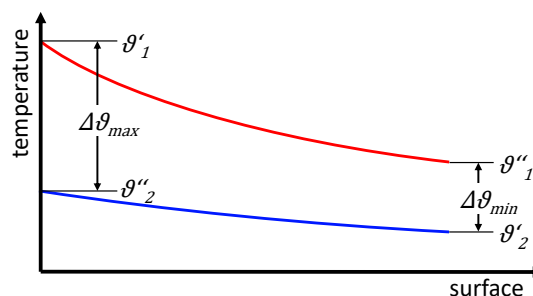


Figure 2.12.: Temperature profile of a counterflow heat exchanger with concave profile

In Equation (2.17), the heat transmission coefficient k [$W/m^2 K$] is used, because in real heat transport problems, heat conduction in a solid and convective heat transfer in a fluid boundary layer at the surface of the solid are usually coupled with each other, as can be seen in the Figure 2.13 (VDI, 2013, p. 33). It is related to the total thermal resistance R , which combines the individual thermal resistances for heat transfer mechanisms in different layers. For a multilayer cylinder wall,

2. Fundamentals

the thermal resistance consisting of conductive and convective parts can be calculated as follows (Kerskes, 2021, p. 21):

$$R = \frac{1}{k A_r} = \underbrace{\frac{1}{\alpha_1 A_1}}_{\text{convection inner pipe}} + \underbrace{\sum_{i=1}^n \frac{\ln \frac{r_{i+1}}{r_i}}{\lambda_i 2 \pi L}}_{\text{conduction}} + \underbrace{\frac{1}{\alpha_2 A_2}}_{\text{convection outer pipe}} \quad (2.18)$$

The heat transfer coefficient refers to a reference area A_r , whereby the outer surface of pipes is used for standardisation (VDI, 2013, p. 49). While the conductive part of formula 2.18 is calculated by the geometry and thermal conductivity, the convective parts have to be calculated separately according to the operating conditions. The procedure for calculating the convective heat transfer in a double pipe heat exchanger is described in the next section.

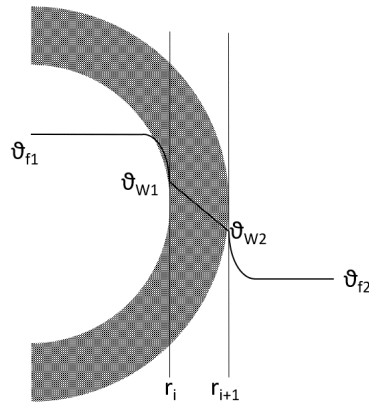


Figure 2.13.: Temperature profile through a pipe wall with convective and conductive heat transfer

2.8. Calculation Method for Convective Heat Transfer

The flow in the pipe affects the heat transfer and is divided into laminar and turbulent for characterisation and calculation of the flow behaviour. In this particular case, for a Reynolds number less than 2300, the flow is considered laminar. From $Re > 10^4$, fully turbulent flow prevails. At $2300 < Re < 10^4$, it is classified as transitional. In this thesis, only turbulent flow is covered.

For the applicability of the Gnielinski method, several criteria have to be fulfilled (Kandlikar and Shah, 1989, p. 301).

1. The flows are always considered idealised with regard to their flow direction
2. The heat exchanger is in a steady state.
3. Kinetic and potential energies are neglected. Also heat losses to the environment
4. There is no heat conduction in the direction of flow.
5. All material properties as well as the heat transfer coefficient are constant over the heat exchanger; for this purpose, appropriate average values are calculated.

The established Gnielinski method for calculation is described in the VDI heat atlas and is based on the assumption of a constant wall temperature and averaged heat transfer coefficient α over the length of the apparatus. A double pipe heat exchanger consists of a flow-through pipe and an concentric annular gap, for each case, the heat transfer coefficient α can be calculated as follows.

2.8.1. Heat Transfer in Pipe Flow

In a first step, the Nusselt-number for constant wall temperature is calculated:

$$Nu_{m,T} = \frac{(\zeta/8) Re Pr}{1 + 12.7 \sqrt{\zeta/8} (Pr^{2/3} - 1)} \left[1 + \left(\frac{d_i}{l} \right)^{2/3} \right] \quad (2.19)$$

with the friction factor for turbulent flow in pipes:

$$\zeta = (1.8 \log Re - 1.5)^{-2} \quad (2.20)$$

In order to take into account the temperature dependency of the medium properties, the direction of the heat flux (heating or cooling) is taken into consideration by calculating the Prandtl number Pr_w (see equation: 2.13) at the wall temperature. The Nusselt number is corrected with the following factor:

$$Nu = Nu_{m,T} \left(\frac{Pr}{Pr_w} \right)^{0.11} \quad (2.21)$$

For the calculation of the heat transfer coefficient in the pipe flow, the Equation 2.14 can be rearranged and the inner diameter d_i is chosen as the characteristic length. Hence applies:

$$\alpha = \frac{Nu \lambda}{d_i} \quad (2.22)$$

2.8.2. Heat Transfer in Concentric Annular Gap

The heat transfer in the annular gap at constant wall temperature can be calculated for different boundary conditions. For the double-tube heat exchanger, the heat transfer is from the inner tube, with the outer tube being thermally insulated. The characteristic length in an annular gap is the hydraulic diameter with the inner diameter of the outer pipe D_i and the outer diameter of the inner pipe d_a .

$$d_h = D_i - d_a \quad (2.23)$$

$$Nu_{m,T} = \frac{(\zeta_{ag}/8) Re Pr}{k_1 + 12.7 \sqrt{\zeta_{ag}/8} (Pr^{2/3} - 1)} \left[1 + \left(\frac{d_h}{l} \right)^{2/3} \right] \quad (2.24)$$

With:

$$k_1 = 1.07 + \frac{900}{Re} - \frac{0.63}{1 + 10 Pr} \quad (2.25)$$

The pressure loss coefficient of a flow-through annular gap depends on the diameter ratio:

$$a = \frac{d_i}{d_a} \quad (2.26)$$

Which results in the pressure loss coefficient as follows:

$$\zeta_{ag} = (1.8 \log Re^* - 1.5)^{-2} \quad (2.27)$$

With:

$$Re^* = Re \frac{[1 + a^2] \ln a + [1 - a^2]}{[1 - a]^2 \ln a} \quad (2.28)$$

2.9. Uncertainty Estimation

In order to assess the reliability of the results of a measurement of a physical quantity, it is essential to specify the quality of the result in the form of a quantitative tolerance. With an uncertainty specification, different measurement results can be compared and discussed. In the following, the calculation of the uncorrelated total uncertainty is described using the "Guide to the expression of uncertainty in measurement" by the Joint Committee for Guides in Metrology (BIPM, 2008).

For the calculation of the measurement uncertainty of the measurand Y , a function f is set up that contains all input variables x_N that have an impact on the measurement:

$$Y = f(x_1, x_2, \dots, x_N) \quad (2.29)$$

For a combined uncertainty $u_c(Y)$, all input variables x_N and its associated uncertainty $u(x_N)$ are taken into account. The associated standard uncertainty $u(x_N)$ can be determined in two different ways:

Type A uncertainty of repeated measurements at the identical conditions.

In most cases, the best available estimate of the expected value is the arithmetic average \bar{q} of n observations:

$$\bar{q} = \frac{1}{n} \sum_{k=1}^n q_k \quad (2.30)$$

To characterise the dispersion around its mean value \bar{q} , the experimental standard deviation $u(\bar{q})$ is obtained from the positive square root of the variance:

$$u(\bar{q})_{TypeA} = \sqrt{\frac{1}{n(n-1)} \sum_{k=1}^n (q_k - \bar{q})^2} \quad (2.31)$$

Type B uncertainty from available information like calibration certificates, device specifications, literature or from previous measurements. The given Gaussian distributed standard deviation σ of the manufacturer can be taken for $u(x_N)_{TypeB}$.

For uncorrelated input variables, the standard uncertainty of the measurand Y is calculated by combining the standard uncertainties of the input estimates (x_1, x_2, \dots, x_N) . This combined standard uncertainty is denoted as $u_c(Y)$.

$$u_c(Y) = \sqrt{\sum_{i=1}^N (c_i u(x_i))^2} \quad (2.32)$$

The sensitivity coefficients c_i are determined by partial derivation:

$$c_i = \frac{\partial f}{\partial x_i} \quad (2.33)$$

If the standard uncertainty is known to be composed of components from both Type A and Type B assessments, the combined uncertainty from Type A and Type B can be calculated using the root-sum-of-squares (RSS) (Kuyatt and Taylor, 1994, p. 18).

3. Design of the Measurement Bypass

This section describes the design of the measurement bypass at PROMETEO and the major implementations to the system in order to achieve the aim of measuring the specific heat capacity and the heat transfer coefficient of HXLP at temperatures up to 430 °C with uncertainty below 1.5 %

3.1. Enhancement of the Existing Flow Calorimeter

The increase of the measurement temperature implied several modifications to the existing flow calorimeter setup, mainly for technical reasons. The design of the energy balance itself was not changed, apart from the optional HTF cooler between the outlet temperature measurement and the Coriolis mass flow sensors of the flow calorimeter. In order to measure mass flow at a lower temperature, as the uncertainty increases with the temperature (Hilgert, Howar, et al., 2019, p. 812) and it can only be operated up to 350°C. The position of the Coriolis sensor was adjusted for better measuring conditions. Since the measuring principle is based on two parallel measuring pipes that are activated to oscillate, an inlet section with a length of 5-10 tube diameters and 3-5 tube diameters for the downstream should be ensured (Küppers, 2004). This serves to guarantee an undisturbed and equal distribution of the mass flows through the two measuring pipes. In addition, a flexhose on the downstream side reduce possible stresses on the sensor. To protect the Coriolis sensor from excessive operating temperatures, two redundant temperature sensors are installed downstream the Coriolis sensor and an automatic valve closes if the temperature reaches the limit. A pressure sensor is integrated in the flow meter to determine the pressure dependencies of the thermophysical fluid properties.

Furthermore an optional calibration section for inline LDA measurements was implemented. For this purpose, the connection flanges between the outlet temperature measurement and the mass flow sensor are used to connect a measurement section for calibration. The measurement section can be operated independently or intermediately between the heat exchanger and the flow calorimeter. The technical adaptations and considerations of the measurement bypass can be seen in the piping and instrumentation diagram (PID), see Figure 3.1.

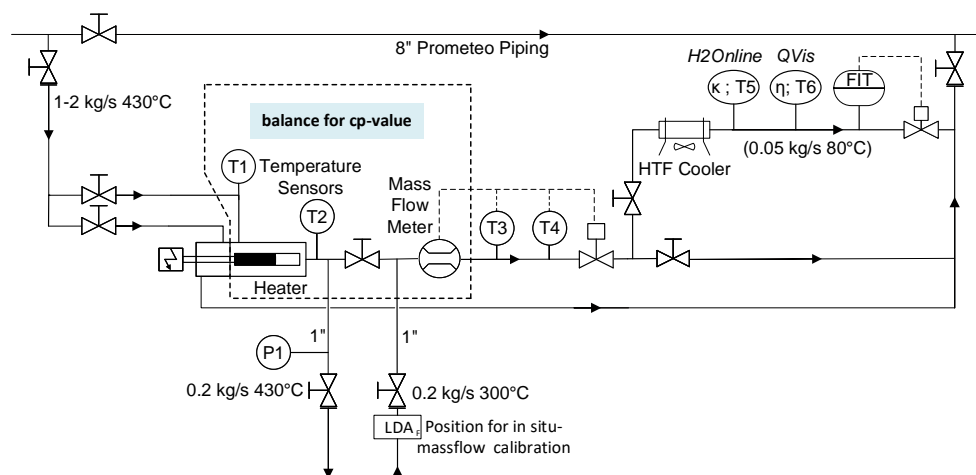


Figure 3.1.: Simplified PID of the enhanced flow calorimeter at the PROMETEO measurement bypass

3. Design of the Measurement Bypass

The technical adjustments associated with the replacement of the pipes with adequate material lead to a pipe design that combines several advantages. The connection flanges for the heat exchanger and the LDA calibration section are designed to place the Coriolis sensor in line with the calibration reference window (see Chapter 3.2.2). The pipe design and the support positions are chosen in order to enable the flow calorimeter to be connected at PROMETEO or the previous KONTAS system. Furthermore, valves and connections for an additional measurement section are integrated. In this measurement section, a small partial flow is cooled to 80°C for the optional measurements of the viscosity and water content of the HTF.

As the adaptations of the calorimeter are comparable to a new construction, a stress analysis of the pipes of the measurement set-up (Chapter 3.1.1) and validation measurements with water (Chapter 4.1) are carried out to ensure the functionality and low uncertainty.

3.1.1. Stress Analysis for Adapted Pipes

For the safe and functional operation of the flow calorimeter, a stress analysis of the pipes was carried out. The operating data of the PROMETEO system show that the operating pressure is approx. 20 bar and thus PN40 is suitable for operation temperatures up to 430 °C. Since the starting and shutting down of the system and changes in the operating points induce thermal stresses, the pipe supports must be carefully designed for safe operation. The pipe stress analysis was carried out using ROHR2, a software for static and dynamic stress analysis, specialised and optimised for piping. A model with 107 nodes was created. The piping material is 1.7335, a pressure of 20 bar, a temperature of 430 °C and a density of 370 kg/m³ were used to calculate the stresses in the operating case.

To classify the different cases of load, the calorimeter was divided into three sections in which different temperatures can occur, depending on the operating point, see Figure 3.2. The green section refers to the thermal protection flow, which has the same temperature as the inlet temperature of the measuring bypass. The blue section represents the heater in which the temperature of the fluid is increased. The yellow section contains the mass flow sensor and the prevailing temperature depends on the operating condition.

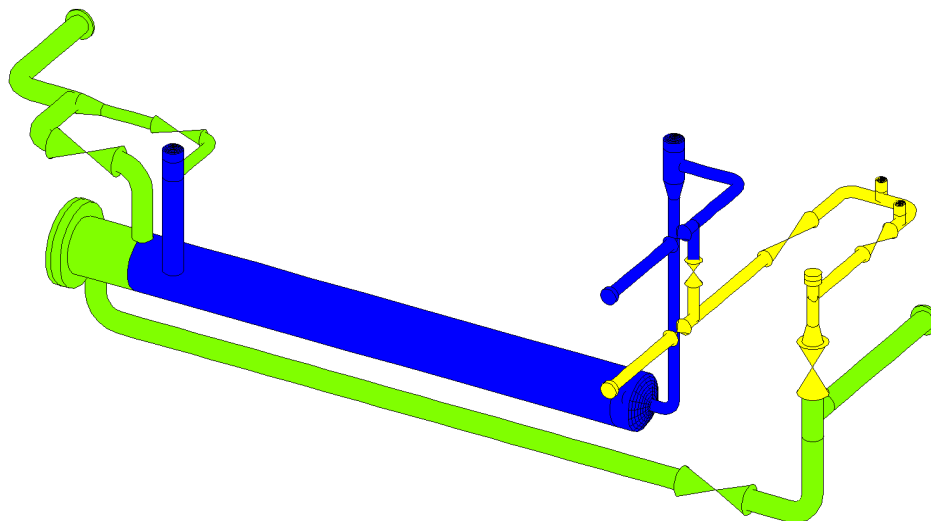


Figure 3.2.: Thermal sections of flow calorimeter for stress analysis, green: thermal protection flow; blue: heating section; yellow: massflow measurement section

The following cases result from the operating options and the three sections:

- case 1** Operation with the heat exchanger; same inlet conditions in the heater and thermal protection flow, but lower temperature in the massflow measurement section
- case 2** Operation without the heat exchanger; same temperature in the heater, thermal protection flow and massflow section.
- case 3** Operation with closed automatic valve; only thermal protection flow is on operating temperature
- case 4** Operation of only the heater to stabilize the temperature, therefore closed protection flow

In addition, the software performs a pressure test, which calculates the strength at increased pressure. The pressure test is carried out with water and at least 1.3 times the nominal pressure (Günthert and Faltermaier, 2018) is used to test the tightness of the pipes and flange joints.

The operating temperatures are shown in the Table 3.1. It should be noted that in case 3 an extreme value of 20°C was assumed for the closed automatic valve. If the valve closes during operation, it starts to cool down. The temperature will not reach the ambient temperature of 20 °C, as the test stands are controlled by the operator and a branch with insulation requires a significant amount of time to cool down

| case | heater | massflow measurement | thermal protection flow | max. utilisation of strength |
|------|--------|----------------------|-------------------------|------------------------------|
| 1 | 450°C | 300°C | 430°C | 41.1% |
| 2 | 350°C | 350°C | 330°C | 46% |
| 3 | 20°C | 20°C | 430°C | 42.5% |
| 4 | 430°C | 300°C | 20°C | 42.8% |

Table 3.1.: Temperatures in the thermal sections for different operation points

The results (See appendix B.1) and the right column in Table 3.1 shows that with the designed isometry, the permissible strength is not exceeded in all operating cases and safety is ensured. In addition, it should be taken into account that the extreme temperature differences will not occur in real test operation. If a line is at an operating temperature of 20°C, it cannot be flown through with hot silicone oil, otherwise temperature shocks will damage the electromechanical components of the Coriolis sensor. The sensor manufacturers recommend a temperature change of less than 1 K/s (Küppers, 2004).

The next step is to calculate the pipe stress of the entire bypass system of the PROMETEO plant. For the measurements, a bypass leads from the 8" main pipe to a paving on which the measuring devices are placed. The outlets of the bypass are made flexible by flexhoses, which minimises pipe stresses. Since the pipes expand thermally parallel to the flow calorimeter from the outlet to the inlet, the logic of the pipe supports was reconsidered and the outlet of the calorimeter is designed as a fixed support and the inlet as a guided support. Simulations of the pipe formation, see Appendix B.5) show that with this design, there are only minor stresses in the entire system.

3.2. Design of the Measurement Heat Exchanger

For the design of the measurement heat exchanger the double pipe design was chosen, as the design is geometrical simple and can thus be easily compared to existing equations. Its size is dominated by the output of an initial sensitivity analysis indicating the favourable ranges of the measurands. The double pipe heat exchanger is equipped with a pressurised cooling water circuit, for a heat transfer from the HTF in the inner pipe to water in the annular gap. The schematic design of the final measurement heat exchanger is given in Figure 3.3. The measurement heat exchanger contains temperature measuring locations (TML) with fourfold redundant temperature sensors at the respective inlets and outlets. A 70 mm long static mixer eliminates possible temperature inhomogeneities in front of the TML. The heat transfer from HXLP to the cooling water takes place in the area of the double pipe. Since a static mixer increases the degree of turbulence, the downstream static mixer is outside the heat transfer surface of the double tube and therefore does not influence the heat transfer. The temperature differences between the inner and outer pipe inevitably lead to thermal stresses, which have to be compensated by a technical solution that has unavoidable impact on the measurement. Thus a special stuffing box was designed in order to minimize the systematic influence in the measurement.

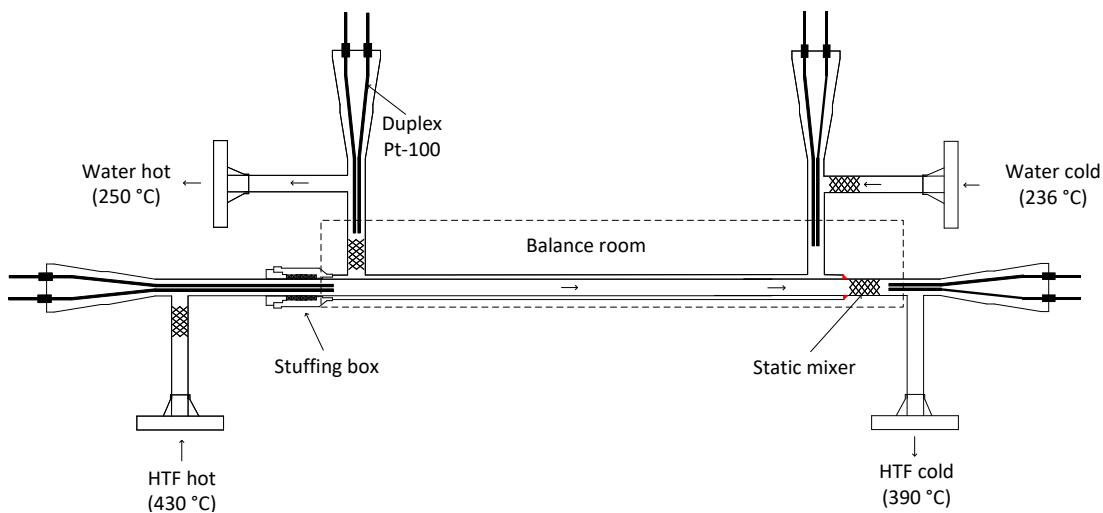


Figure 3.3.: Schematic design of the measuring heat exchanger with temperature measuring chambers, precision tubes, static mixers and stuffing box.

The underlying assumptions for the measurement heat exchanger is a HTF flow velocity of approx. 1.6 m/s in order to have a similar flow regime of receivers. In the literature, velocities of 1.3 m/s (Lüpfert et al., 2003) to 2.3 m/s (Wehner, 2022) for the wide-spread EUROTROUGH collectors is given. At a similar Re number, the corresponding mass flow of 0.2 kg/s in the measurement heat exchanger is suitable and enables also a measurement point of the flow calorimeter with low uncertainties.

The measurement heat exchanger is integrated into the measuring bypass, the PID (see Figure 3.4) shows the relevant components and interactions. The heat exchanger is connected to the flow calorimeter see Figure 3.1. Starting from the inlet of the heat exchanger, the HTF (red line) flows into the measurement heat exchanger and its temperature is measured before it transfers heat to the cooling water in the annular gap, using the counter flow principle. On the outside of the measuring heat exchanger, several temperature sensors are installed at defined locations around the circumference in order to measure the temperature on the surface and its spatial distribution. To obtain the differential temperature, the temperature is measured at the outlet. For the cooling water, the respective inlet and outlet temperatures are measured as well. After the measurement heat exchanger, further cooling takes place in three subsequent heat exchangers of the same geometry

without measuring instrumentation and the HTF flows back to the Coriolis sensor in the flow calorimeter. If necessary, two of the passes downstream can be bypassed to reduce the cooling capacity. For the calculation of the heat transfer, the pressure drop is used, which can be calculated and measured as a comparison for a lower uncertainty. In the measurement heat exchanger the TML dominate the total pressure loss. For this reason the pressure drop is measured by a differential pressure sensor over the length of the inner pipe in the second heat exchanger of the same design.

The lower part in the PID consists of the pressurised water cooling circuit. This has the overall task of cooling the HTF. The water is pressurized to 80 bar, hence it remains in a liquid state at the prevailing temperatures of 200-250 °C. In addition, its temperature control loop enables a constant inlet temperature of the water. A water to water heat exchanger lowers the temperature in the area of the mass flow sensor and the pump, enabling them to be operated at 60 °C. Thus, the Coriolis sensor can be operated in the range of calibration at temperatures of 20 °C - 90 °C and measure with a low uncertainty.

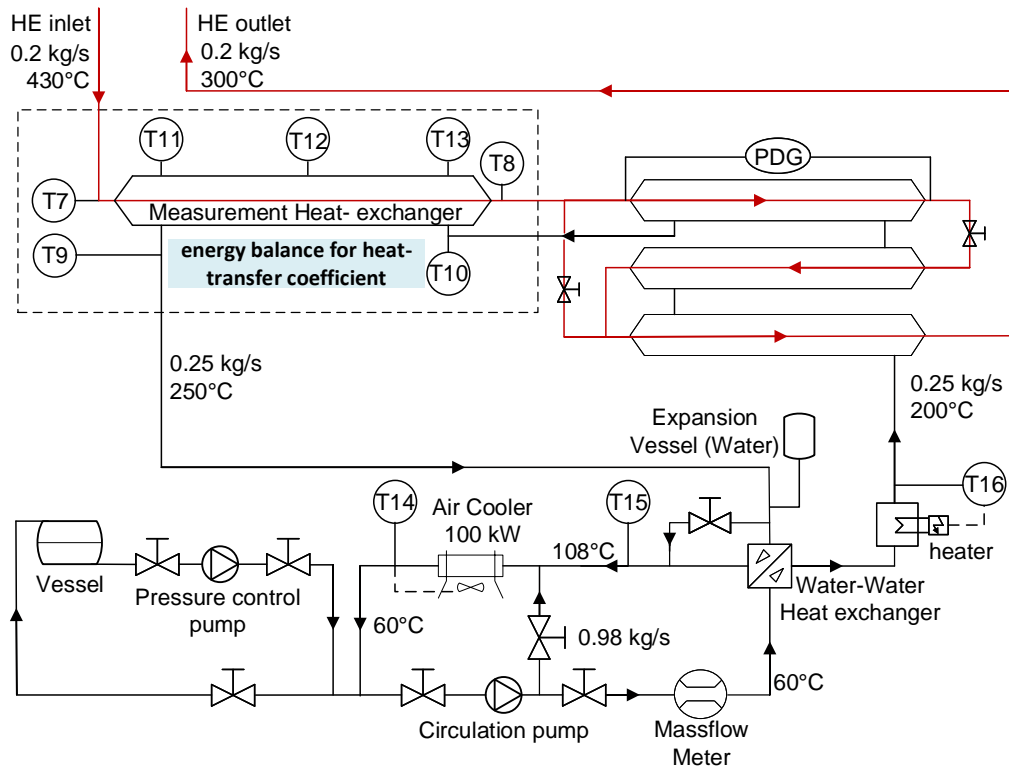


Figure 3.4.: Simplified PID of measurement heat exchanger bypass with pressurized water for cooling the heat transfer fluid

The influencing parameters were first identified using the relevant formulas for calculating the heat transfer in the double-tube heat exchanger. The relevant parameters are derived from the equation of the energy balance:

$$\dot{Q}_{W-HTF} = \dot{m} \cdot c_p \cdot (T_2 - T_1) - Q_{loss} \quad (3.1)$$

$$\dot{Q}_{W-HTF} = k \cdot A_2 \cdot \Delta\vartheta_{ln} \quad (3.2)$$

The heat flow \dot{Q}_{W-HTF} which represents the transferred heat in the measurement heat exchanger, can be equated in the Formula 3.1 and 3.2 for the determination of the heat transmission coefficient k :

$$k = \frac{\dot{m} \cdot c_p \cdot (T_2 - T_1) - Q_{loss}}{A_2 \cdot \Delta\vartheta_{ln}} \quad (3.3)$$

3. Design of the Measurement Bypass

With the heat transmission coefficient k , the heat transfer coefficient $\alpha_{HXL P}$ can be calculated:

$$\alpha_{HXL P} = \frac{d_a}{d_i \cdot \left(\frac{1}{k} - \frac{d_a \ln \frac{d_a}{d_i}}{2 \lambda_{steel}} - \frac{1}{\alpha_{water}} \right)} \quad (3.4)$$

Formulas 3.3 and 3.4 contain the relevant parameters that are necessary for the determination of the specific heat transfer coefficient. The output of the uncertainty analysis, which is presented in detail in Chapter 5, states a strong influence of the temperature measurement and the geometry on the overall uncertainty, placing it in focus. The importance of heat losses is primarily in the applicability of the formulas and methodology, because depending on the quantity of heat losses, the formulas are no longer valid. Furthermore, variable heat losses caused by the surroundings are difficult to quantify and thus increase the uncertainty.

The design and implementation of the five sensitive measurands as: temperature measurement, geometry, mass flow measurement, stuffing box and heat losses are described in detail individually in the following sections.

3.2.1. Temperature Measurement in the Heat Exchanger

Pt100¹ sensors with accuracy class 1/10 DIN B are used in four-wire circuit. The accuracy class 1/10 DIN B refers to the uncertainty specifications of DIN EN 60751 which is given as $\pm 0.03\text{K} + 0.0005 * t\text{K}/^\circ\text{C}$. Using the four-wire circuit of Pt100 sensors, the resistance of the connecting cables can be subtracted up to the platinum measuring resistor. This means that the cable length and changing environmental conditions have no influence on the temperature measurement. A total of four Pt100 sensors per measurement point are used. Due to the duplex design, two Pt100 measuring resistors can be combined in one sensor head, so that two duplex resistance thermometers per measuring point are integrated in the heat exchanger, For greater confidence in the temperature measurement. With the redundant measurement, the different temperatures readings can be compared and averaged, and continued operation is possible in case of failure of individual sensors.

The inlet and outlet pipes as well as the inner pipe of the measurement heat exchanger have the diameter DN15, therefore a measuring chamber with increased installation volume is needed for the integration of the sensors. The basic construction (see Figure 3.5) is a T-piece, two concentric reducers and a blind flange for mounting the compression fittings. Two duplex sensors with a diameter of 3 mm are introduced into each measuring chamber, screwed and sealed with conical NPT-F fittings. To prevent gas bubbles from accumulating in the measuring chamber, a venting is provided. The sensors are led through guiding tubes for stabilisation through the measuring chamber (see appendix Figure C.2). The thickness of the cover was calculated according to EN 13445-3:2021². The technical drawing of the temperature measurement chamber can be found in the appendix in Figure C.3.



Figure 3.5.: Temperature measuring chamber with compression fitting for Pt100 Sensors

As the temperature measurement significantly influences the overall measurement uncertainty, a computational fluid dynamics simulation (CFD) was carried out using Ansys 2022 R1 CFX with the following objectives.

- Is the measurement chamber influencing the temperature measurement negatively?
- Which immersion depth minimises environmental influences and ensures stable measurement conditions?

The simulation was performed at operating temperatures of 237°C for water and 430°C for HXLP. Free convection at the outside with $15 \text{ W}/\text{m}^2\text{K}$, an insulation with a thermal conductivity of 0.035 [W/(K m)] and an ambient temperature of 20°C was assumed. To investigate the effects of the immersion depth of the Pt100 sensors, three different immersion depths were simulated. An immersion depth of 150mm and thus 50 times the diameter is given for all due to the height of the pipe reductions up to the T-piece. In addition, the three different installation methods have a depth

¹Platinum resistor with an electrical resistance of 100 Ohm at 0°C

²DIN EN 13445-3:2021 Unfired pressure vessels - Part 3: Design

3. Design of the Measurement Bypass

from the centre of the T-piece of 20 mm, 65 mm and 100 mm. Figure 3.6 shows the flow velocity in the measuring chamber with clear differences, whereby the value in the head of the measuring chamber nearly reaches zero. At an immersion depth of 20mm, strongly varying velocities (blue and red lines close to the tip) and a partial reverse flow at the sensor tip become apparent. At deeper immersion depths, the sensor is in the direct flow path without the influence of the measuring chamber.

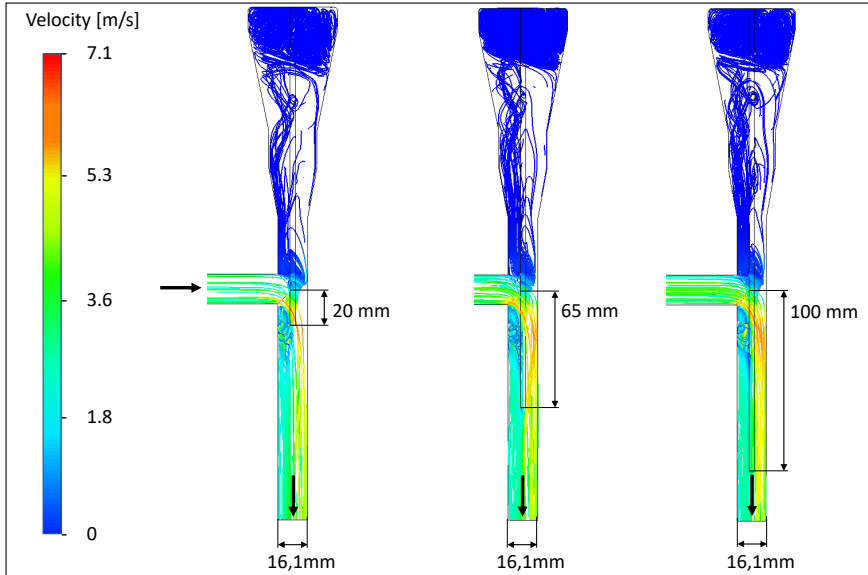


Figure 3.6.: Flow velocity in measurement chamber for different length of temperature sensor

For possible transient operating points, 65mm to 100mm provide direct and stable flow conditions. When looking at the temperature distribution, no difference in the temperature distribution in dependence can be seen with a steady flow. Appendix 3.7 shows an example of the temperature distribution with a sensor length of 100mm. In the head of the chamber, a maximum temperature difference of 1.42 Kelvin can be observed. Below the T-piece the temperature is equal to the input temperature. Overall, an immersion depth up to at least the middle of the T-piece must be ensured, so influences due to thermal losses in the head of the measuring chamber are significantly reduced.

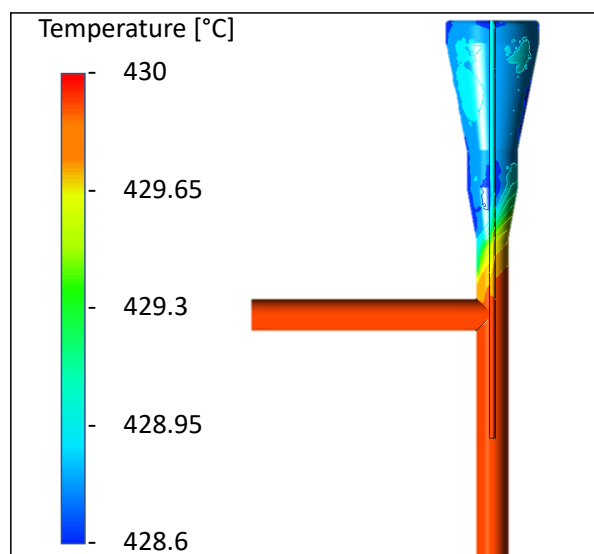


Figure 3.7.: Temperature profile in measurement chamber for HELISOL XLP with immersion depth of 100mm from center of T-piece

To simulate the temperature measurement chamber, a CAD model was generated. The measuring point is mirror-symmetrical and is therefore cut in the symmetry plane in order to save computing time by only meshing and calculating one half, as can be seen in Figure 3.8 on the left hand side. For the simulation, the model is divided into elements (Figure 3.8 top right), which form the basis for the numerical solved equation model. When meshing the model, a smaller element size and thus resolution of the component increases the accuracy of the later simulation, but the computational effort increases with an increasing number of elements. By means of a grid study for different element sizes, it was determined that with approx. 2.9 million elements for the temperature measurement chamber, a sufficiently accuracy is available. For the boundary condition at the pipe wall, the "no slip wall" was chosen, which means that the fluid has no velocity at the pipe wall. For an adequate mapping of the velocity profile in the boundary layer, an inflation layer with decreasing element diameter is used as can be seen in Figure 3.8 on the right bottom side. For a sufficiently large resolution at the boundary layer, a mean non dimensional wall distance value "y+" < 1 was chosen.

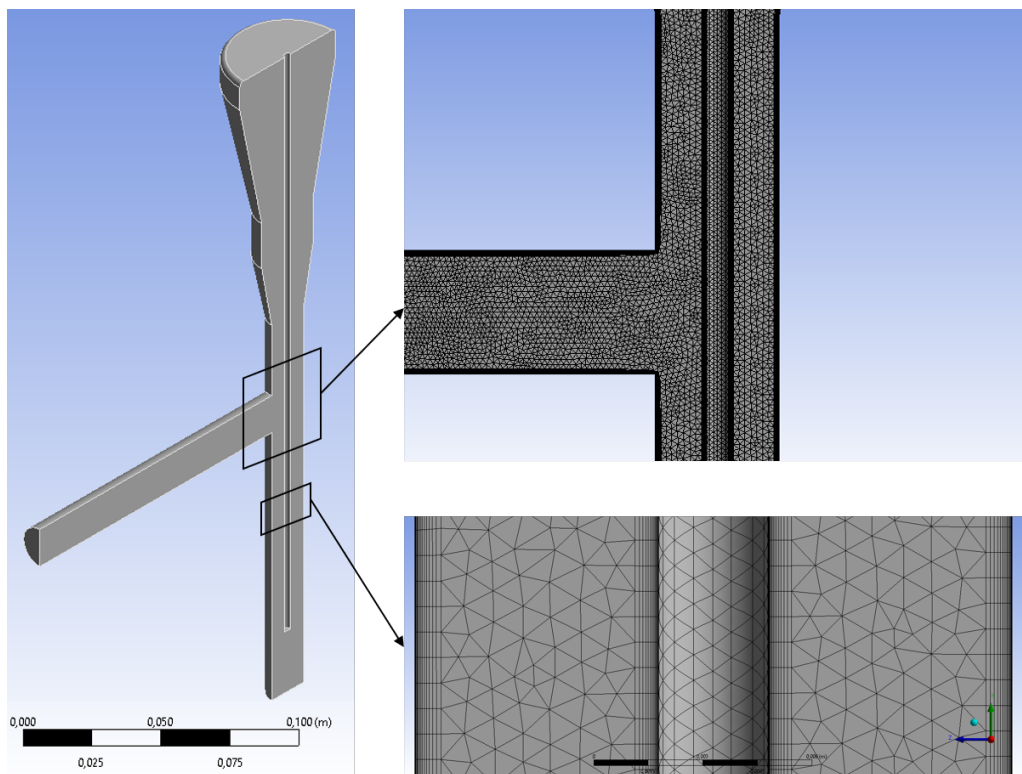


Figure 3.8.: Sliced geometry of temperature measuring chamber (left) with zoomed in mesh (top right) and inflation of element size on wall boundaries (bottom right)

With the temperature measurement chamber presented here, the surrounding influence can be significantly reduced in comparison to the previous approach with thermowell sensors located outside the connection flanges of the heat exchanger. Since flange joints have a larger surface area and are not insulated at the contact point, there is increased heat loss in this area. Measurements and simulations show an exponential increase in heat loss at different wind speeds, medium and ambient temperatures (Zheng et al., 2019). A diagram of the VDI heat atlas states a heat loss of approx. 600W and 250 W respectively for a pipe diameter of 30 mm at the expected operating conditions of HELISOL XLP (430°C) and water (250°C). To eliminate these thermal bridges and heat losses from the balance room, temperature sensors must be placed as close as possible to the inlets and outlets of the heat exchanger.

3.2.2. Massflow Measurement

A Coriolis sensor is used for mass flow measurement in the water circuit and in the HXLP circuit. In the water circuit, the Yokogawa Rotamass model is used with an uncertainty denoted by the manufacturer of 0.1% of the flow rate. The sensor is used in the cooling water circuit at a temperature of 60°C, which is within the manufacturer’s calibration range. The Rheonik Coriolis sensor in the HXLP circuit has been calibrated by the Research Institute of Sweden AB (RISE) for 20°C and 90°C. As the temperature rises, there is a shift in the mass flow reading for identical mass flows, which is why a temperature-dependent uncertainty was determined in previous measurements (Hilgert, Howar, et al., 2019, p. 9).

LDA Mass Flow Sensor Validation and Calibration

The uncertainty of the mass flow sensor in the silicone oil circuit has the most significant influence on the overall uncertainty of the flow calorimeter (Hilgert, Howar, et al., 2019, p. 10). In order to reduce this, the mass flow sensor will be calibrated in-situ by the National Metrology Institute of Germany (PTB) using Laser Doppler Anemometry (LDA). LDA is an optical velocity measurement method. Through an optical access (glass window), particles are illuminated by two crossed laser beams within the crosssection flow. The measurement volume is created in the crossing area (Juling, 2016, p. 3). Particles moving with the fluid through the measuring volume, generate a scattered light signal in a photo-detector, the frequency of which is proportional to the velocity component. Several measurements at different location in the crosssection can be used to determine the flow profile and the volume flow can then be calculated from the pipe cross-sectional area. The fluid density, which is known for HXLP from laboratory measurements, is used to obtain the mass flow.

In high-temperature in-situ calibrations with water in the power industry, a deviation of 0.12 % was achieved by LDA (Heitmann et al., 2020, p. 1). So far, no high-temperature in-situ calibrations with silicone oil have been carried out under field conditions. First preliminary investigations under lab conditions show a strong influence of the fluid quality on the scattering of the laser and thus the accuracy in the measurement volume. Figure 3.9 shows a test measurement with crossed laser beams in a clear HXLP sample taken at the PROMETEO facility (left). In comparison, a turbid HXLP sample with residues of a previous HTF from the KONTAS facility visualised potential inaccuracies (right) due to higher scattering. With a target of less than 1 % measurement uncertainty, a significant reduction in the overall uncertainty of the flow calorimeter can be achieved .

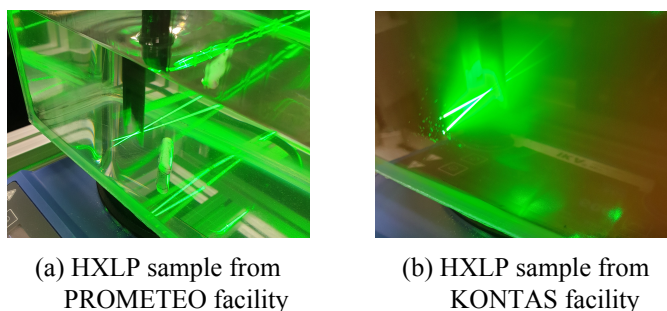


Figure 3.9.: HELISOL[®]XLP samples and the influence of fluid quality on the left side clear fluid and on the right side scattered turbid fluid with residues of a previous HTF

The in-situ LDA measurement will be connected at the 1” flange downstream the measurement heat exchanger (see Figure 3.1). The measurement chamber with a diameter of 2” is located in a straight line upstream the Coriolis sensor to be calibrated. A consistent flow profile is guaranteed by an inlet section of 10 times the pipe diameter and an outlet section of 5 pipe diameters see Appendix C.4.

3.2.3. Geometry of the Heat Exchanger

The geometry of the heat exchanger and therefore the area for heat transfer must be determined for accurate measurement. The following equations are relevant for the calculation of the area of the inner pipe:

$$A = \pi \cdot d \cdot L_{HE} \quad (3.5)$$

Precision pipes offer the lowest tolerance for standardised pipes. To stick to the original concept of the flow velocity and Reynolds number, the pipes with the diameters and tolerances shown in Table 3.2 are used according to DIN 10305-1 (DIN e.V., 2016, p. 14).

| Specified outside diameter with tolerances, d_a [mm] | Specified inside diameter with tolerances, d_i [mm] | Specified wall thickness [mm] |
|---|--|----------------------------------|
| 22 ±0.08 | 16.4 ±0.15 | 2.8 |
| 38 ±0.15 | 29 ±0.15 | 4.5 |

Table 3.2.: Dimensions and tolerances for precision pipes according to DIN 10305-1 (DIN e.V., 2016, p. 14)

Stainless steel 1.4571 from the group 316 steels is used for the double-tube heat exchanger. Its thermal conductivity is specified in the data sheets as 15 [W/mK] at 20°C. Various investigations such as (Ala-Outinen, 1996, p. 9) and (Frantz et al., 2022, p. 8) have given a temperature dependence of the thermal conductivity as follows:

$$\lambda_{316}(T) = (1.27551 \cdot 10^2 \cdot T / (\text{degC}) + 14.7449) \frac{\text{W}}{\text{m K}} \quad (3.6)$$

For a given diameter, the length of the heat exchanger is decisive for the transferred heat and thus the respective temperature differences from the inlet to the outlet of the silicone oil and the cooling water. Water has a higher heat capacity than silicone oil, therefore water will experience a smaller change in temperature than HXLP. As already observed in previous experiments, the uncertainty of the temperature difference measurement is 0.1 K (Hilgert, Howar, et al., 2019, p. 9). It was decided to aim for temperature changes of $\Delta T_{\text{water}} = 14 \text{ K}$ and $\Delta T_{\text{HXLP}} = -30 \text{ K}$, which can be achieved with a total heat transfer length of 2000 mm. Hence the complete heat transfer device is divided into four double pipe heat exchanger, contrary to the initial design of two double pipes with 4 m length each.

By a repeated measurement of the geometry, the uncertainty of the heat-transmitted surface can be further reduced. The tolerance of a manual micrometer is approx. ±0.004 mm (Thomas Bornath, 2020, p. 21). Measurements with low uncertainty can be achieved with several measuring points distributed along the length of the pipe. In addition, the wall thickness should be checked with wall thickness measurement devices, as soon as the measurement heat exchanger is manufactured. The length can be measured with a line scale, for a length of 2000mm a tolerance of ±0.15mm is given (Thomas Bornath, 2020, p. 20). As heat-transferring pipes expand with increasing temperature, the thermal expansion coefficient is considered for calculating the area.

$$L_{HE} = L_0 * (\alpha_{thexp} * \Delta T + 1) \quad (3.7)$$

$$d = d_0 * (\alpha_{thexp} * \Delta T + 1) \quad (3.8)$$

Due to the fact that the average wall temperatures of the inner and outer pipes are different, the pipes expand differently during the heating process and when the operating point changes. To avoid stresses in the heat exchanger, the difference in length must be compensated, which will be explained in the following section.

3.2.4. Stuffing Box for Length Expansion Compensation

For compensating the thermal induced expansion, an individual designed stuffing box is used to minimise the unavoidable influences of the axial compensator. The function of a stuffing box is based on the compression of gland rings, which provides a seal between the housing and a tube or shaft, but allows the components to move relative to each other. The stuffing box consists of the main pipe, which is welded to the outer tube of the heat exchanger, as can be seen in Figure 3.10. In the stuffing box there are 6 graphite packing rings and two stiffer rings at the corresponding ends, which are pressed together with the adjusting nut. For a tight connection, the nut should be tightened to a torque of 30 Nm, as recommended for comparable stuffing boxes for valves (Emerson, 2021, p. 10). In order for the inner pipe to move, the surface at the sealing area must have $Ra \leq 1\mu m$.³ The stuffing box was designed for the prevailing pressure and manufactured using CNC machines (technical drawing see appendix C.5 and C.6). A pressure test at 120 bar proved the tightness.

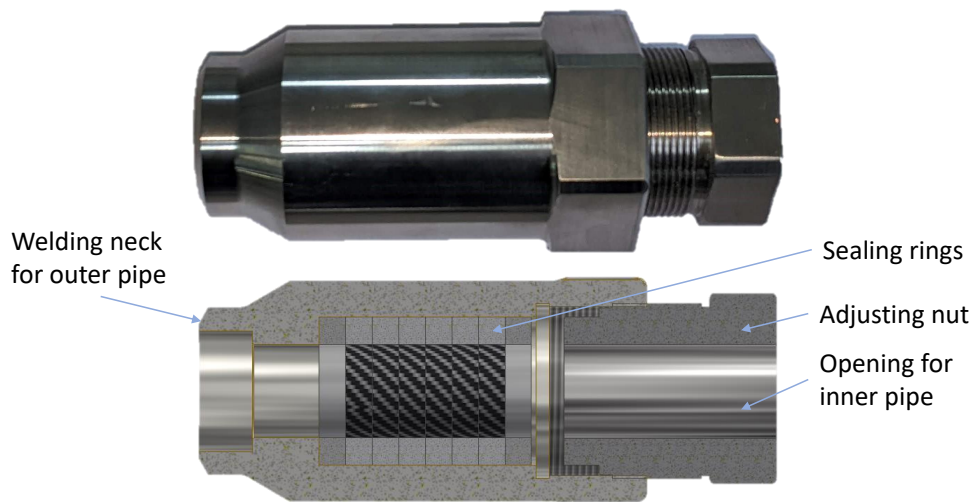


Figure 3.10.: Stuffing box for sealing the inner pipe to the outer pipe and allowing relative motion in axial direction

The tailored stuffing box offers advantages compared to a standardised bellow axial compensator due to its reduced surface, and therefore heat losses. Suitable bellow axial compensators for the operating conditions of 80 bar have a three times larger diameter than the stuffing box. Furthermore unacceptable forces in the longitudinal direction occur, due to the prevailing pressure.

3.2.5. Heat Losses

The unavoidable heat losses are caused by the heat transfer from the outer pipe through the thermal insulation to the environment. The heat losses should be minimised for two several reasons: For reducing the measurement uncertainties, enabling steady state condition and safety. Due to variable environmental parameters that change during the measurement period, such as temperature and wind, potential uncertainties can affect the system. Although heat losses can be measured in different environmental conditions, fluctuations will affect and increase the uncertainty of the measurement. Another reason is the applicability of the formulas for calculating the heat transfer coefficient α_{water} in the annular gap. For the considered calculation case an insulated surface on the outer pipe is assumed.

The relevant heat losses at the heat exchanger occur in the energy balance volume. The heat losses across the outer pipe depend on the convective (influence of the wind) and conductive heat losses. In Figure 3.11, the heat losses are plotted against the insulation thickness at different wind

³Ra is a measure of the roughness of a technical surface, determined by the peaks and depths over a certain area.

speeds at an ambient temperature of 20 °C. As insulation thickness increases, thermal conduction dominates the heat flux. According to DIN 4140 for insulation work on industrial installations, a minimum insulation thickness of 70 mm must be ensured for a given pipe diameter of 38 mm and a temperature of 250 °C (DIN, 2022, p. 46). The constructional conditions of the system limit the thickness of the insulation. With an insulation of 90 mm, the total heat loss Q_{loss} is reduced to approx. 62 W. In Equation 3.9, the heat loss is calculated according Equation 2.17 and 2.18. An initial convective heat transfer of $\alpha_{water} = 16112 W/m^2K$, an ambient convection of $15 W/m^2K$, an average water temperature of 243 °C and ambient temperature of 20 °C are applied.

$$Q_{loss} = \frac{\pi \cdot 2m \cdot (243^{\circ}C - 20^{\circ}C)}{\frac{1}{16112 W/m^2K \cdot 0.038m} + \frac{1}{2 \cdot 0.035 W/mK} \cdot \ln \frac{178mm}{38mm} + \frac{1}{15 W/m^2K \cdot 0.178m}} = 62.45W \quad (3.9)$$

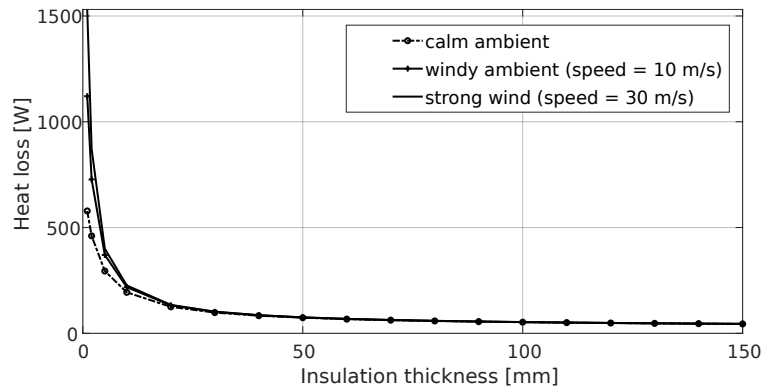


Figure 3.11.: Heat loss of 2000 mm pipe section of the heat exchanger through insulation for different wind speeds at 20°C ambient temperature

The initial design also includes pipe supports on the heat exchanger. Heat loss studies show that on an average up to 400W is lost per pipe shoe (Kerkwijk, 2016, p. 46), due to conduction. To avoid these thermal bridges and punctual changes in wall temperature, which affect the measurement, the pipe supports are placed outside the energy balance volume or on the insulation.

The heat loss by radiation from the outer jacket of the insulation, which is blank aluminium, to the environment is calculated by using Equation 3.10 (see Chapter 2 Equation 2.15). For blank aluminium sheet, which serves as the outer layer of the insulation, an emissivity of 0.05 is specified (VDI, 2013, p. 1087). With an outer diameter of the insulation of 0.178m and a temperature at the outer layer of 30°C, radiation losses to ambient temperature (20°C) are only 3 W, which is negligible compared to the transferred heat of 16 500 W.

$$Q_{rad} = \epsilon A \sigma (T_p^4 - T_{amb}^4) \quad (3.10)$$

$$Q_{rad} = 0.05 \cdot \pi \cdot 0.178m \cdot 2m \cdot 5.669 \cdot 10^{-8} \frac{W}{m^2K^4} \cdot (303.15K^4 - 293.15K^4) = 3.36W \quad (3.11)$$

By locating the temperature measurement close to the heat exchanger without flange connections in between, by avoiding the pipe support in the energy balance room and the insulation, the heat losses can be effectively minimised to approx. 60 W with reduced influence of surrounding. The measurement of heat losses is presented in the evaluation in Chapter 4.3.2. For a measurement of the pipe wall temperature and thus confirming the above presented assumptions during measurements, four temperature sensors are installed around the circumference on the hot side of the heat exchanger, in the middle and on the cold side.

4. Measurements and Evaluation

During this thesis, the PROMETEO loop was not operational due to a pump failure and the resulting reconstruction activities, hence no measurements on HXLP could be carried out in the flow calorimeter.

4.1. Validation of the Flow Calorimeter with Water

For the validation of the flow calorimeter after the reconstruction and for the identification of potential uncertainties, the flow calorimeter is operated with water. The physical properties of water are denoted with a low uncertainty and is ideal for initial comparative measurements due to its simple handling. Analog to previous water test measurements with the flow calorimeter (Howar, 2016, p. 26) a pump circulates water from a tank and filter through the measurement set-up and returns it to the tank.

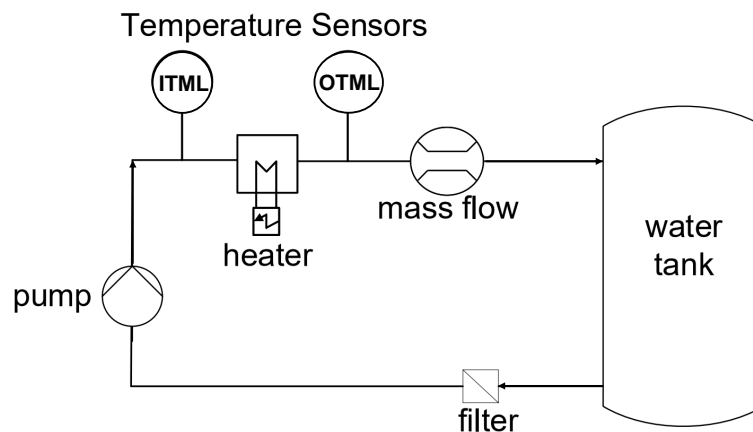


Figure 4.1.: Flow calorimeter setup with water for validation measurements

Results of the measurements show that the heat capacity can be measured with a low uncertainty and repeatably. At a mean water temperature of 32 °C, a heat capacity of 4181 J/kg,K was measured with an uncertainty of 1.5 %, deviating by 0.05 % from the IAPWS reference value of 4179 J/kg K with a given uncertainty of 0.3 %. The existing evaluation routine in Matlab first performs the absolute and relative calibration. The flow velocity is used to determine the residence time in the flow calorimeter, which corresponds to the time it takes for a particle to travel from the inlet temperature measurement location (ITML) to the outlet temperature measurement location (OTML). For this purpose, the residence time is subtracted from the temperature vector of the initial temperature. The heat capacity is calculated using the formula presented in Chapter 2.5.

Figure 4.2 shows the data set of a validation measurement with water. The linear ramp due to the heating of the water tank is taken into account in the calculation. The influences of the grid stability on the heating power (pink line) can be clearly seen. Since the fluctuations are relatively small (few watt), a result with low uncertainties can nevertheless be achieved by observing a longer period of several minutes. The attempt to stabilise the heating power by means of a control system is also not possible, as the heating controller can only be controlled in the integer percentage range

4. Measurements and Evaluation

and thus the smallest step size is 100 W. To minimize the grid instabilities an uninterrupted power supply (UPS) can provide a stable supply, however, is not available at the PROMETEO facility.

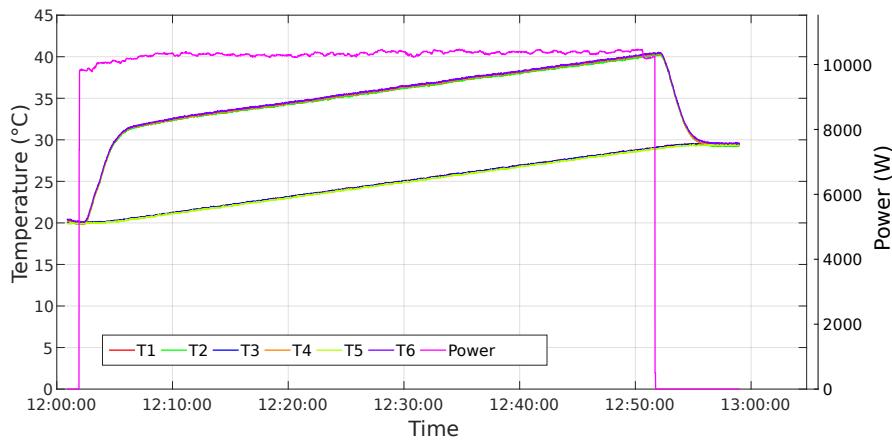


Figure 4.2.: Measurement of flow calorimeter with water for system validation

Absolute calibration

Each temperature sensor has an individual temperature response, for this reason the Pt100 sensors (named T1 through T6) are first calibrated absolutely in a mobile calibrator with a reference to determine the temperature-dependent deviation. The deviations shown in Figure 4.3 can be adjusted with a correction function. The calibration procedure was performed in previous measurements with the flow calorimeter (Howar, 2016, p. 22) and stated a uncertainty of 0.1 K of the temperature measurement, including the relative calibration described in the next section.

The Ametek RTC 700 B reference temperature calibrator is used for the absolute calibration and consists of a temperature controlled electrical heater, a multiple test sensor data acquisition system, a reference sensor and a DLC (Dynamic Load Compensation) sensor. The sensors are inserted into a metal cylinder with high thermal conductivity. The DLC sensor measures the axial temperature distribution along the cylinder and can compensate for axial temperature inhomogeneities. During automatic calibration, a program from 25 °C to 475 °C is ran in increments of 25 K, with a temperature stability of 0.015 °C.

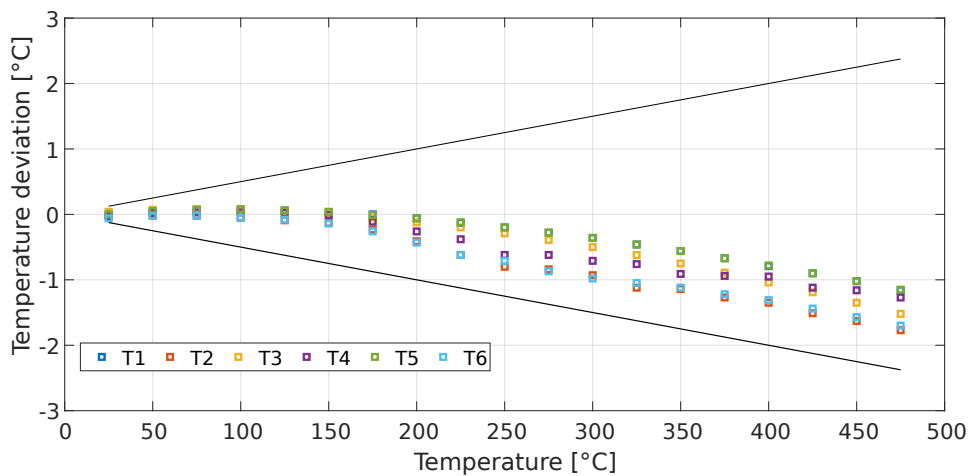


Figure 4.3.: Deviations of the Pt100 temperature readings over the absolute temperature to the reference in the AMETEK calibrator with the tolerance limits (black lines) of 0.5 % rng.

Relative calibration

The differential temperature has the largest budget in the overall uncertainty. For this purpose, a relative calibration including the entire measurement sequence is done with the temperature sensors and the data acquisition of the flow calorimeter as can be seen in Figure 4.4.

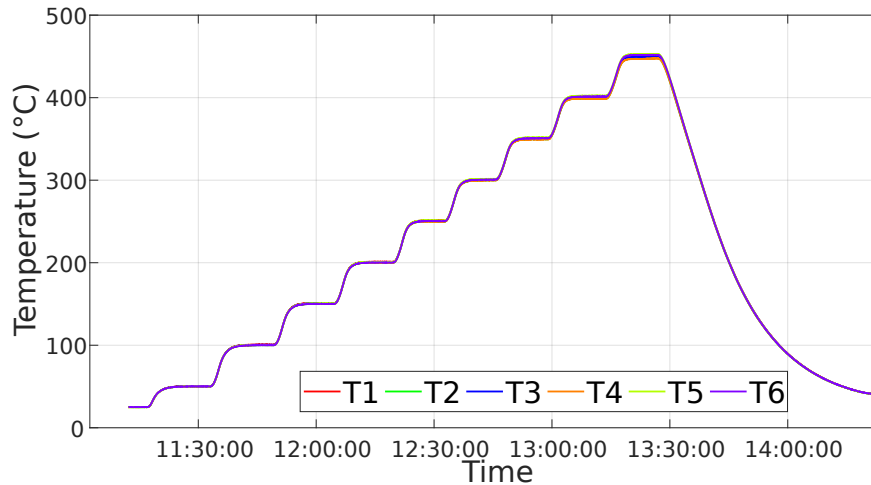


Figure 4.4.: Relative calibration in AMTETEK caloribrator indicating larger deviations at higher temperatures in a range from 25 °C to 475 °C

The data set (see Figure 4.4) shows that the deviations and combined uncertainty of the sensors and the DAQ increase with rising temperature. Figure 4.5 shows on the left hand side the raw data at 400°C with a considerable offset in temperature readings. On the right hand side the absolute and relative calibrated data is presented after an adjustment by a correction function. This allows the temperature to be measured stably within a reduction in uncertainty below 0.1 K.

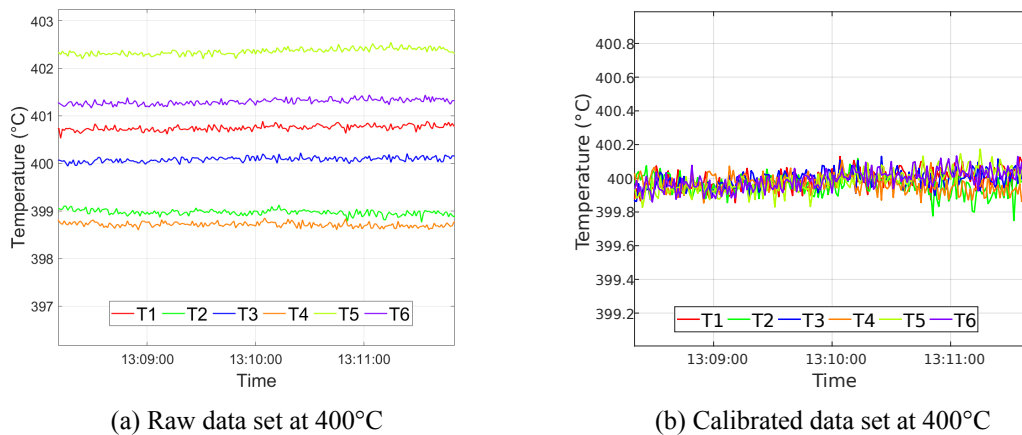


Figure 4.5.: Raw data set (left side) and data set after relative and absolute calibration (right side) of Pt100 temperature reading

4.2. Generation of Dummy Data for the Measurement Heat Exchanger

Since the construction and delivery of the heat exchanger system require more time than planned, no measurements with the heat exchanger were carried out and presented in this thesis. Thus to automate the evaluation of the heat exchanger’s measurement data, dummy data was generated. Based on operating data of the PROMETEO parabolic trough system (see Figure 4.6) the data set was extended to the sensors of the heat exchanger system.

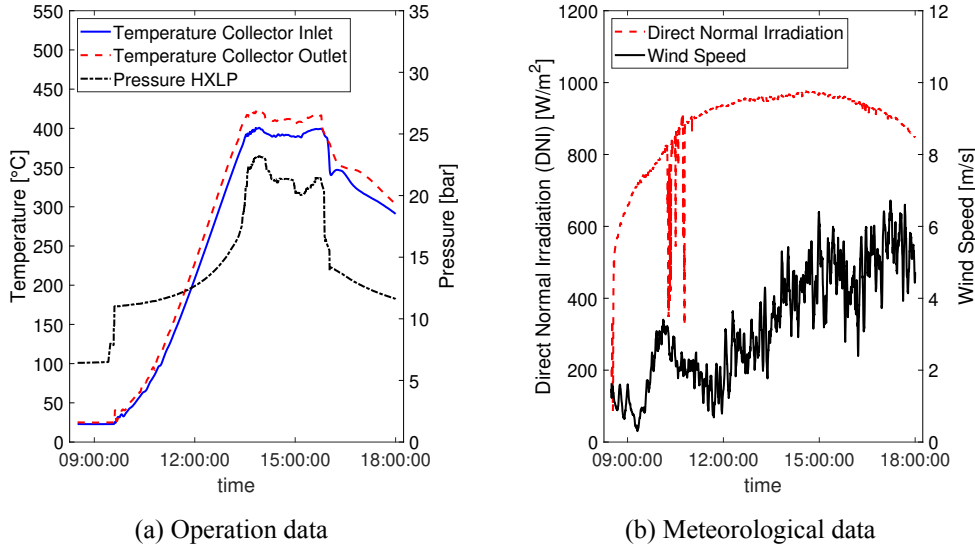


Figure 4.6.: Exemplary measurement data of PROMETEO facility from September 2022

Accordingly to the sensor list, see Table 4.1, data was created with the sake to develop and run the data evaluation software. A total of 32 sensor signals are relevant for the evaluation and calculation of the specific heat transfer coefficient and the specific heat capacity. With all these derived values of the PROMETEO operations data, the evaluation of the data can be automatised. Matlab is used and an existing environment for reading and filtering data for thermal measurements on the PSA.

| Sensor name in PID | Unit | Measurement location |
|--------------------|------|---|
| TT 10151 - (1/2) | °C | Outlet HXLP heat exchanger (duplex) |
| TT 10152 - (1/2) | °C | Outlet HXLP heat exchanger (duplex) |
| TT 10153 - (1/2) | °C | Inlet HXLP heat exchanger (duplex) |
| TT 10154 - (1/2) | °C | Inlet HXLP heat exchanger (duplex) |
| TT 51151 - (1/2) | °C | Outlet water heat exchanger (duplex) |
| TT 51152 - (1/2) | °C | Outlet water heat exchanger (duplex) |
| TT 51153 - (1/2) | °C | Inlet water heat exchanger (duplex) |
| TT 51154 - (1/2) | °C | Inlet water heat exchanger (duplex) |
| TT 51105 - 51108 | °C | Surface hot side (4 sensors) |
| TT 51109 - 51112 | °C | Surface middle (4 sensors) |
| TT 51113 - 51116 | °C | Surface cold side (4 sensors) |
| FIT 51701 | kg/s | Massflow water |
| Additional sensor | kg/s | Massflow HXLP (DAQ of flow calorimeter) |
| Additional sensor | °C | Insulation middle |
| Additional sensor | °C | Ambient |

Table 4.1.: Integrated sensors for heat exchanger with sensor names of PID

4.2. Generation of Dummy Data for the Measurement Heat Exchanger

The operating data was adjusted as follows to obtain appropriate demo data. In a first step, the sample rate of the measurement data of the PROMETEO facility with an interval of 10s is increased by means of linear interpolation to 1s. The higher sampling rate of 1s provides more information about the process and enables better statistical evaluation. Based on the temperature of the collector output, four temperature signals were created as input to the heat exchanger with an offset. The offset represents the systematic deviation due to the data acquisition, which is later on eliminated by a relative calibration. The water temperature follows the collector temperature during heating up to 235°C see Figure 4.7. After that, the temperature is kept constant, as it is done in the heat exchanger by means of controlling the cooler and electric heater to have a constant input temperature on the water side. There are a total of four temperature signals for the water inlet, also with a respective offset.

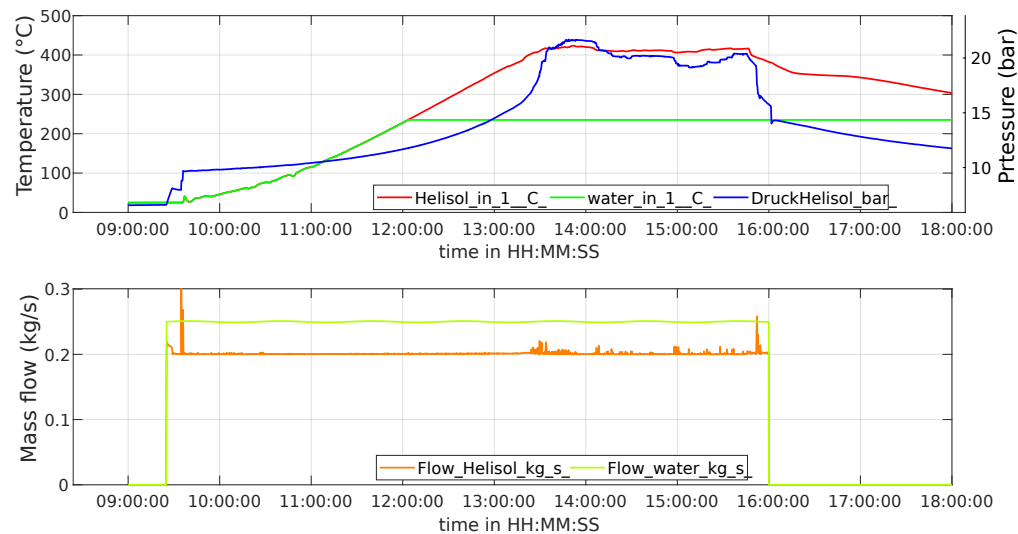


Figure 4.7.: Overview chart of selected operating data of the demo data of the PROMETEO system, top: inlet temperatures and pressure of HXLP, below: mass flows HXLP and water

According to initial heat transfer calculations, the output temperatures from the heat exchanger were calculated with the formulas presented in Chapter 2.7 for four sensors each for HXLP and water. The values from Table 4.2 were used for the calculation of the outlet temperatures.

| | | |
|---|--------|----------------|
| Specific heat capacity water (100 bar /225 °C) | 4585 | J/kg K |
| Specific heat capacity HXLP (15 bar / 362.5 °C) | 2300 | J/kg K |
| Heat transmission k | 768 | W/mK |
| Heat transfer surface A | 0.1338 | m ² |
| Massflow HXLP | 0.2 | kg/s |
| Massflow water | 0.25 | kg/s |
| Fouling factor FN | 1 | - |

Table 4.2.: Initial values for the generation of demo data

In the measurement heat exchanger, surface sensors are distributed around the circumference to measure the temperature (see Figure 4.8), which allows to measure the heat loss and the temperature distribution in the outer pipe. The surface temperatures for the demo data were calculated based on the fluid temperature and the heat transfer through the outer pipe and the insulation to the environment. The surface temperatures are measured on the hot side (TT51105-08), in the middle (TT51109-12) and on the cold side (TT51113-16) of the heat exchanger.

4. Measurements and Evaluation

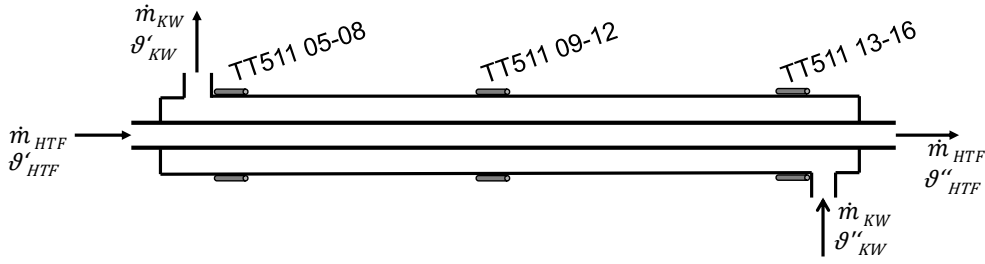


Figure 4.8.: Simplified scheme for the arrangement of the circumferential temperature sensors on the outer pipe surface

Based on the fluid temperature ϑ_{water} , Equation 4.1 is used to calculate the temperatures at the surface of the pipe towards the insulation.

$$\vartheta_{bl} = \vartheta_{amb} + k_R \left(\frac{1}{\Lambda_{R,bl}} + \frac{1}{\pi D_a \alpha_a} \right) (\vartheta_{water} - \vartheta_{amb}) \quad (4.1)$$

- ϑ_{bl} – Temperature boundary layer [$^{\circ}\text{C}$]
- ϑ_{amb} – Temperature ambient [$^{\circ}\text{C}$]
- ϑ_{water} – Temperature water [$^{\circ}\text{C}$]
- k_R – Heat transmission coefficient (pipe to ambient) [W/mK]
- $\Lambda_{R,bl}$ – Heat transfer resistance insulation [mK/W]
- α_a – Heat transfer coefficient (fluid to outer pipe) [$\text{W}/\text{m}^2\text{K}$]

The following equation is used to calculate the heat transfer resistance of the pipe and the surrounding insulation:

$$\frac{1}{\Lambda_{R,bl}} = \frac{1}{2\pi} \left(\frac{1}{\lambda_{steel}} \ln \frac{D_a}{D_i} + \frac{1}{\lambda_{steel}} \ln \frac{D_a + 2s_{insu}}{D_a} \right) \quad (4.2)$$

The input values for the thermal conductivity of the metal pipe and the insulation, as well as the thickness of the insulation, can be found in Table 4.3. To calculate k_R , formula 2.18 is used.

| | | |
|--|-------|-------|
| Thermal conductivity of insulation λ_{insu} | 0.035 | W/m K |
| Thermal conductivity of 1.4571 steel λ_{steel} | 15 | W/m K |
| Insulation thickness s_{insu} | 90 | mm |

Table 4.3.: Input values for the calculations of radial temperatures along the heat exchanger

Transferable with the calculation of the surface temperature of the pipe, the temperature in the insulation was calculated at half the radius (45mm). This allows the heat flow through the insulation to be quantified and determined more accurately, because there is only heat conduction.

In the last step of the preparation of the demo data, the fluid temperature of HXL P at the mass flow sensor was determined based on the cooling capacity of the heat exchanger. The temperature is used for the calculation of the measurement uncertainty, as the uncertainty of the Coriolis sensor correlates with increasing temperature.

4.3. Data Evaluation for the Measurement Heat Exchanger

For the automated measurement data evaluation for steady-state processes, demo data was generated which match the expected data from the heat exchanger and serve as a valid basis for the calculation of the heat capacity and the specific heat transfer coefficient. For the evaluation, individual suitable stationary measurement points are first selected from the entire data set and then automatically evaluated. The first step is the absolute calibration of the temperature sensors, which can be determined using the mobile Ametek calibrator. This is followed by the relative calibration of the sensors, identical to the relative calibration presented in Chapter 4.1. For the calibration of the Coriolis mass flow sensor, the results of the external Laboratory RISE are used. As soon as the calibration results of the LDA volume flow calibration are available, they can be implemented. As the residence time is necessary for the evaluation of the heat capacity in the flow calorimeter, it is also calculated for the heat exchanger in the inner tube as well as in the annular gap. The residence time indicates how long it takes a defined volume of liquid or particles to pass through the apparatus and is calculated according to Equation 4.3.

$$t_{res} = \frac{\rho V}{\dot{m}} \quad (4.3)$$

This allows constant temperature shifts between the input temperature measurement and the output to be taken into account in transient conditions. The residence time for HXLP in the inner tube is 0.98 seconds for the intended operating conditions and 1.8 seconds for water. Since no change can be detected in these short residence times due to the thermal inertia of the heat exchanger, and the operation data of the PROMETEO facility does not change significantly in these intervals, no relevance is assigned to the residence time.

4.3.1. Energy Balance in the Heat Exchanger

The stationary energy balance in the heat exchanger is fundamental for calculating the heat capacity. The heat transferred by the HXLP from the inner pipe is equal to the heat absorbed by the water in the annular gap added by the heat losses through the surface of the outer pipe as can be seen in Equation 4.4.

$$-Q_{HXLP} = Q_W + Q_{loss} \quad (4.4)$$

The absorbed heat of the water is determined by the temperature difference between inlet and outlet, the mass flow and the specific heat capacity. The specific heat capacity of water is extracted for the operating points from the International Association for the Properties of water and steam (IAPWS). In the range considered for liquid water, an uncertainty of 0.3% is stated for the specific heat capacity (IAPWS, 2007, p. 47).

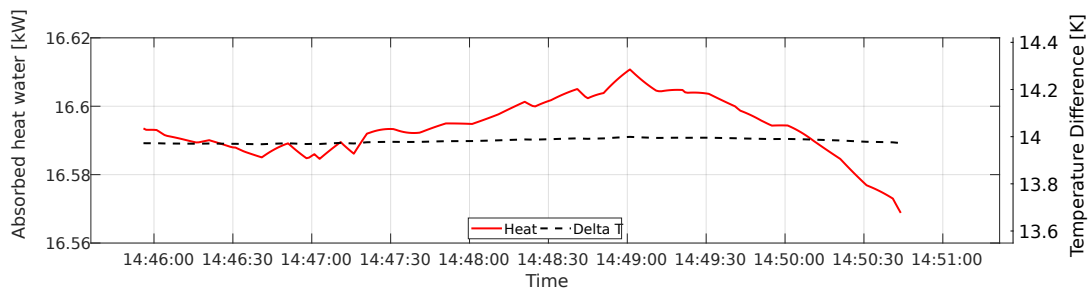


Figure 4.9.: Absorbed heat of water in the measurement heat exchanger and mean temperature difference between inlet and outlet in a measurement point over 5 minutes

4.3.2. Heat Losses in the Heat Exchanger

Even if the heat exchanger is provided with sufficient insulation and pipe supports and flanges in the measurement section are removed, heat loss to the environment cannot be eliminated. The aim is to subsequently compensate the heat loss in the evaluation. With an insulation of 90mm, a heat loss of 60 watts prevails which is marginal compared to the transferred heat of 16.500 W. Nevertheless, compensating for the losses reduces the overall measurement uncertainty. To quantify the heat losses, three methods are specified and implemented in the evaluation code.

Method water to ambient uses the mean fluid temperature of water and the ambient temperature.

By knowing the specific heat transfer coefficient of water α_{water} in the annular gap and air at the ambient α_{amb} in combination with the thermal conductivity of the steel pipe λ_{steel} and insulation λ_{insu} (Table 4.3) Equation 2.17 and 2.18 lead to the following Equation 4.5 to determine the heat loss.

$$Q_{loss} = \frac{\pi L_{HE} \cdot (\vartheta_{water} - \vartheta_{amb})}{\frac{1}{\alpha_{water} D_i} + \frac{1}{2 \lambda_{steel}} \ln \frac{D_a}{D_i} + \frac{1}{2 \lambda_{insu}} \ln \frac{D_a + 2 s_{insu}}{D_a} + \frac{1}{\alpha_{amb} (D_a + 2 s_{insu})}} \quad (4.5)$$

When applying this method, a wind-dependent heat transfer coefficient alpha must be assumed. For soft wind $\alpha_{amb} = 15 \text{ W/m}^2\text{K}$ can be selected, depending on the wind speed up to $\alpha_{amb} = 150 \text{ W/m}^2\text{K}$ (VDI, 2013, p. 723). Since the wind speed at the heat exchanger is reduced by surrounding pipes and equipment, the convective heat transfer to the air is denoted with a higher uncertainty. In total, convective heat transfer is insignificant; heat conduction dominates. To reduce the uncertainty of the heat loss the following method is applied.

Method surface sensors into insulation can be used to consider only heat conduction in the insulation. For this, the averaged temperature of the surface sensors placed in the middle of the heat exchanger is used, as well as the temperature sensor in the middle of the insulation. Thus, the Equation 4.5 is simplified to Equation 4.6. In addition to the measurement through the insulation, the heat loss can be determined by the next method.

$$Q_{loss} = \frac{\lambda_{insu} 2 \pi L_{HE} \cdot (\vartheta_{(s-mid)} - \vartheta_{insu})}{\ln \frac{D_a + s_{insu}}{D_a}} \quad (4.6)$$

Measuring the heatloss at an operating point without heat transfer between HXLP and water. The cooling of the water in the outer pipe is then caused by the heat losses to the surrounding and can be measured by the temperature difference between inlet and outlet. However, the heat losses are very small. With the previously presented methods and an insulation of 90mm, a heat loss of 60 watts can be expected. If the formula 2.5 from Chapter 2.5 is used for the correlation of the transferred heat, it shows that a very low mass flow must be set in order to measure a differential temperature of 1 Kelvin at the intended operating point:

$$\dot{m} = \frac{\dot{Q}_{loss}}{c_p (T_2 - T_1)} = \frac{-60\text{W}}{4.76 \frac{\text{kJ}}{\text{kgK}} (-1\text{K})} = 0.0126 \frac{\text{kg}}{\text{s}} \quad (4.7)$$

At low differential temperatures, the uncertainty increases due to the measurement instrumentation. The convective heat transfer is also reduced at low flow velocities, therefore the result is subject to high uncertainty.

4.3.3. Specific Heat Capacity and Heat Transfer Coefficient in Heat Exchanger

Specific Heatcapacity

Formula 4.8 is used to calculate the heat capacity. In the automatic evaluation, the specific heat capacity calculated from the measurement data is compared with the data sheet from the manufacturer WACKER for HXLP and laboratory values with a differential scanning calorimeter from DLR.

$$c_p = \frac{\dot{m}_{water} c_{p,water} \Delta T_{water} - \dot{Q}_{loss}}{\dot{m} \Delta T_{HXLP}} \quad (4.8)$$

Specific Heat Transfer Coefficient

The calculation of the heat transfer coefficient of HXLP is carried out in several steps. In the first step, the literature values are calculated according to the VDI Heat Atlas, in Chapter 2.8.1 and for the annular gap in Chapter 2.8.2. The thermophysical properties are taken from the data sheet. The Nusselt number is corrected in the VDI procedure with a factor for the fluid properties at wall temperature. The calculation of the wall temperature, the Nusselt numbers and thus the literature values for the specific heat transfer coefficients is carried out iterative as shown in Figure 4.10. First, the Nusselt number is calculated for the mean fluid temperature. This is followed by the calculation of the wall temperature, in the first run with an initial value for the heat transfer. After calculating the correction factor with the Prandtl numbers for fluid and wall temperature, the heat transfer coefficient can be calculated. Since the heat transfer coefficients influence the wall temperatures in the inner pipe and outer pipe, a residual value to the previous run, or initial value, is determined. The heat transfer loop is repeated until the set residual value to the previous iteration is met.

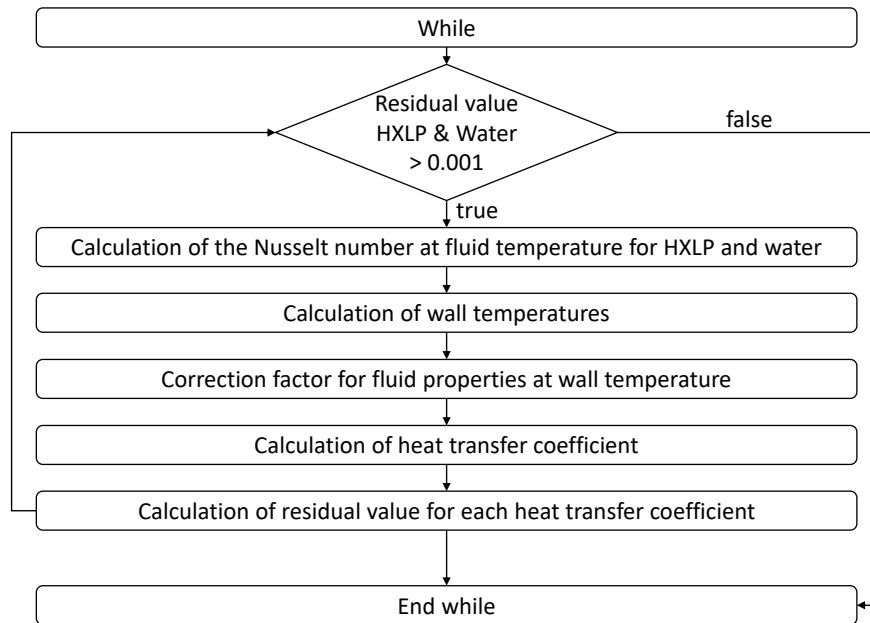


Figure 4.10.: Program flow for iterative calculation of specific heat transfer coefficient

The calculation of α_{HXLP} using Equation 4.9 is based on the knowledge of the heat transfer from the pipe to the water which is taken from literature.

$$\frac{1}{\alpha_{HXLP}} = \frac{d_i}{d_a} \left(\frac{1}{k} - \frac{d_a \ln \frac{d_a}{d_i}}{2 \lambda_{steel}} - \frac{1}{\alpha_{water}} \right) \quad (4.9)$$

4. Measurements and Evaluation

The heat transmission coefficient k is calculated by means of the measured transferred heat \dot{Q}_{HXLP} , the logarithmic temperature difference $\Delta\vartheta_{ln}$ and the heat transfer area A_2 ¹. The following Equation 4.10 applies:

$$k = \frac{\dot{Q}_{HXLP}}{A_2 \Delta\vartheta_{ln}} \quad (4.10)$$

After the specific heat transfer coefficient of HXLP has been determined, the measured value is compared with the literature value according to the calculation procedure in Chapter 2.8.1. Figure 4.11 shows the typical control figure for counterflow heat exchangers. The temperature over the length of the heat exchanger is calculated from the measurement data and shows the relationship between the heat capacity flows and the temperatures that result.

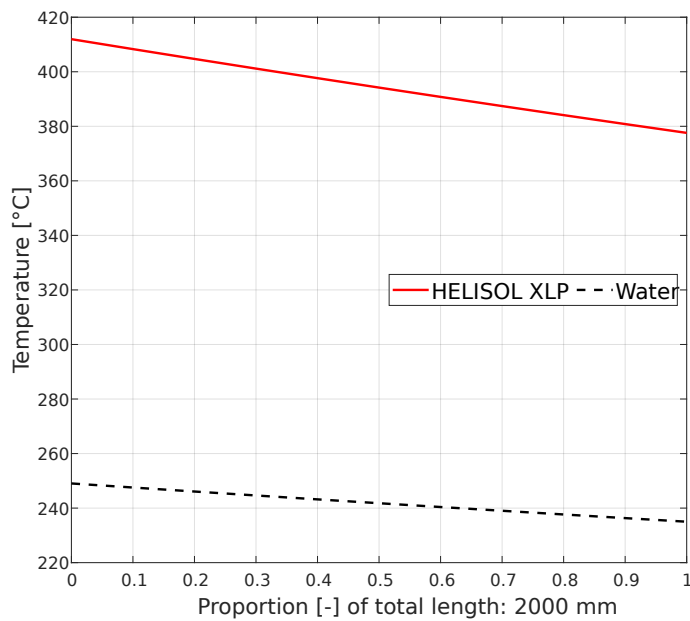


Figure 4.11.: Temperature profile of HXLP and water in heat exchanger over the proportion of the total length of 2000 mm

¹The heat transfer surface is referred to the outer surface of the pipes for standardisation (VDI, 2013, p. 49)

5. Measurement Uncertainties

The uncertainty analysis analyses the statistical and systematic uncertainty of the measurand. The calculation follows the "Guide to the expression of uncertainty in measurement" by the Joint Committee for Guides in Metrology (BIPM, 2008). The uncertainty of the flow calorimeter and the heat exchanger depends on the operating points such as temperature and flow, but also on the system configuration, whether the flow calorimeter is operated with or without the heat exchanger and whether the LDA inline calibration is included. This results in different cases, which are considered separately below.

5.1. Measurement Uncertainty of Specific Heat Capacity

The specific heat capacity can be measured either in the flow calorimeter or in the heat exchanger. For the flow calorimeter there are three operating options, either in the original state up to 350 °C with the heat exchanger and with the LDA mass flow calibration. These will be presented individually in the following.

The uncertainty analysis according to GUM in Chapter 2.9 consists of the type A uncertainties, which can be determined by the mean value and the standard deviation of the measured values. The type B uncertainties are derived from the manufacturer's specifications of the measuring instruments. In Table 5.1 the relevant type B uncertainties for the calculation of the overall measurement uncertainty for the specific heat capacity are noted.

| Measurand | Symbol | Uncertainty (u_{TypeB}) |
|----------------------------|-------------------|---|
| Temperature difference | ΔT | 0.1 K |
| Electrical Power | P_{el} | 0.1 % reading + 0.1 % range |
| Heat loss flow calorimeter | $Q_{loss,fc}$ | 40 W |
| Heat loss heat exchanger | $Q_{loss,he}$ | 10 W |
| Mass flow HXLP | \dot{m}_{HXLP} | 0.6 % reading + 0.0032%/°C ¹ |
| Mass flow water | \dot{m}_{water} | 0.1 % |
| heat capacity water | cp_{water} | 0.3 % |

Table 5.1.: Type B uncertainties for calculating the overall measurement uncertainty for the specific heat capacity of HXLP

CP1 - flow calorimeter without heat exchanger for temperatures up to 350°C

For the initial flow calorimeter, an uncertainty analysis was carried out (Howar, 2016, p. 40) corresponding to operation without heat exchanger up to 350°C. Using the Formula 5.1 for calculating the heat capacity the combined uncertainty is calculated.

$$c_p = \frac{P_{el} - \dot{Q}_{loss,fc}}{\dot{m}_{HXLP} \Delta T_{HXLP}} \quad (5.1)$$

For the calculation of the type B uncertainty, the partial derivative is formed, resulting in the sensitivity coefficients c_i .

$$\begin{aligned}
 c_1 &= \frac{\partial c_p}{\partial P_{el}} = \frac{\partial c_p}{\partial \dot{Q}_{loss,fc}} = \frac{1}{\dot{m}_{HXLP} \Delta T_{HXLP}} \\
 c_2 &= \frac{\partial c_p}{\partial \dot{m}_{HXLP}} = -\frac{P_{el} - \dot{Q}_{loss,fc}}{\dot{m}_{HXLP}^2 \Delta T_{HXLP}} \\
 c_3 &= \frac{\partial c_p}{\partial \Delta T_{HXLP}} = -\frac{P_{el} - \dot{Q}_{loss,fc}}{\dot{m}_{HXLP} \Delta T_{HXLP}^2}
 \end{aligned} \tag{5.2}$$

Type A and B can be combined with RSS (root-sum-of-squares) if they are not correlated, resulting in the overall uncertainty for the specific heat capacity.

$$\begin{aligned}
 u_c^2(c_{p,fc}) &= [u_{TypeA}^2(P_{el}) + u_{TypeB}^2(P_{el}) + u_{TypeA}^2(\dot{Q}_{loss,fc}) + u_{TypeB}^2(\dot{Q}_{loss,fc})] \cdot c_1^2 + \\
 &\quad (u_{TypeA}^2(\dot{m}_{HXLP}) + u_{TypeB}^2(\dot{m}_{HXLP})) \cdot c_2^2 + \\
 &\quad (u_{TypeA}^2(\Delta T) + u_{TypeB}^2(\Delta T)) \cdot c_3^2
 \end{aligned} \tag{5.3}$$

CP2 - flow calorimeter with heat exchanger

For the operation of the flow calorimeter in combination with the heat exchanger, the previously presented uncertainty analysis remains. The temperature prevailing at the mass flow sensor is lower due to the heat exchanger, which makes operation up to 430°C possible and reduces the uncertainty. Thus the prevailing temperature at the Coriolis sensor is accounted for in the type B uncertainty:

$$u_{TypeB}(\dot{m}_{HXLP}) = 0.6\% + 0.0032 \frac{\%}{^\circ\text{C}} \cdot T_{coriolis} \tag{5.4}$$

CP3 - flow calorimeter with heat exchanger and LDA massflow calibration

In this case, for the calculation of the heat capacity, the uncertainty for the mass flow sensor at temperatures up to 300 °C is assigned an uncertainty of 1 %. For temperatures below 125 °C, the existing calibration with the measurement uncertainty given in Table 5.1 provides a lower uncertainty and is considered instead.

CP4 - measurement of specific heat capacity in heat exchanger

For the calculation of the heat capacity in the heat exchanger, the calculation of the uncertainty is carried out similarly. But the HXLP is cooled instead and the transferred heat is determined based on the cooling water heat balance.

$$c_p = \frac{\dot{m}_{water} c_{p,water} \Delta T_{water} - \dot{Q}_{loss,he}}{\dot{m}_{HXLP} \Delta T_{HXLP}} \tag{5.5}$$

The sensitivity coefficients are calculated as follows:

$$\begin{aligned}
 c_4 &= \frac{\partial c_p}{\partial \dot{m}_{water}} = \frac{c_{p,water} \Delta T_{water}}{\dot{m}_{HXLP} \Delta T_{HXLP}} \\
 c_5 &= \frac{\partial c_p}{\partial c_{p,water}} = \frac{\dot{m}_{water} \Delta T_{water}}{\dot{m}_{HXLP} \Delta T_{HXLP}} \\
 c_6 &= \frac{c_p}{\partial \Delta T_{water}} = \frac{\dot{m}_{water} c_{p,water}}{\dot{m}_{HXLP} \Delta T} \\
 c_7 &= \frac{\partial c_p}{\partial \dot{Q}_{loss,he}} = \frac{1}{\dot{m}_{HXLP} \Delta T_{HXLP}} \\
 c_8 &= \frac{\partial c_p}{\partial \dot{m}_{HXLP}} = \frac{\dot{Q}_{loss,fc} - \dot{m}_{water} c_{p,water} \Delta T_{water}}{\dot{m}_{HXLP}^2 \Delta T_{HXLP}} \\
 c_9 &= \frac{\partial c_p}{\partial \Delta T_{HXLP}} = \frac{\dot{Q}_{loss,fc} - \dot{m}_{water} c_{p,water} \Delta T_{water}}{\dot{m}_{HXLP} \Delta T^2}
 \end{aligned} \tag{5.6}$$

The combined standard uncertainty for the specific heat capacity measurement is obtained according:

$$\begin{aligned}
 u_c^2(c_{p,he}) &= (u_{TypeA}^2(\dot{m}_{water}) + u_{TypeB}^2(\dot{m}_{water})) c_4^2 + u_{TypeB}^2(c_{p,water}) c_5^2 + \\
 &\quad (u_{TypeA}^2(\Delta T_{water}) + u_{TypeB}^2(\Delta T_{water})) c_6^2 + \\
 &\quad (u_{TypeA}^2(\dot{Q}_{loss,he}) + u_{TypeB}^2(\dot{Q}_{loss,he})) c_7^2 + \\
 &\quad (u_{TypeA}^2(\dot{m}_{HXLP}) + u_{TypeB}^2(\dot{m}_{HXLP})) c_8^2 + \\
 &\quad (u_{TypeA}^2(\Delta T_{HXLP}) + u_{TypeB}^2(\Delta T_{HXLP})) c_9^2 +
 \end{aligned} \tag{5.7}$$

5.1.1. Comparison of the Uncertainties for the Different Modes of Measuring the Specific Heat Capacity

In Figure 5.1 the four modes introduced in Section 5.1 are presented in terms of their measurement uncertainties over the operating temperature. The corresponding uncertainty is given for the operating temperature. The first Mode CP1- operation of the flow calorimeter without heat exchanger for measurements up to 350°C, shows an increase of the uncertainty from 1.4 % at 200°C to 1.87 % at 350°C. For the second case CP2 with the operation of the heat exchanger, measurements up to 430°C are possible and the uncertainty at 350°C is noted with 1.49 % and at 430°C with 1.75 %. In the case of the CP3, the LDA calibration of the mass flow sensor lowers the uncertainty of the measurements at increased temperatures. At an operating temperature of 430°C, an overall measurement uncertainty of 1.22 % can be achieved.

When measuring the specific heat capacity in the heat exchanger, the results for low fluid temperatures denoted with a higher uncertainty. Due to the reduced differential temperature between the inlet and outlet of the cooling water, the transferred heat can only be measured with increased uncertainty. At temperatures above 200 °C, on the other hand, the temperature difference of the cooling water is increased, thus the transferred heat is measured with a lower uncertainty. At a fluid temperature of 430°C, an uncertainty of 1.29 % can be achieved in the heat exchanger. It should be noted, the specific heat capacity is measured over a temperature difference of approx. 30 K when measuring in the heat exchanger, which results in significant linearisation uncertainties. In the flow calorimeter measurement points with more lower uncertainties can be adjusted.

Overall, the lowest uncertainty is achieved in the CP3 case when operating the flow calorimeter with the cooling of the heat exchanger and the LDA calibration. Compared to the initial state, the measurement uncertainty at 350°C was reduced from 1.87 % to 1.2 %, and the measurement range was increased to 430°C.

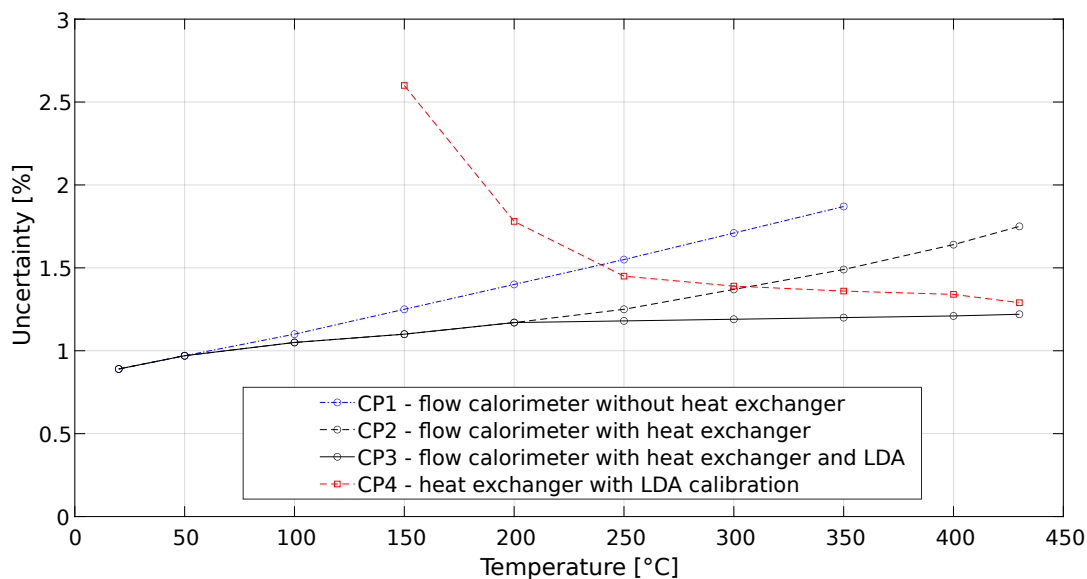


Figure 5.1.: Uncertainty of specific heat capacity for different modes of operation

5.2. Measurement Uncertainty of Specific Heat Transfer Coefficient

The calculation of the overall measurement uncertainty for the specific heat transfer coefficient α_{HXLP} is based on Equation: 5.8:

$$\alpha_{HXLP} = \frac{d_a}{\left(d_i \cdot \left(\frac{1}{k} - \frac{d_a \cdot \ln \frac{d_a}{d_i}}{2 \cdot \lambda_{steel}} - \frac{1}{\alpha_{water}} \right) \right)} \quad (5.8)$$

Integrated in this equation is the specific heat transfer coefficient of water α_{water} in the annular gap and the heat transmission coefficient k . The uncertainties for α_{water} and k need to be calculated and accounted for the overall uncertainty. The underlying type B uncertainties are given in Table 5.2. The diameter tolerances in the DIN standard for precision tubes such as d_a, d_i, D_i are given as equally distributed intervals. For the The type B standard deviation for uniformly distributed variables in an interval is given as:

$$u_{TypeB} = \frac{a}{\sqrt{3}} \quad (5.9)$$

| Measurand | Symbol | Uncertainty (u_{TypeB}) | Source |
|---------------------------------|-------------------|--------------------------------|--------------------------------------|
| Temperature difference | ΔT | 0.1 K | (Hilgert, Howar, et al., 2019, p. 9) |
| Outer diameter inner pipe | d_a | 0.05 mm | (DIN e.V., 2016, p. 14) |
| Inner diameter inner pipe | d_i | 0.09 mm | (DIN e.V., 2016, p. 14) |
| Inner diameter outer pipe | D_i | 0.09 mm | (DIN e.V., 2016, p. 14) |
| Length | L | 0.15 mm | (DIN e.V., 2016, p. 14) |
| Heat conductivity steel | λ_{steel} | 0.6 W /m K | (Blackwell et al., 2000, p. 10) |
| Mass flow water | \dot{m}_{water} | 0.1 % | (Yokogawa, 2020, p. 16) |
| Heat capacity water | cp_{water} | 0.3 % | (IAPWS, 2007, p. 47) |
| Heat transfer coefficient water | α_{water} | 1.49 % | |

Table 5.2.: Type B uncertainties of the individual measurands for calculating the overall measurement uncertainty for the specific heat transfer coefficient of HXLP in the heat exchanger

Uncertainty of the Heat Transfer of Water in the Annular Gap

The convective heat transfer is calculated using the Gnielinski annular gap calculation method presented in Chapter 2.8.2. The total uncertainty is determined by the partial derivatives of α_{water} , with respect to the influence parameters given in formula 5.10:

$$u_c(\alpha_{water}) = f(\dot{m}_{water}; \rho_{water}; D_i; d_a; \eta_{water}; cp_{water}; \lambda_{water}; L) \quad (5.10)$$

The properties of water ($\rho_{water}; \eta_{water}; cp_{water}; \lambda_{water}$) are given with an uncertainty of 0.3 % (IAPWS, 2007, p. 47). For the mass flow and the geometry, the uncertainties from Table 5.2 apply. The calculation of the partial derivatives in combination with the type B uncertainties leads to a combined uncertainty of 1.49 %, whereby the inner diameter of the outer pipe d_i with a share of 82 % and the outer diameter of the inner pipe d_a with a share of 16 % dominate the uncertainty of α_{water} . As the terms of the partial derivative are very long, the code for the calculation can be found in Appendix D.

Uncertainty of the Heat Transmission

The uncertainty of the heat transmission coefficient k in Formula 5.11 is obtained by partial derivation by its influencing parameters.

$$k = \frac{\Delta T_{\text{water}} \cdot cp_{\text{water}} \cdot \dot{m}_{\text{water}} - Q_{\text{loss}}}{d_a \cdot \Delta \vartheta_{\text{ln}} \cdot L \cdot \pi} \quad (5.11)$$

The partial derivatives lead to:

$$\begin{aligned} c_{10} &= \frac{\partial k}{\partial \dot{m}_{\text{water}}} = \frac{\Delta T_{\text{water}} \cdot cp_{\text{water}}}{d_a \cdot \Delta \vartheta_{\text{ln}} \cdot L \cdot \pi} \\ c_{11} &= \frac{\partial k}{\partial cp_{\text{water}}} = \frac{\Delta T_{\text{water}} \cdot \dot{m}_{\text{water}}}{d_a \cdot \Delta \vartheta_{\text{ln}} \cdot L \cdot \pi} \\ c_{12} &= \frac{\partial k}{\partial \Delta T_{\text{water}}} = \frac{cp_{\text{water}} \cdot \dot{m}_{\text{water}}}{d_a \cdot \Delta \vartheta_{\text{ln}} \cdot L \cdot \pi} \\ c_{13} &= \frac{\partial k}{\partial Q_{\text{loss}}} = -\frac{1}{d_a \cdot \Delta \vartheta_{\text{ln}} \cdot L \cdot \pi} \\ c_{14} &= \frac{\partial k}{\partial d_a} = \frac{Q_{\text{loss}} - \Delta T_{\text{water}} \cdot cp_{\text{water}} \cdot \dot{m}_{\text{water}}}{d_a^2 \cdot \Delta \vartheta_{\text{ln}} \cdot L \cdot \pi} \\ c_{15} &= \frac{\partial k}{\partial L} = \frac{Q_{\text{loss}} - \Delta T_{\text{water}} \cdot cp_{\text{water}} \cdot \dot{m}_{\text{water}}}{d_a \cdot \Delta \vartheta_{\text{ln}} \cdot L^2 \cdot \pi} \\ c_{16} &= \frac{\partial k}{\partial \Delta \vartheta_{\text{ln}}} = \frac{Q_{\text{loss}} - \Delta T_{\text{water}} \cdot cp_{\text{water}} \cdot \dot{m}_{\text{water}}}{d_a \cdot \Delta \vartheta_{\text{ln}}^2 \cdot L \cdot \pi} \end{aligned} \quad (5.12)$$

The total combined standard uncertainty for the measurement of the specific heat transmission coefficient k is thus obtained as:

$$\begin{aligned} u_c^2(k) &= (u_{\text{TypeA}}^2(\dot{m}_{\text{water}}) + u_{\text{TypeB}}^2(\dot{m}_{\text{water}})) \cdot c_{10}^2 + u_{\text{TypeB}}^2(cp_{\text{water}}) \cdot c_{11}^2 + \\ &\quad (u_{\text{TypeA}}^2(\Delta T_{\text{water}}) + u_{\text{TypeB}}^2(\Delta T)) \cdot c_{12}^2 + \\ &\quad (u_{\text{TypeA}}^2(Q_{\text{loss}}) + u_{\text{TypeB}}^2(Q_{\text{loss}})) \cdot c_{13}^2 + u_{\text{TypeB}}^2(d_a) \cdot c_{14}^2 + \\ &\quad u_{\text{TypeB}}^2(L) \cdot c_{15}^2 + (u_{\text{TypeA}}^2(\Delta \vartheta_{\text{ln}}) + u_{\text{TypeB}}^2(\Delta T)) \cdot c_{16}^2 \end{aligned} \quad (5.13)$$

With the type B uncertainties given in Table 5.2, an overall uncertainty of 0.75 % is obtained for the heat transmission coefficient k , whereby the uncertainty of the temperature measurement accounts for the largest share of the uncertainty. The impact of the other parameters are presented in the pie chart in Figure 5.2.

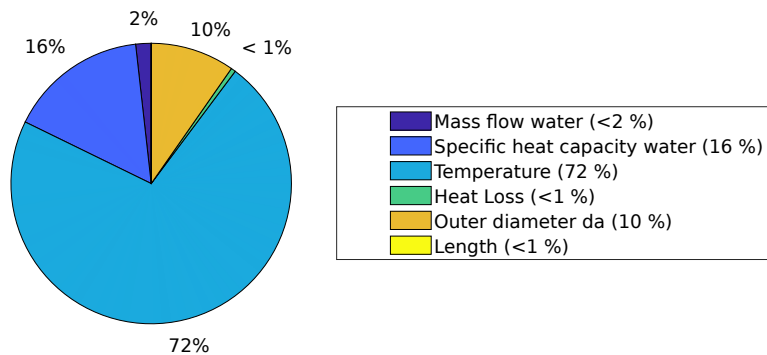


Figure 5.2.: Pie chart of uncertainty contributions from different sources for the heat transmission coefficient k

Overall Uncertainty of the Heat Transfer of HXLP

With the uncertainty estimation of α_{water} and k , the uncertainty for α_{HXLP} can be determined using the partial derivative of α_{HXLP} in Equation (5.8) with respect to all influence parameters given in formula 5.14:

$$u_c(\alpha_{\text{HXLP}}) = f(d_a, d_i, D_i, \lambda_{\text{steel}}, k, \alpha_{\text{water}}) \quad (5.14)$$

The combined overall uncertainty is obtained with Formula 5.15. The partial derivatives are given in Appendix D.1.

$$\begin{aligned} u_c^2(\alpha_{\text{HXLP}}) = & u_{\text{TypeB}}^2(d_a) \cdot \left(\frac{\partial \alpha_{\text{HXLP}}}{\partial d_a} \right)^2 + u_{\text{TypeB}}^2(d_i) \cdot \left(\frac{\partial \alpha_{\text{HXLP}}}{\partial d_i} \right)^2 + \\ & u_{\text{TypeB}}^2(D_i) \cdot \left(\frac{\partial \alpha_{\text{HXLP}}}{\partial D_i} \right)^2 + u_{\text{TypeB}}^2(\lambda_{\text{steel}}) \cdot \left(\frac{\partial \alpha_{\text{HXLP}}}{\partial \lambda_{\text{steel}}} \right)^2 + \\ & u_{\text{TypeA}}^2(k) \cdot \left(\frac{\partial \alpha_{\text{HXLP}}}{\partial k} \right)^2 + u_{\text{TypeA}}^2(\alpha_{\text{water}}) \cdot \left(\frac{\partial \alpha_{\text{HXLP}}}{\partial \alpha_{\text{water}}} \right)^2 + \end{aligned} \quad (5.15)$$

With the presented design of the measurement heat exchanger in Chapter 3.2 an overall uncertainty of 1.46 % can be achieved for the measurement of the heat transfer coefficient of HXLP at a temperature of 430 °C. The sensitive measurands are the inner diameter, the temperature measurement, the thermal conductivity of water and the outer diameter of the inner pipe. For measurements at temperatures below 200 °C, the measurement uncertainty increases to 1.8 % and the influence of the temperature measurement on the overall uncertainty increases, see Figure 5.3. The reason is given in the lower temperature difference between inlet and outlet temperatures in the cooling water, resulting in a more uncertain measurement of the transferred heat. In addition, the logarithmic temperature difference between the heat exchanging fluids HXLP and water gets lower. Nevertheless, the increased uncertainty due to the temperature measurement is very small and measurements with a low uncertainty can be conducted, especially at the relevant operation point at 430 °C to investigate the application limits of HXLP.

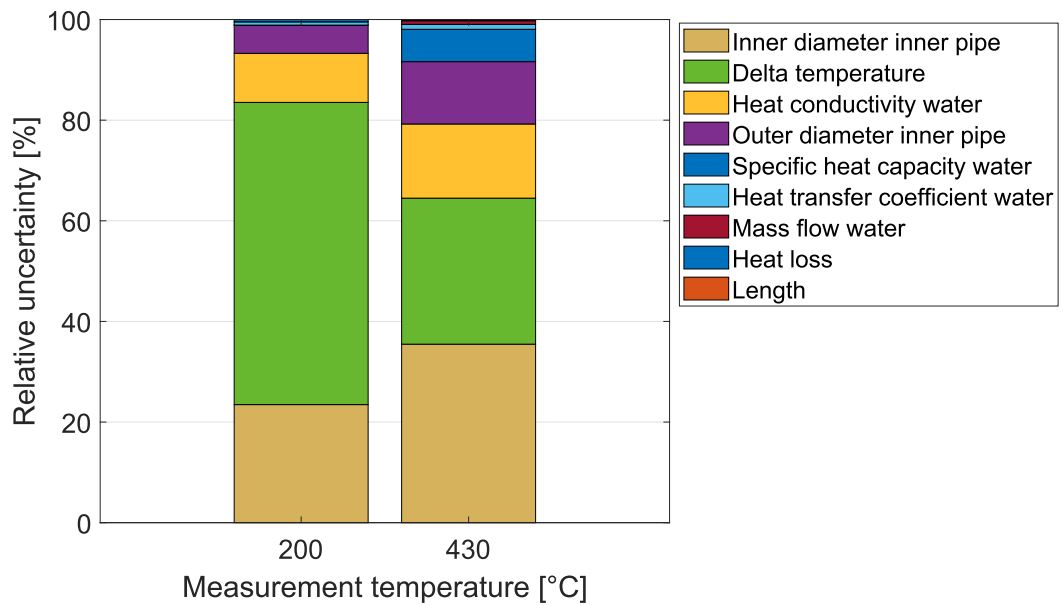


Figure 5.3.: Proportion of the influence parameters in the overall uncertainty for the heat transfer coefficient for HXLP at different fluid temperatures

6. Conclusion and Outlook

This thesis was dedicated to designing a measurement bypass. Hence, an existing flow calorimeter was enhanced and a measurement heat exchanger was designed, to measure the specific heat capacity and the heat transfer coefficient of HXLP under typical operation conditions at the PROMETEO PTC test loop at PSA.

For the measurement of the heat capacity, an existing flow calorimeter was adapted for the increased temperatures up to 430 °C. The implementation of an inline cooler enables mass flow measurements at lower temperatures, thus reducing the corresponding uncertainty and complies with the sensor's maximum operating temperature of 350 °C. Additionally, the pipe design enables the option to install a measurement section for calibrating the mass flow sensor with laser Doppler anemometry at temperatures up to 300 °C.

For the measurement of the heat transfer coefficient of HXLP under typical parabolic trough loop conditions, a measurement heat exchanger was designed based on a counter flow double pipe heat exchanger for straightforward applicability of the equations for comparison. By identifying the sensitive measurands and their influence on the measurement uncertainty, several implementations were made to promise an overall uncertainty of 1.2 % for the specific heat capacity and 1.46 % for the heat transfer coefficient at 430 °C. These implementations include a temperature measurement chamber with fourfold redundant differential calibrated 1/10 class B Pt100 sensors at the in- and outlets of the water and HXLP flow.

The influence of the surroundings on the temperature chamber was minimized by the sake of CFD simulations for different immersion depths of the sensors. Resulting in a design with guided sensor, 65 mm from the inlet T-piece with negligible influence of the surroundings. The geometry of the measurement heat exchanger was optimized for a suitable temperature spread to measure the differential temperature with a given measurement uncertainty of 0.1 K.

Precision pipes were implemented for lowest possible uncertainties for the determination of the heat-transferring geometry. The temperature differences between the inner and outer pipe inevitably lead to thermal stresses, which required axial compensation to lower stresses. Thus a tailored stuffing box was designed in order to minimize the systematic influence in the measurement by avoiding larger technical solutions like a bellow axial compensator. The unavoidable heat losses that occur over the surface of the outer pipe, have been made largely independent of the surroundings by means of appropriate insulation and preventing pipe support over the length of the measurement heat exchanger. The heat losses can be determined with several temperature sensors distributed around the circumference and compensated during measurements.

The PROMETEO loop was not in operation during the examination period and the measurement heat exchanger was in manufacturing, thus no measurements were conducted on HXLP. Comparative measurements of the specific heat capacity in the flow calorimeter with water at ambient temperature generated valid results after the enhancement with a deviation of 0.05 % to the IAPWS reference and a measurement uncertainty of 1.5 %. To simulate measurements on the measurement heat exchanger, a realistic data set was generated based on PROMETEO process data. An evaluation routine was established to automatically perform the measurement analysis, incorporating statistical and known systematic uncertainties.

A comprehensive uncertainty analysis showed the enhanced flow calorimeter enables measurements up to 430 °C, with an uncertainty reduced from the initial 1.87 % at 350 °C (application limit) to 1.22 % at 430 °C with HTF cooler and LDA calibration section. Using the measurement

6. Conclusion and Outlook

heat exchanger to determine the heat capacity showed uncertainties at 430°C of 1.29 %. However, the uncertainties increase at lower temperatures as the differential temperatures get smaller and thus the relative uncertainty of the temperature measurement increases. For measuring the heat transfer coefficient of HXLP, the diameters of the inner pipe and the temperature measurement stated a significant influence on the overall uncertainty. An uncertainty of 1.46 % at 430 °C could be achieved, which represents a favorable result in the context of the measurement at loop scale.

Following up on this work, the diameters of the installed pipes have to be measured using a micrometer, as these have a strong sensitivity to the overall uncertainty. Furthermore, comparative measurements should be carried out with water in the measurement heat exchanger, in order to prove the applicability and uncertainty of the Gnielinski method to calculate the convective heat transfer coefficient in the annular gap for water. Overall, following this work, the improved fluid properties of HXLP can be demonstrated at loop scale at 430 °C, lowering the implementation hurdles for new CSP projects.

Bibliography

- Ala-Outinen, T. (1996). *Fire resistance of austenitic stainless steels Polarit 725 (EN 1.4301) and Polarit 761 (EN 1.4571)*. Espoo. ISBN: 951-38-4915-5.
- Alexopoulos, S. and S. Kalogirou (2022). *Solar Thermal Energy - A Volume in the Encyclopedia of Sustainability Science and Technology*. Vol. 2. Springer. ISBN: 978-1-0716-1421-1.
- Bahrami, M. (2009). *Forced Convection Heat Transfer*. Manuscript. URL: <https://www.sfu.ca/~mbahrami/ENSC%5C%20388/Notes/Forced%5C%20Convection.pdf>.
- BIPM (2008). *Evaluation of measurement data | Guide to the expression of uncertainty in measurement*. JCGM 100:2008. URL: https://www.bipm.org/documents/20126/2071204/JCGM_100_2008_E.pdf/cb0ef43f-baa5-11cf-3f85-4dcd86f77bd6.
- Blackwell, B., W. Gill, K. Dowding, and R. Easterling (2000). "Uncertainty Estimation in the Determination of Thermal Conductivity of 304 Stainless Steel". In: *IMECE*. URL: <https://www.osti.gov/servlets/purl/764054>.
- Böckh, P. and T. Wetzel (2015). *Wärmeübertragung*. 6th ed. Berlin, Heidelberg: Springer Vieweg. ISBN: 978-3-662-44477-1. DOI: <https://doi.org/10.1007/978-3-662-44477-1>.
- Chen, Q., Y. Wang, J. Zhang, and Z. Wang (2020). "The Knowledge Mapping of Concentrating Solar Power Development Based on Literature Analysis Technology". In: *Energies*. DOI: 10.3390/en13081988.
- DIN (2022). *DIN 4140 Dämmarbeiten an betriebstechnischen Anlagen in der Industrie und in der technischen Gebäudeausrüstung – Ausführung von Wärme- und Kälte­dämmungen; Legal Rule or Regulation*.
- DIN e.V., D. I. f. N. (2016). *DIN EN 10305-1 Präzisionsstahlrohre Technische Lieferbedingungen – Teil 1: Nahtlose kaltgezogene Rohre; Deutsche Fassung*. Legal Rule or Regulation.
- DLR (2023). *CIEMAT Plataforma Solar de Almería -Praxisnahe Bedingungen im größten europäischen Testzentrum für Concentrated Solar Power (CSP)*. Web Page. URL: https://www.dlr.de/sf/de/desktopdefault.aspx/tabid-7176/11942_read-28189/.
- Emerson (2021). *Fisher ET und EAT easy-e Ventile Class 125 bis Class 600 - Betriebsanleitung*. Tech. rep.
- Frantz, C., R. Bucka, and B. Röger M. and Hoffschmidt (2022). "Experimental Analysis of Forced Convective Heat Transfer of Nitrate Salt in a Circular Tube at High Reynolds Numbers and Temperatures". In: *International Journal of Heat and Mass Transfer* 201. DOI: <https://doi.org/10.1016/j.ijheatmasstransfer.2022.123563>.
- Günther, F. W. and S. Faltermaier (2018). *Prüfung von Rohrleitungen*. Ed. by H.-B. Horlacher and U. Helbig. Berlin, Heidelberg: Springer Berlin Heidelberg, pp. 489–495. ISBN: 978-3-662-50355-3. DOI: 10.1007/978-3-662-50355-3_113. URL: https://doi.org/10.1007/978-3-662-50355-3_113.
- Hannoschöck, N. (2018). *Wärmeleitung und -transport - Grundlagen der Wärme- und Stoffübertragung*. Berlin Heidelberg New York: Springer-Verlag. ISBN: 978-3-662-57572-7.
- Heidemann, D.-I. . W. (2022). *Berechnung von Wärmeübertragern*. Manuscript.
- Heitmann, F., M. Juling, and J. Steinbock (2020). "Performance of the LDA Volumetric Flow Rate Standard Under Severely Disturbed Flow Conditions". In: *Flow Measurement and Instrumentation* 74. DOI: <https://doi.org/10.1016/j.flowmeasinst.2020.101756>.
- Hilgert, C., C. Jung, L. Valenzuela, E. Schaffer, and D. Lei (2021). *Silicone-Based Heat Transfer Fluids (SiHTF) in Line Focusing Concentrating Solar Power Applications*. Conference Paper.

- Hilgert, C. (2020). *Vorhabensbeschreibung SING, (Silicone Fluid Next Generation)*. Web Page. URL: https://www.dlr.de/sf/en/desktopdefault.aspx/tabid-9315/22254_read-73739/.
- Hilgert, C., F. Howar, and M. Röger (2019). “Flow through calorimeter to measure fluid heat capacity in CSP applications”. In: *Solar Energy* 194, pp. 804–814. ISSN: 0038-092X. DOI: <https://doi.org/10.1016/j.solener.2019.11.029>. URL: <https://www.sciencedirect.com/science/article/pii/S0038092X19311302>.
- Hirsch, T. (2021). *Solarthermische Kraftwerke: Parabolrinnenkraftwerke mit Flüssigsalz*. Manuscript.
- Howar, F. (2016). “On-line heat capacity measurements of a silicone based heat transfer fluid for concentrated solar power applications”. Thesis.
- IAPWS (2007). *The International Association for the Properties of Water and Steam - Revised Release on the IAPWS Industrial Formulation 1997 for the Thermodynamic Properties of Water and Steam*. Aggregated Database.
- Juling, M. (2016). “Rückgeführte Volumenstrommessung mittels orts aufgelöster Laser-Doppler-Anemometrie”. Thesis.
- Kandlikar, S. G. and R. K. Shah (1989). “Multipass Plate Heat Exchangers—Effectiveness-NTU Results and Guidelines for Selecting Pass Arrangements”. In: *Journal of Heat Transfer* 111.2, pp. 300–313. ISSN: 0022-1481. DOI: 10.1115/1.3250678. URL: <https://doi.org/10.1115/1.3250678>.
- Kerkwijk, A. (2016). “Quantifying heat loss through pipe shoe supports”. Thesis.
- Kerskes, H. (2021). *Thermische Energiespeicher I - Speicherung fühlbarer Wärme 4*. Manuscript.
- Kugi, A., T. Glück, W. Kemmetmüller, and A. Steinböck (2016). *Vorlesung und Übung Modellbildung*. Manuscript. URL: https://www.acin.tuwien.ac.at/fileadmin/cds/lehre/mblg/Modellbildung_Kapitel_3.pdf.
- Küppers, M. (2004). *Betriebsanleitung RHEONIK Massedurchflussmesser RHE 07, 08, 11*. Tech. rep. URL: www.rheonik.de.
- Kuyatt and Taylor (1994). “Guidelines for Evaluating and Expressing the Uncertainty of NIST Measurement Results”. In: URL: <https://nvlpubs.nist.gov/nistpubs/Legacy/TN/nbstechnicalnote1297.pdf>.
- Lovegrove, K. and W. Stein (2012). *Concentrating Solar Power Technology - Principles, Developments and Applications*. Woodhead Publishing. ISBN: 978-1-84569-769-3.
- Lüpfert, E., E. Zarza-Moya, and M. Geyer (2003). “Eurotrough collector qualification complete-performance test results from PSA”. In.
- Mukund, H. B. and B. Santanu (2012). “Targeting Minimum Heat Transfer Fluid Flow for Multiple Heat Demands”. In: *11th International Symposium on Process Systems Engineering*. Ed. by A. K. Iftekhar and S. Rajagopalan. Vol. 31. Elsevier, pp. 675–679. DOI: <https://doi.org/10.1016/B978-0-444-59507-2.50127-X>. URL: <https://www.sciencedirect.com/science/article/pii/B978044459507250127X>.
- Müller-Steinhagen, H. and F. Trieb (2004). “Concentrating solar power - A review of the technology”. In.
- Njore, M. Sinton, and J. Edwards (2021). “WorldBank CSP Report - Concentrating Solar Power - Clean Power on Demand 24/7”. In: URL: <https://pubdocs.worldbank.org/en/849341611761898393/WorldBank-CSP-Report-Concentrating-Solar-Power-Clean-Power-on-Demand-24-7-FINAL.pdf>.
- Pitz-Paal, R., T. Wetzel, P. Nitz, and J. Terrapon-Pfaff (2018). *Solarthermische Kraftwerke*. Conference Paper. URL: <https://elib.dlr.de/124274/>.
- Thomas Bornath, G. W. (2020). *Messunsicherheiten – Anwendungen*. Springer Spektrum Wiesbaden. ISBN: 978-3-658-30565-9. DOI: <https://doi.org/10.1007/978-3-658-30565-9>.
- United-Nations (1987). *Report of the World Commission on Environment and Development - Our Common Future*. Report.
- VDI, V. d. I. (2013). *VDI-Wärmeatlas*. Vol. 11. Berlin Heidelberg: Springer. ISBN: 978-3-642-19981-3. DOI: 10.1007/978-3-642-19981-3.
- Vignarooban, K., X. Xinhai, A. Arvay, K. Hsu, and A. M. Kannan (2015). “Heat transfer fluids for concentrating solar power systems – A review”. In: *Applied Energy* 146, pp. 383–396. ISSN:

- 0306-2619. DOI: <https://doi.org/10.1016/j.apenergy.2015.01.125>. URL: <https://www.sciencedirect.com/science/article/pii/S0306261915001634>.
- Wacker, C. A. (2022). *TDS Technisches Datenblatt*. Report. URL: <https://www.wacker.com/h/de-de/medias/HELISOL-XLP-de-2022.06.28.pdf>.
- Wehner, K. (2022). “Techno-economic evaluation of a full heat transfer fluid changeover in an existing parabolic trough power plant”. Thesis.
- Yokogawa (2020). *Produktspezifikation ROTAMASS Total Insight Coriolis-Massedurchfluss- und Dichtemessgerät*. Tech. rep.
- Zheng, X., X. Zhang, J. Gao, L. Ma, W. Wang, J. Xu, and J. Yu (2019). “Heat Loss Characteristics of Pipe Flange Joints: Experiments and Simulations”. In: *Journal of Pressure Vessel Technology* 142.2. ISSN: 0094-9930. DOI: 10.1115/1.4044754. URL: <https://doi.org/10.1115/1.4044754>.

A. Data Sheet of HELISOL[®] XLP

| Temperature [°C] | Viscosity [mPas] | Thermal conductivity [W/m ² K] | Density at 20 bar [kg/m ³] | Heat capacity at 20 bar [J/kg K] |
|---------------------|---------------------|--|---|-------------------------------------|
| -40 | 68.51 | 0.1542 | 1014.2 | 1.374 |
| -35 | 57.81 | 0.1526 | 1008.6 | 1.379 |
| -30 | 49.16 | 0.1511 | 1003.2 | 1.385 |
| -25 | 42.11 | 0.1496 | 997.8 | 1.391 |
| -20 | 36.32 | 0.1481 | 992.4 | 1.397 |
| -15 | 31.53 | 0.1466 | 987.2 | 1.404 |
| -10 | 27.53 | 0.1451 | 982 | 1.411 |
| -5 | 24.17 | 0.1437 | 976.8 | 1.419 |
| 0 | 21.34 | 0.1422 | 965 | 1.426 |
| 5 | 18.93 | 0.1408 | 962 | 1.435 |
| 10 | 16.87 | 0.1394 | 958.9 | 1.443 |
| 15 | 15.1 | 0.138 | 955.5 | 1.452 |
| 20 | 13.58 | 0.1366 | 952.1 | 1.461 |
| 25 | 12.25 | 0.1352 | 948.5 | 1.47 |
| 30 | 11.1 | 0.1339 | 944.8 | 1.479 |
| 35 | 10.09 | 0.1326 | 940.9 | 1.489 |
| 40 | 9.2 | 0.1312 | 937 | 1.499 |
| 45 | 8.42 | 0.1299 | 932.9 | 1.509 |
| 50 | 7.72 | 0.1286 | 928.8 | 1.519 |
| 55 | 7.11 | 0.1274 | 924.5 | 1.529 |
| 60 | 6.56 | 0.1261 | 920.2 | 1.54 |
| 65 | 6.07 | 0.1248 | 915.7 | 1.55 |
| 70 | 5.63 | 0.1236 | 911.2 | 1.561 |
| 75 | 5.23 | 0.1224 | 906.6 | 1.572 |
| 80 | 4.87 | 0.1212 | 902 | 1.583 |
| 85 | 4.55 | 0.12 | 897.3 | 1.594 |
| 90 | 4.26 | 0.1188 | 892.6 | 1.605 |
| 95 | 3.99 | 0.1177 | 887.9 | 1.616 |
| 100 | 3.75 | 0.1165 | 883.1 | 1.628 |
| 105 | 3.53 | 0.1154 | 878.2 | 1.639 |
| 110 | 3.32 | 0.1143 | 873.4 | 1.65 |
| 115 | 3.14 | 0.1132 | 868.5 | 1.662 |
| 120 | 2.97 | 0.1121 | 863.6 | 1.673 |
| 125 | 2.81 | 0.111 | 858.7 | 1.685 |
| 130 | 2.66 | 0.1099 | 853.7 | 1.696 |
| 135 | 2.53 | 0.1089 | 848.8 | 1.708 |
| 140 | 2.4 | 0.1079 | 843.9 | 1.72 |
| 145 | 2.29 | 0.1069 | 838.9 | 1.731 |
| 150 | 2.18 | 0.1059 | 834 | 1.743 |

A. Data Sheet of HELISOL[®] XLP

| Temperature [°C] | Viscosity [mPas] | Thermal conductivity [W/m ² K] | Density at 20 bar [kg/m ³] | Heat capacity at 20 bar [J/kg K] |
|---------------------|---------------------|--|---|-------------------------------------|
| 155 | 2.08 | 0.1049 | 829 | 1.755 |
| 160 | 1.99 | 0.1039 | 824.1 | 1.766 |
| 165 | 1.9 | 0.103 | 819.2 | 1.778 |
| 170 | 1.82 | 0.102 | 814.3 | 1.79 |
| 175 | 1.75 | 0.1011 | 809.4 | 1.802 |
| 180 | 1.68 | 0.1002 | 804.5 | 1.814 |
| 185 | 1.61 | 0.0993 | 799.6 | 1.826 |
| 190 | 1.55 | 0.0984 | 794.7 | 1.838 |
| 195 | 1.49 | 0.0975 | 789.9 | 1.849 |
| 200 | 1.43 | 0.0967 | 785.1 | 1.861 |
| 205 | 1.38 | 0.0959 | 780.2 | 1.873 |
| 210 | 1.33 | 0.095 | 775.4 | 1.885 |
| 215 | 1.29 | 0.0942 | 770.7 | 1.898 |
| 220 | 1.24 | 0.0934 | 765.9 | 1.91 |
| 225 | 1.2 | 0.0927 | 761.1 | 1.922 |
| 230 | 1.16 | 0.0919 | 756.4 | 1.934 |
| 235 | 1.13 | 0.0912 | 751.6 | 1.946 |
| 240 | 1.09 | 0.0904 | 746.9 | 1.958 |
| 245 | 1.06 | 0.0897 | 742.2 | 1.971 |
| 250 | 1.03 | 0.089 | 737.5 | 1.983 |
| 255 | 1 | 0.0883 | 732.8 | 1.995 |
| 260 | 0.97 | 0.0876 | 728.1 | 2.008 |
| 265 | 0.94 | 0.087 | 723.4 | 2.021 |
| 270 | 0.91 | 0.0863 | 718.6 | 2.033 |
| 275 | 0.89 | 0.0857 | 713.9 | 2.046 |
| 280 | 0.86 | 0.0851 | 709.2 | 2.059 |
| 285 | 0.84 | 0.0845 | 704.4 | 2.072 |
| 290 | 0.82 | 0.0839 | 699.6 | 2.085 |
| 295 | 0.8 | 0.0833 | 694.8 | 2.098 |
| 300 | 0.78 | 0.0828 | 690 | 2.111 |
| 305 | 0.76 | 0.0822 | 685.1 | 2.124 |
| 310 | 0.74 | 0.0817 | 680.3 | 2.138 |
| 315 | 0.72 | 0.0812 | 675.3 | 2.151 |
| 320 | 0.71 | 0.0807 | 670.3 | 2.165 |
| 325 | 0.69 | 0.0802 | 665.2 | 2.179 |
| 330 | 0.68 | 0.0798 | 660.1 | 2.194 |
| 335 | 0.66 | 0.0793 | 654.9 | 2.208 |
| 340 | 0.65 | 0.0789 | 649.7 | 2.223 |
| 345 | 0.63 | 0.0784 | 644.3 | 2.238 |
| 350 | 0.62 | 0.078 | 638.9 | 2.253 |
| 355 | 0.61 | 0.0776 | 633.4 | 2.268 |
| 360 | 0.6 | 0.0773 | 627.8 | 2.284 |
| 365 | 0.58 | 0.0769 | 622 | 2.3 |
| 370 | 0.57 | 0.0766 | 616.2 | 2.316 |

| Temperature [°C] | Viscosity [mPas] | Thermal conductivity [W/m ² K] | Density at 20 bar [kg/m ³] | Heat capacity at 20 bar [J/kg K] |
|---------------------|---------------------|--|---|-------------------------------------|
| 375 | 0.56 | 0.0762 | 610.2 | 2.332 |
| 380 | 0.55 | 0.0759 | 604.1 | 2.348 |
| 385 | 0.54 | 0.0756 | 597.8 | 2.365 |
| 390 | 0.53 | 0.0753 | 591.5 | 2.38 |
| 395 | 0.52 | 0.075 | 584.8 | 2.396 |
| 400 | 0.51 | 0.0748 | 578.1 | 2.41 |
| 405 | 0.5 | 0.0745 | 571.1 | 2.423 |
| 410 | 0.49 | 0.0743 | 564.1 | 2.435 |
| 415 | 0.49 | 0.0741 | 556.7 | 2.443 |
| 420 | 0.48 | 0.0739 | 549.3 | 2.449 |
| 425 | 0.47 | 0.0737 | 541.4 | 2.452 |
| 430 | 0.46 | 0.0735 | 533.5 | 2.452 |
| 435 | 0.45 | 0.0734 | 525.2 | 2.449 |
| 440 | 0.45 | 0.0732 | 516.8 | 2.445 |
| 445 | 0.44 | 0.0731 | 507.9 | 2.438 |
| 450 | 0.43 | 0.073 | 499 | 2.432 |

Table A.1.: Physical properties of HELISOL[®] XLP in use based on laboratory data by Wacker

B. Enhancement of the Flow Calorimeter

B.1. ROHR2 Stress Simulation

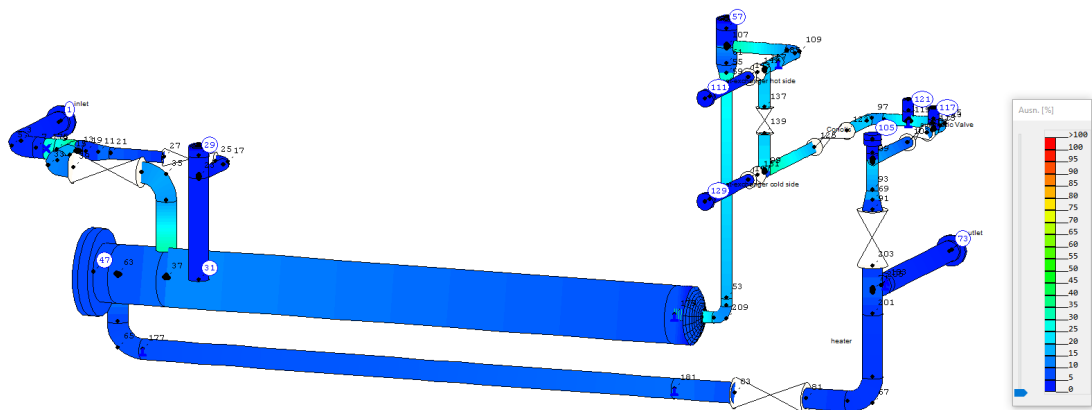


Figure B.1.: Results of ROHR2 stress simulation for case 1 with 41.1% utilisation of the strength

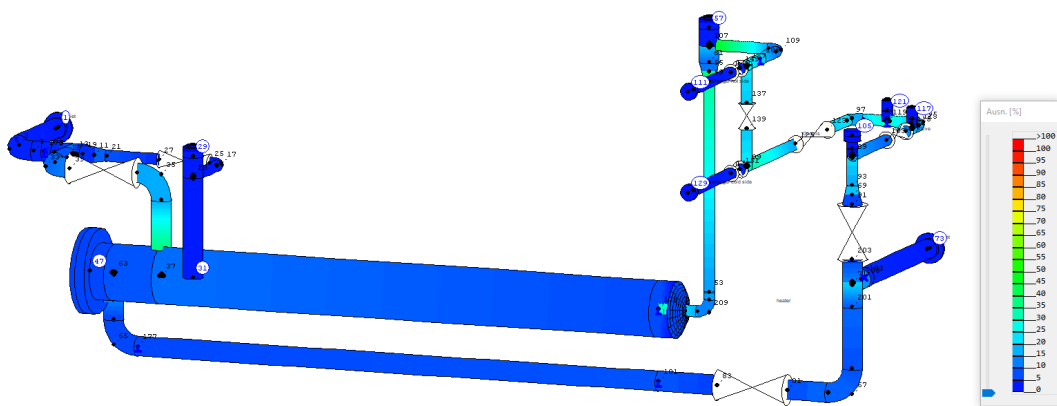


Figure B.2.: Results of ROHR2 stress simulation for case 2 with 46% utilisation of the strength

B. Enhancement of the Flow Calorimeter

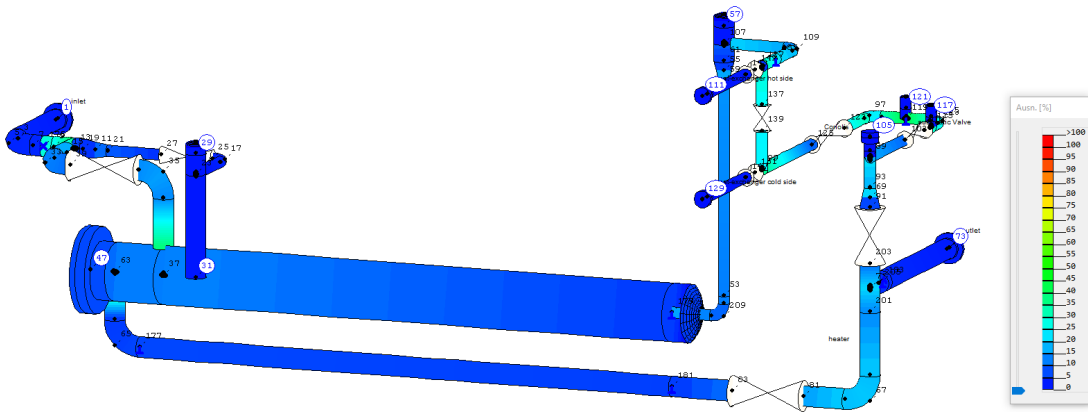


Figure B.3.: Results of ROHR2 stress simulation for case 3 with 42.5% utilisation of the strength

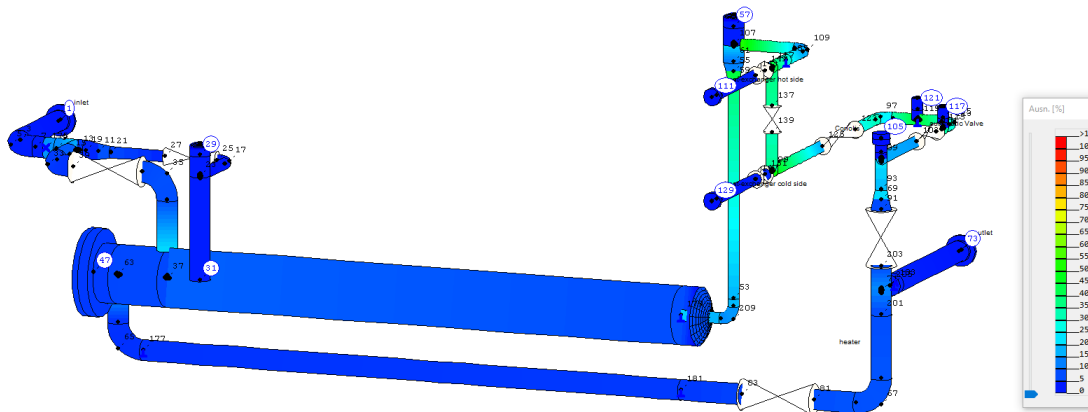


Figure B.4.: Results of ROHR2 stress simulation for case 4 with 52.6% utilisation of the strength

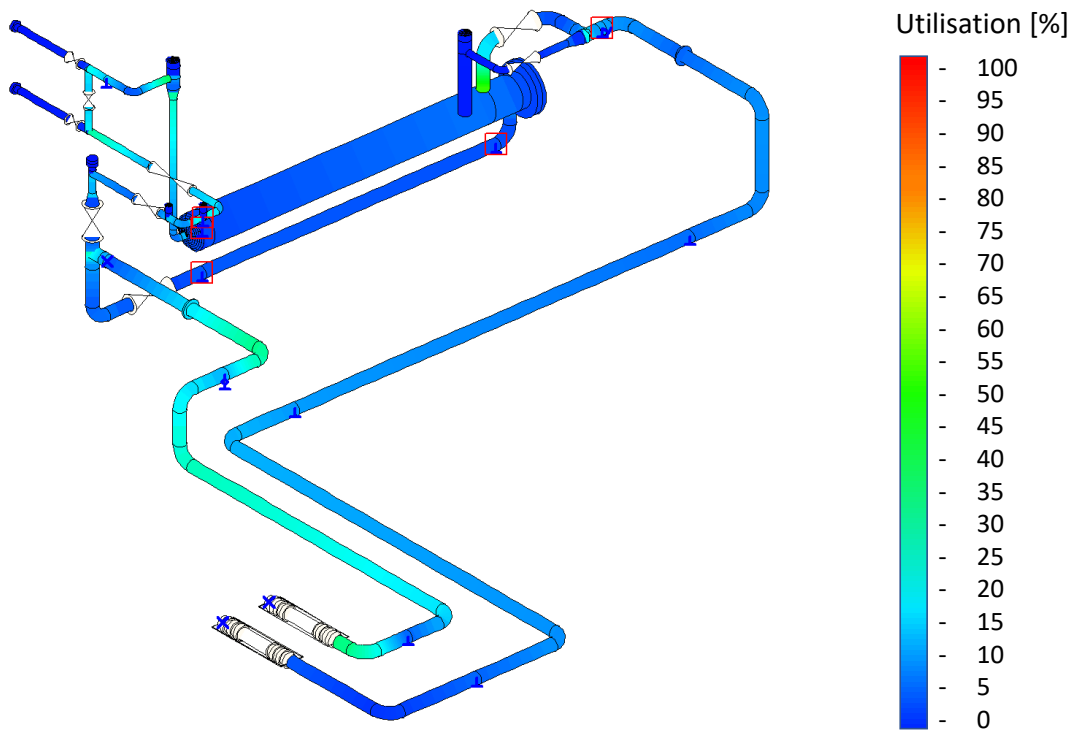


Figure B.5.: Flow calorimeter with measurement bypass at PROMETEO facility

C. Design of the Measurement Heat Exchanger

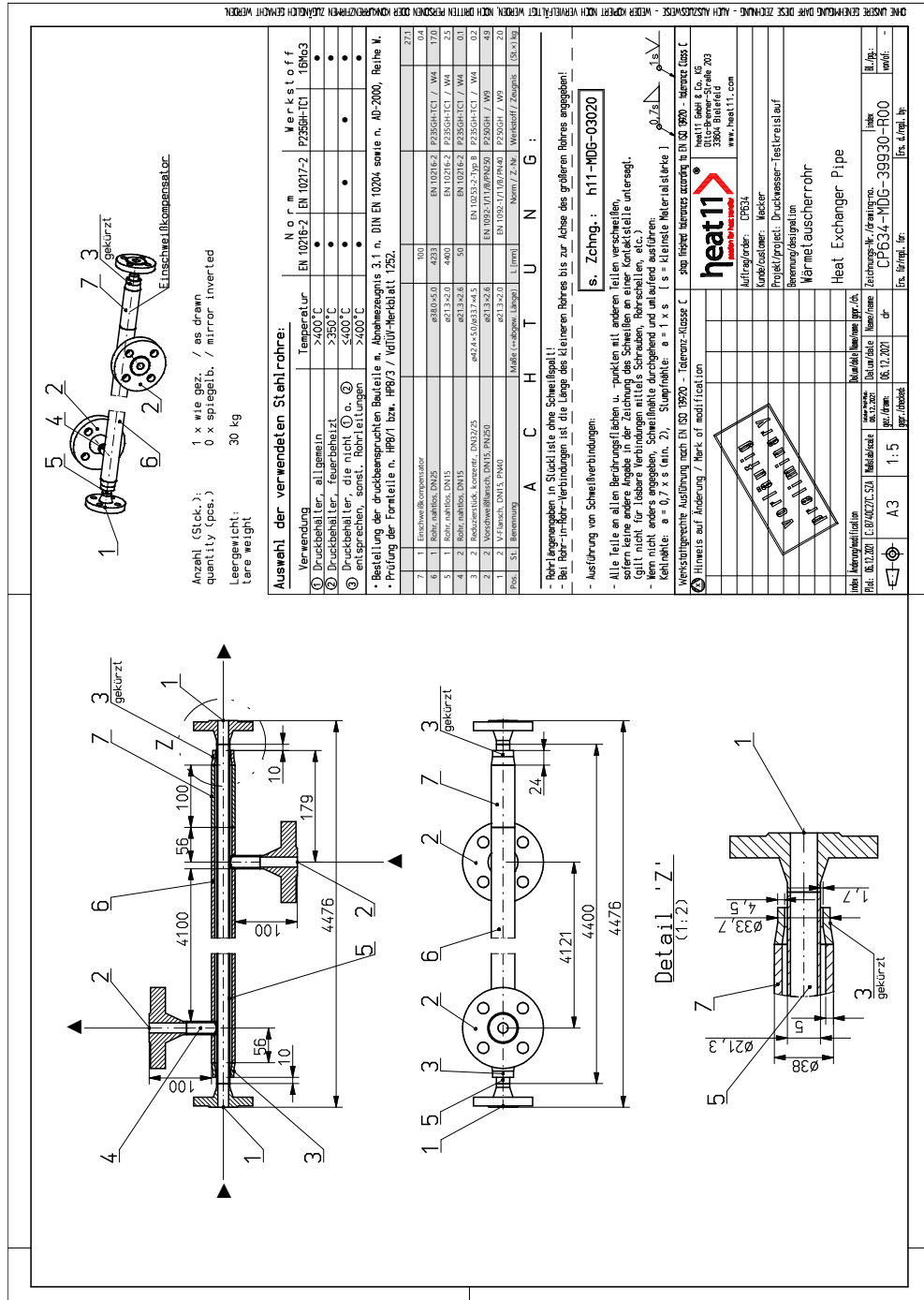


Figure C.1.: Initial Drawing of the heat exchanger



Figure C.2.: Guiding tubes for stabilisation Pt100 sensors through the measuring chamber

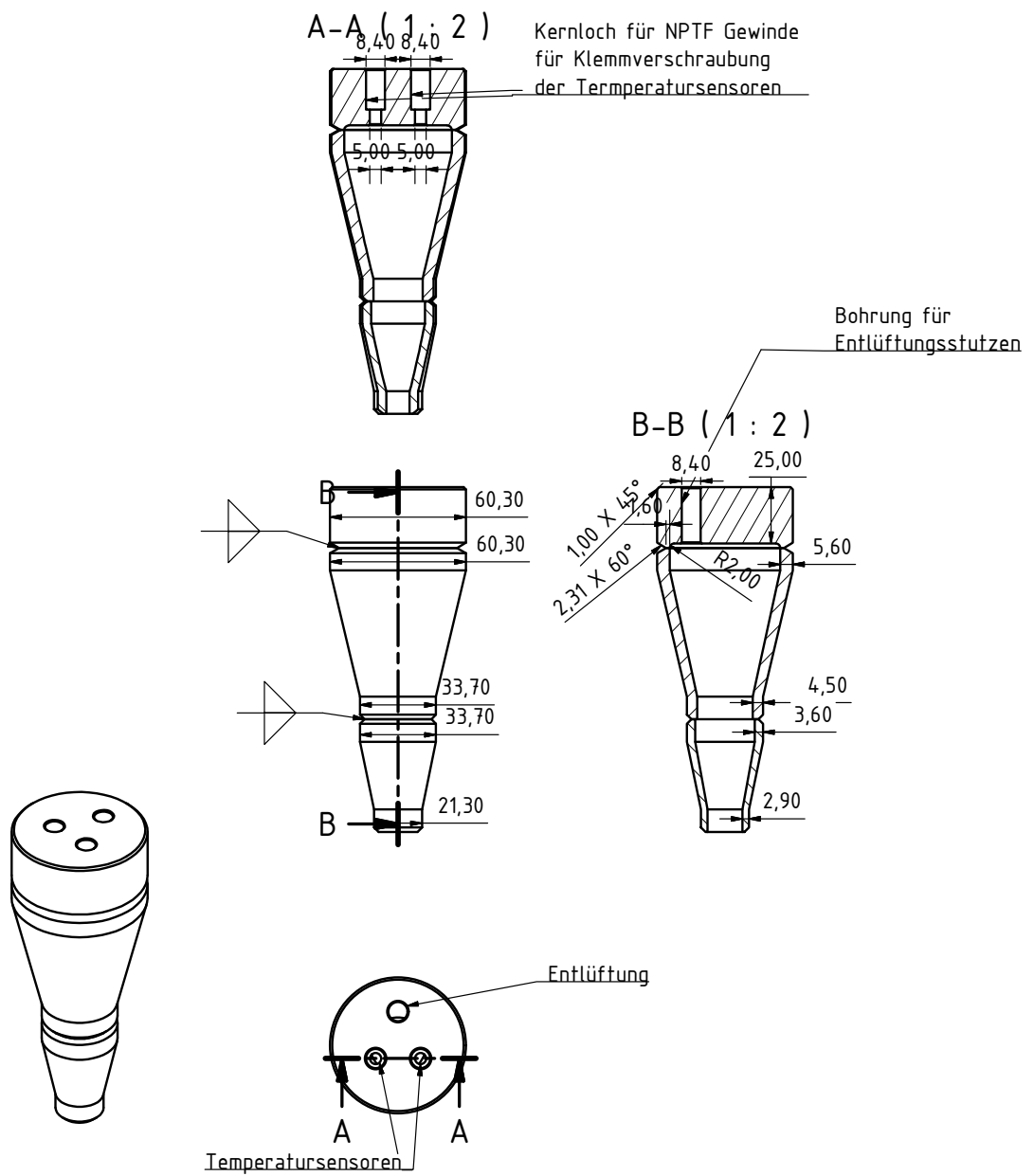


Figure C.3.: Technical drawing of the temperature measurement chamber for the heat exchanger

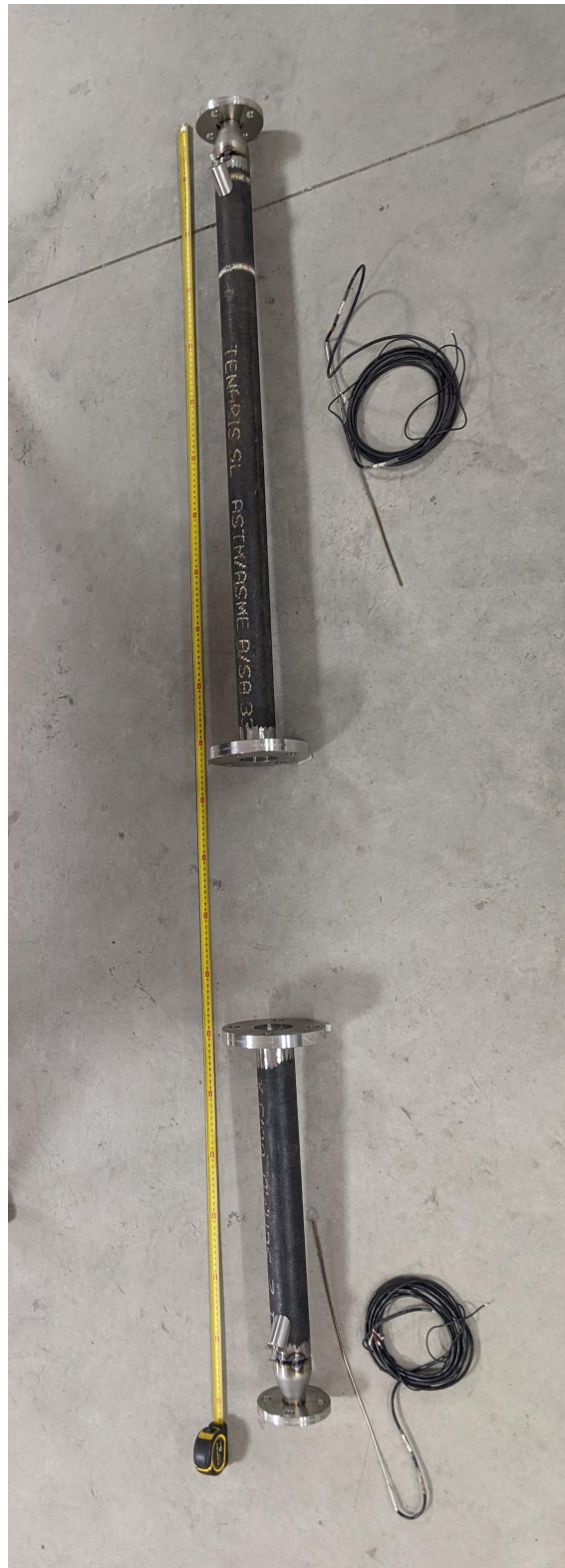


Figure C.4.: Measurement section for in-situ LDA calibration for temperatures up to 300°C for silicone oil

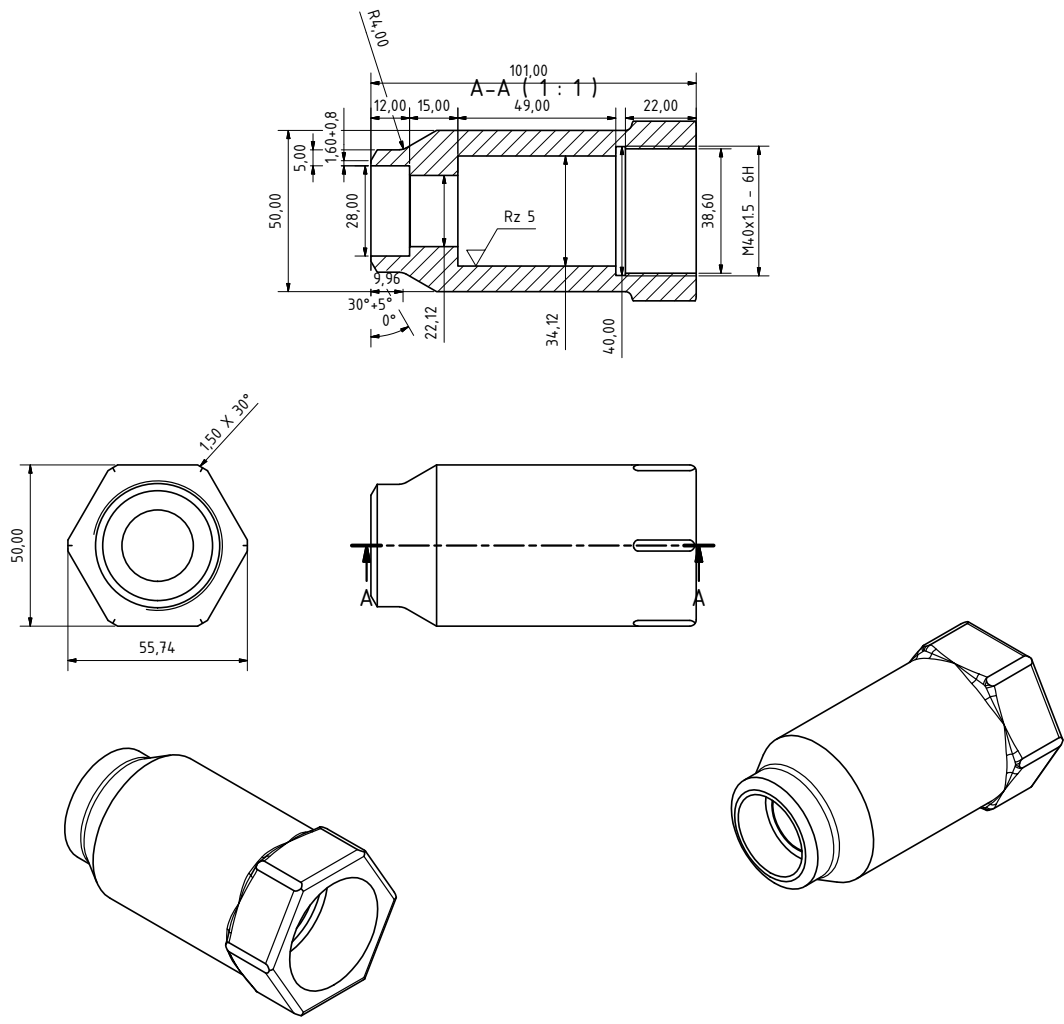


Figure C.5.: Technical drawing of the stuffing box

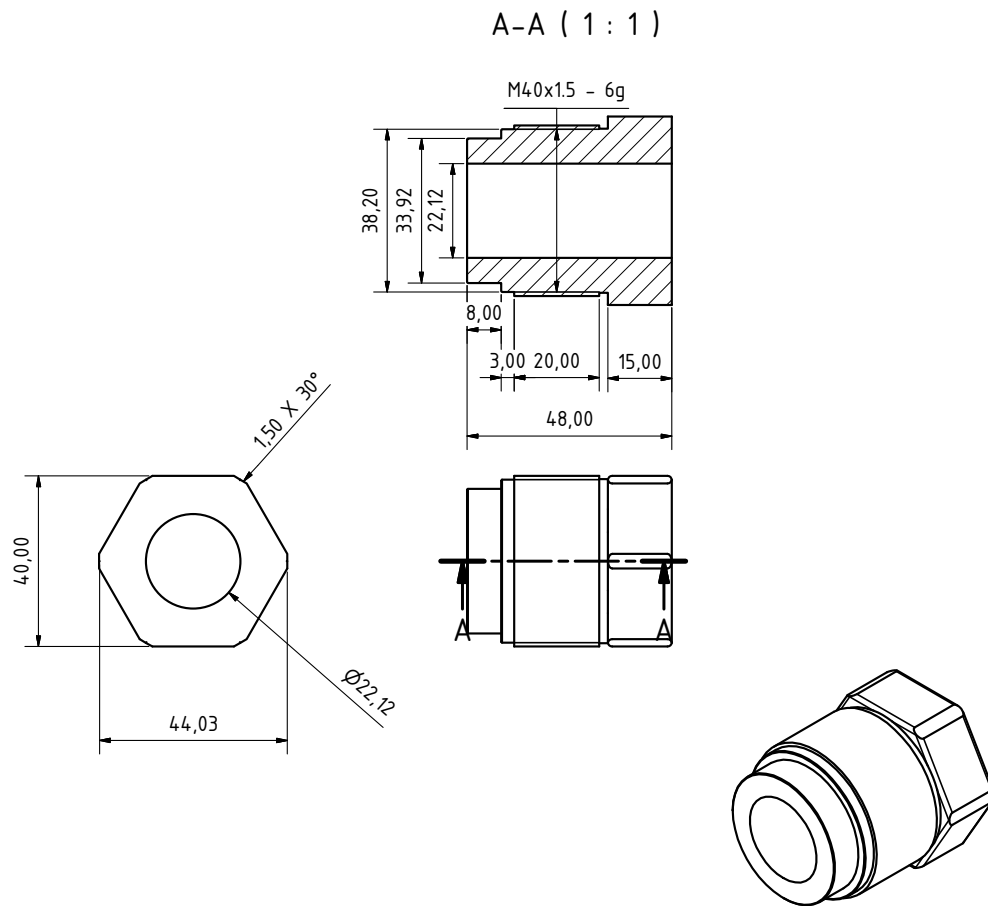


Figure C.6.: Technical drawing of the nut of the stuffing box

D. Uncertainty Estimation of the Heat Transfer Coefficient

```

1 % Relvant values for alpha water
2 m_Water_val =      0.2508;
3 rho_water_val =    840.4;
4 di_outer_val =     0.029;
5 da_val =           0.022;
6 dynVis_val =       0.0001209;
7 cp_mean_Water_val = 4585;
8 k_water_val =      0.6514;
9 len_val =          2;
10 % Type B uncertainties
11 TypeB_m_Water =    0.001 *m_Water_val;
12 TypeB_rho_water =  0.003* rho_water_val;
13 TypeB_di_outer =   0.00009;
14 TypeB_da =         0.00005;
15 TypeB_dynVis =     0.003* dynVis_val;
16 TypeB_cp_mean_Water = 0.003* cp_mean_Water_val;
17 TypeB_k_water =    0.003* k_water_val;
18 TypeB_len =        0.00015;
19
20 syms m_Water rho_water di_outer da dynVis cp_mean_Water k_water len
21
22 %% Formulas for calculating alpha_water
23 velocity_water =   m_Water / (rho_water * (pi * 0.25 * (((di_outer)^2) - ...
24 (da)^2))); % calculation of flow velocity [m/s]
25 dh =              (di_outer - da); % hydraulic diameter in [m]
26 Reynold_water =   rho_water * velocity_water * dh / dynVis;
27 a =               da / di_outer; % relation of diameter
28 Pr_water =        dynVis * cp_mean_Water / k_water;
29 k1 =              1.07 + 900 / Reynold_water - 0.63 / (1 + 10 * Pr_water);
30 Re_water_star =   Reynold_water * (((1 + a^2) * log(a) + (1 - a^2))/...
31 ((1 - a)^2 * log(a))); % Reynold with correction for
32 % pressuredrop Xi
33 Xi_water_Rsp =    (1.8 * log10(Re_water_star) - 1.5)^(-2); % Pressure drop
34 F_Rsp =           0.75 * a^(-0.17); % Korrelation factor
35 Nusselt_mT_water = (((Xi_water_Rsp / 8) * Reynold_water * Pr_water) * ...
36 (1 + (dh / len)^(2/3))) * F_Rsp / (k1 + 12.7 * ...
37 sqrt(Xi_water_Rsp / 8) * ((Pr_water^(2/3)) - 1));
38 % Nusselt for medium wall temperature
39 alpha_water =     Nusselt_mT_water * k_water / dh;
40 % alpha with medium walltemperature
41 % Partial derivatives for alpha water

```

D. Uncertainty Estimation of the Heat Transfer Coefficient

```
42 % List of variables and their values
43 variables = [m_Water, rho_water, di_outer, da, dynVis, cp_mean_Water, ...
44             k_water, len];
45 values =    [m_Water_val, rho_water_val, di_outer_val, da_val, dynVis_val, ...
46             cp_mean_Water_val, k_water_val, len_val];
47
48 partial_derivatives = [];
49
50 % Calculate the partial derivatives
51 for i = 1:numel(variables)
52     variable = variables(i);
53     partial_derivative = diff(alpha_water, variable);
54     partial_derivatives = [partial_derivatives, partial_derivative];
55 end
56
57 % Initialise the list of partial derivative values
58 partial_derivative_values = zeros(size(partial_derivatives));
59
60 % Calculate the partial derivative values in a loop
61 for i = 1:numel(partial_derivatives)
62     partial_derivative = partial_derivatives(i);
63     partial_derivative_value = double(subs(partial_derivative, variables,
64     values));
65     partial_derivative_values(i) = partial_derivative_value;
66 end
67
68 alpha_water_value = double(subs(alpha_water, variables, values));
69
70 % Calculate the uncertainties for each parameter
71 uncertainties = [TypeB_m_Water, TypeB_rho_water, TypeB_di_outer, TypeB_da, ...
72                 TypeB_dynVis, TypeB_cp_mean_Water, TypeB_k_water, TypeB_len];
73 uncertainty_values = uncertainties .* partial_derivative_values;
74
75 % Calculate the absolute and relative uncertainty for alpha_water
76 u_alpha_water_abs = sqrt(sum(uncertainty_values.^2));
77 u_alpha_water_rel = u_alpha_water_abs / alpha_water_value * 100;
78
79 % Print values to console
80 disp(['alpha_water = ' num2str(alpha_water_value)]);
81 disp(['with an absolute uncertainty of = ' num2str(u_alpha_water_abs)]);
82 disp(['and a relative uncertainty = ' num2str(u_alpha_water_rel) '%']);
```

D.1. Partial Derivatives of the Specific Heat Transfer Coefficient of HXLP

$$\begin{aligned}
 \frac{\partial \alpha_{HXLP}}{\partial d_a} &= \frac{d_a \left(\frac{\log\left(\frac{d_a}{d_i}\right)}{2 \cdot \lambda_{steel}} + \frac{1}{2 \cdot \lambda_{steel}} \right)}{d_i \left(\frac{1}{\alpha_{water}} - \frac{1}{k} + \frac{d_a \cdot \log\left(\frac{d_a}{d_i}\right)}{2 \cdot \lambda_{steel}} \right)^2} - \frac{1}{d_i \left(\frac{1}{\alpha_{water}} - \frac{1}{k} + \frac{d_a \cdot \log\left(\frac{d_a}{d_i}\right)}{2 \cdot \lambda_{steel}} \right)} \\
 \frac{\partial \alpha_{HXLP}}{\partial d_i} &= \frac{d_a}{d_i^2 \left(\frac{1}{\alpha_{water}} - \frac{1}{k} + \frac{d_a \cdot \log\left(\frac{d_a}{d_i}\right)}{2 \cdot \lambda_{steel}} \right)} - \frac{d_a^2}{2 \cdot d_i^2 \cdot \lambda_{steel} \left(\frac{1}{\alpha_{water}} - \frac{1}{k} + \frac{d_a \cdot \log\left(\frac{d_a}{d_i}\right)}{2 \cdot \lambda_{steel}} \right)^2} \\
 \frac{\partial \alpha_{HXLP}}{\partial k} &= \frac{d_a}{d_i \cdot k^2 \left(\frac{1}{\alpha_{water}} - \frac{1}{k} + \frac{d_a \cdot \log\left(\frac{d_a}{d_i}\right)}{2 \cdot \lambda_{steel}} \right)^2} \\
 \frac{\partial \alpha_{HXLP}}{\partial \lambda_{steel}} &= - \frac{d_a^2 \cdot \log\left(\frac{d_a}{d_i}\right)}{2 \cdot d_i \cdot \lambda_{steel}^2 \left(\frac{1}{\alpha_{water}} - \frac{1}{k} + \frac{d_a \cdot \log\left(\frac{d_a}{d_i}\right)}{2 \cdot \lambda_{steel}} \right)^2} \\
 \frac{\partial \alpha_{HXLP}}{\partial \alpha_{water}} &= - \frac{d_a}{\alpha_{water}^2 \cdot d_i \left(\frac{1}{\alpha_{water}} - \frac{1}{k} + \frac{d_a \cdot \log\left(\frac{d_a}{d_i}\right)}{2 \cdot \lambda_{steel}} \right)^2}
 \end{aligned} \tag{D.1}$$